INFLUENCE OF N INCORPORATION ON THE ELECTRONIC PROPERTIES OF DILUTE NITRIDE (IN)GaAsN ALLOYS

by

Yu Jin

A dissertation submitted in partial fulfillment
of the requirements for the degree of
Doctor of Philosophy
(Physics)
in the University of Michigan
2010

Doctoral Committee:

Associate Professor Cagliyan Kurdak, Chair
Professor Roy Clarke
Professor Rachel S. Goldman
Professor Ctirad Uher
Professor Stephen Fahy, University College Cork, Ireland

ACKNOWLEDGEMENTS

I would like to thank my advisor, Rachel S. Goldman for her guidance and support throughout my studies at the University of Michigan. I would also like to thank Cagliyan Kurdak, Stephen Fahy, Roy Clarke, and Ctirad Uher for their valuable discussions and suggestions.

This dissertation would not have been possible without the help of my many collaborators: Dr. Matthew Reason in Materials Science & Engineering; Mr. Hailing Cheng in Physics; Miss. Yan He, Dr. Alexander M. Mintairov and Prof. James L. Merz in Electrical Engineering, University of Notre Dame; and Dr. Yongqiang Wang from Los Alamos National Laboratory

I thank all my fellow students in Professor Goldman's research group for their help. In particular, I would like to thank Jiahung Wu, Tassilo Dannecker, Weifeng Ye, and Leon Webster for working on the MBE system with me; Ryan M. Jock, Christer Akouala, Niall Mangan and Kutessa Garnett, for their help with various sample characterizations; Rachel Collino and Vaishno Dasika for their support and encouragement.

I gratefully acknowledge the support from the NSF-FRG grant #DMR-060640 monitored by L.Hess, and the support from the Center for Solar and Thermal Energy Conversion, an Energy Frontier Research Center funded by the U.S. Department of

Energy, Office of Science, Office of Basic Energy Sciences under Award Number DE-SC0000957.

Finally, my greatest gratitude to my parents.

TABLE OF CONTENTS

LIST OF TABLES

Table

LIST OF FIGURES

Figure

LIST OF APPENDICES

Appendix

CHAPTER 1

INTRODUCTION

1.1 Overview

Dilute nitride (In)GaAsN alloys have attracted considerable attention in the past few years. The bandgap energy of GaAsN is substantially reduced as the N composition increases, i.e., for ~1% N added to GaAs, the band gap energy is reduced by ~150 meV.[1-4] The significant bandgap bowing enables the growth of dilute nitride semiconductor alloys with a variety of bandgap energies in the near-infrared regime, while maintaining near-lattice-matching with common substrates such as GaAs and InP. Therefore, (In)GaAsN alloys films and heterostructures are promising for a wide range of optoelectronic applications. In addition, due to the very low solubility of N in GaAs, GaAsN alloys provide a unique opportunity for investigating non-equilibrium growth processes.[5-7]

It is believed that the N-induced localized states perturb the conduction band (CB) edge of GaAs, causing potential fluctuations and carrier trapping and/or scattering. Therefore, (In)GaAsN alloys provide an opportunity for investigation of the interactions between localized states and free carriers in semiconductors.[8-11] Furthermore, the degree of N-induced perturbation can be easily tuned by parameters such as N composition, doping concentration, and annealing temperature. Thus, this material system is ideal for

the study of the physics of weak and strong localization.[12, 13]

Due to the large size and electronegativity differences between As and N, the formation of several point defect complexes has been predicted.[14-16] These point defect complexes are likely the origin of the limited optical emission efficiency and minority carrier transport properties observed in (In)GaAsN alloys. Indeed, the defect physics in GaAsN is expected to be substantially different from conventional semiconductor alloys. A significant concentration of N atoms are expected to incorporate in non-substitutional sites, such as N insterstitials.[17-19] Therefore, it is important to understand the physical nature of these N-related defects.

In this chapter, we first review the current status of (In)GaAsN optoelectronic device development. Next, we review the theoretical studies of the band structure of (In)GaAsN. Then, we will discuss two types of N-related defects in GaAsN: intrinsic N split interstitial defects and extrinsic N-Si defect complexes, and their influence on the structural and transport properties of GaAsN. Finally, we will summarize the present experimental and theoretical understanding of the electronic and optical properties of GaAsN alloys.

1.2 Bandgap bowing and device applications of GaAsN Alloys

The simplest prediction of the physical properties of semiconductor ternary alloys is a linear extrapolation between the properties of the endpoint elements or binary compounds, namely Vegard's law, or the law of mixtures.[20] Figure 1.1 shows a plot of bandgap energy vs. lattice parameter for various III-V semiconductor alloys.[1, 2, 21-25] The points correspond to the energy bandgap, E_g, and bond length for each elemental or

binary semiconductor, and the lines connecting those points correspond to the alloys. Typically, E_g of the alloys of the elemental or binary compound semiconductors are not linear interpolations of the endpoints (as would be predicted by Vegard's law) but instead are slightly bowed to a lower band gap. Such behavior is typically described by a quadratic deviation from Vegard's Law, with a bowing parameter, *b*. In conventional III-V alloys, *b* is typically composition-independent, with values of fractions of an eV.[21] On the other hand, for GaAsN, *b* = 18-20 eV, and as shown in Fig. 1.1, E_g of GaAsN decreases rapidly with increasing N composition.[1, 26-33] In addition, *b* is N composition dependent, decreasing with increasing N composition.

The energy bandgap bowing in semiconductors has been attributed to alloy disorder, with *b* values related to the electronegativity mismatch of the constituents.[34, 35] Shown in Table 1.1 is a summary of the properties of Group V elements, including electronic structure, atomic mass, covalent radius, and Pauling's electronegativity.[36] The electronegativity difference between N and As/P is 1.0/0.9 eV, much larger than those between other group V elements.[21, 37 37] Thus, significant bandgap bowing is observed in highly mismatched alloys such as III-V-N, as shown in Table 1.2.

Table 1.1: Properties of elements of interest from groups V, including electronic structure, atomic mass, covalent radius and Pauling's electronegativity[36]

Element	Electronic Structure	Atomic Mass	Covalent Radius (nm)	Electronegativity
N	(He) $2s^2 2p^3$	14.007	0.07	3.04
P	(Ne) $3s^2 3p^3$	30.97	0.106	2.19
As	(Ar) $3d^{10} 4s^2 4p^3$	74.92	0.118	2.18
Sb	(Kr) $4d^{10} 5s^2 5p^3$	121.75	0.136	2.05
Bi	(Xe) $4f^{14} 5d^{10} 6s^2 6p^3$	208.98	0.145	2.02

Table 1.2: Electronegativity difference between group V elements, E_B-E_c(eV), and the bandgap bowing parameter, *b*, for selected III-V alloys. *b* values are adopted from Ref.[21]

Alloys AB_xC_{1-x}	E_B-E_c(*eV*)	*b(eV)*	Alloys AB_xC_{1-x}	E_B-E_c (*eV*)	*b(eV)*
GaAsSb	0.2	1.43	GaAsN	1	120.4–100*x*
InAsSb	0.2	0.67	GaPN	0.9	3.9
AlAsSb	0.2	0.8	InPN	0.9	15
GaPAs	0.1	0.19	InAsN	1	4.22
InPAs	0.1	0.1			
AlPAs	0.1	0.22			
GaPSb	0.3	2.7			
InPSb	0.3	1.9			

The simultaneous incorporation of In and N with a specific composition ratio (In:N=3:1) enables the formation of unstrained InGaAsN on GaAs or InP substrates with bandgap energy lower than 1.42 eV.[1, 2, 3] For example, according to calculations, InGaAsN lattice matched to GaAs with E_g = 0.93 *eV* (λ =1.33 μm) and 0.8 *eV* (λ =1.55 μm) can be achieved with $In_{0.10}GaAsN_{0.038}$ and $In_{0.18}GaAsN_{0.06}$.[38] Furthermore, with 20% N incorporation into GaAs or 2% N in GaP, $GaN_{0.2}As_{0.8}$ or $GaN_{0.02}P_{0.98}$ are lattice matched to Si, which potentially enables the high quality III-V epitaxial films on Si substrates. The ability to substantially change the band gap energy while maintaining lattice matching to common substrates makes (In)GaAsN a promising material for a wide range of near infrared optoelectronics applications, including long-wavelength light-emitters and detectors, high-performance electronic devices, and high-efficiency solar cells.[39-50]

For example, InGaAsN has recently demonstrated promise for laser diodes operating at the optical fiber communication wavelength window (1.3-1.55 μm).[51-57] For light-emitting applications, InGaAsN has several advantages in comparison with the

conventional InGaAs(P) system.[58] First, the InGaAsN/(Al)GaAs quantum well is reported to have type I band alignment, with a much larger CB offset, ΔE_c, than that of GaInPAs/InP quantum wells.[59] For example, for lattice-matched InGaAsP/InP, it has been reported that $\Delta E_c \sim 0.39\,\Delta E_g$, corresponding to 50~200 meV.[60] On the other hand, for InGaAsN/GaAs, it has been reported that $\Delta E_c \sim 0.8\,\Delta E_g$.[61, 62] In addition, InGaAsN can be combined with AlGaAs, where ΔE_c between GaAs and AlGaAs is reported to be greater than $0.6\,\Delta E_g$,[63] potentially leading to InGaAsN/AlGaAs $\Delta E_c > 0.5\ eV$. The deep well for InGaAsN/AlGaAs is predicted to lead to several advantages for lasers, including reduced temperature sensitivity of both the threshold current and the lasing wavelength. In heterojunction bipolar transistors (HBT), the incorporation of InGaAsN alloys into the base layers enables lowering of the turn on voltages and collector currents due to the increased band offset.[48, 49] Since InGaAsN active layers can be grown lattice-matched to a highly reflective GaAs/AlAs layer, these alloys are also useful for vertical cavity surface-emitting lasers (VCSELs). Indeed, the GaAs/AlGaAs distributed Bragg reflector (DBR) mirrors are more easily incorporated into InGaAsN-based VCSELs than in InP-based VCSELs.[42, 44] To date, InGaAsN (~4% N, ~10% In) has been used in 1.3 μm VCSELs commercially available from Infineon,[44] and related alloys have been used to produce lasers operating at 1500 nm.[64]

Due to the possibility of tailoring the bandgap in the range of 1.0 to 1.4 eV by varying the N and In concentration, while lattice-matching to Ge or GaAs is maintained, InGaAsN is also useful for solar cells. Indeed, one strategy for increasing the efficiency of terrestrial photovoltaics involves the use of multi-junction solar cells, with each junction material preferentially absorbing different regions of the solar spectrum. The

thermodynamic efficiency limit of an optimized four-junction device with the top GaInP and bottom Ge cell was calculated to be 41% under air-mass 0.[65] To achieve this efficiency, GaAs, with a bandgap of 1.4 eV, would be applied for cell 2, whereas cell 3 should have a bandgap of 1.0 eV, which can be achieved using InGaAsN films with 8% In and 2.8% N.[66] Kurtz *et al.* suggested that the addition of InGaAsN cells to a commercial tandem InGaP-GaAs structure would improve the internal quantum efficiency to a record value of ~ 70%.[47] To date, efficiencies of 11.27% and 21% have been achieved for single and multi-junction InGaAsN solar cell. [67-69] Furthermore, for GaAsN/GaAs MQW solar cells, current output comparable to that of conventional GaInNAs solar cells, with output voltages significantly higher than bulk-like counterparts, has been reported.[70]

1.3 Electronic structure of GaAsN alloys

A basic understanding of the unusual electronic structure of GaAsN alloys has been provided by Hjalmarson, whose tight-binding calculations predict that the energy levels of elements with high electronegativity are located at energies lower than those of more-metallic impurities.[71] Thus, replacement of As with P is predicted to produce an energy level high in the CB of GaAs, leading to a relatively weak interaction between the impurity and the extended band. However, substitution of As with highly electronegative N results in a level located close to the CB minimum. This impurity state interacts strongly with extended CB states and drastically modifies the electronic structure of the GaAsN alloys, presumably leading to the unusual bandgap bowing in GaAsN alloys.

Among the many attempts to understand the (In)GaAsN band structure,[9, 11, 72-79]

a semi-empirical band anti-crossing (BAC) model proposed by Shan *et al.*[80, 81] has been most successful in explaining the bandgap bowing effect in (In)GaAsN. Within this model, a higher lying localized N band, E_N, interacts with the extended host semiconductor band, E_c, resulting in a split of the CB into two sub-bands, E_+ and E_-, as schematically shown in Fig. 1.2.[82] The lower sub-band, E_-, is shifted downwards, and has mainly delocalized CB-like character; it is considered to be responsible for the reduction of the fundamental bandgap. On the other hand, the upper sub-band, E_+, mainly has the character of N localized states.

The BAC model has been able to explain the three fundamental transitions observed with electroreflectance and photoreflectance measurements in bulk GaAsN films,[80, 81, 83] and permits remarkable fitting to measured bulk-like quantities such as composition, pressure, and temperature-dependent bandgaps.[80, 81, 84] In addition, the BAC model predicts a non-parabolic CB dispersion, which has been measured by magnetotunneling [85] and photoreflectance spectroscopy[86, 87] of GaAsN quantum wells. The BAC model also predicts a N-composition-dependent flattening of the E_- band, which in turn would lead to a N-composition-dependent increase in the electron effective mass, m_e*.[79, 84, 88]

However, the BAC model simplifies the picture by only considering a single local state, independent of the N composition. Although the BAC model qualitatively predicts the bandgap dependence on N composition, it does not enable quantitative explanations of several extraordinary optical and electronic behavior, such as the composition-dependent non-monotonic increase in m_e* [89, 90, 97-99] and the electron gyromagnetic factor, g_e*,[91] which have been observed with magnetophotoluminescence[90, 91] and optically

detected cyclotron resonance technique[89] of InGaAsN alloys.

In addition to the bandgap lowering due to substitutional N incorporation, a number of N-induced defect levels near the CB edge have been predicted, including N nearest neighbor pairs, triplets and clusters, as well as N interstitials and defect complexes. [9, 91-98] The distribution of these N levels is expected to significantly influence the electronic properties of GaAsN. For example, the linear combination of isolated N resonant states (LCINS) model,[99] a modified BAC model, which explicitly includes N-induced defect levels, predicts the existence of the E_- level and identifies an E_+ level that broadens with increasing N composition. In addition, the LCINS model predicts the non-monotonic increase in m_e^* observed experimentally.[98, 100, 101] Figure 1.3 presents a plot of m_e^* vs. N composition in $GaAs_{1-x}N_x$ determined by experimental techniques (open symbols),[98, 100, 101] in comparison with those calculated using a two-level BAC model (dashed line),[24] and the LCINS model, i.e., including hybridization between the CB edge and the N cluster state (solid symbols).[11]

1.4 N-related point defects in GaAsN alloys

In this dissertation, we consider two types of N-related point defect complexes, with or without additional external elements, such as electronic impurities. Several N-related extrinsic (i.e., with additional external elements) point defect complexes have been reported in GaAsN, including N-H_x and Si-N. The presence of N-H_x complexes apparently increases the lattice parameter[102] and the bandgap energy[103, 104] of GaAsN, and correspondingly, reduces the effective mass[105] and gyromagnetic factor.[91] Moreover, these effects may be reversible by thermal annealing up to 550ºC, which apparently leads

to the dissociation of N-H_x. However, for N-H_x complexes, the number and locations of H atoms surrounding N is still under debate.[104, 106, 107] In addition, it was recently reported that group IV donors form donor-N defect complexes with N, as shown in Fig. 1.4 (a). For example, Si-N complexes have been reported to inhibit the electronic activity of Si donors, leading to reduced free carrier concentration and increased resistivity.[15, 108, 109] However, there have been conflicting reports on the form of the Si–N complex,[14, 16] and the influence of Si–N complexes on GaAsN electronic properties remains unknown.

Several N-related intrinsic (i.e., without additional external elements) point defect complexes have also been reported, including NN pairs, triplets and clusters, as well as N interstitials. Generally, the term "N clusters" refer to 2-4 N atoms which share a common Ga nearest neighbor. Fahy *et al.* predicted that such N clusters produce various defect levels in the vicinity of the CB edge of GaAsN.[110] When the defect levels are resonant with the CB edge, they are expected to lead to potential fluctuations and electron scattering.[110]

Of particular interest in this thesis work is non-substitutional intrinsic N point defect, i.e., N interstitials. Fig. 1.4 (b) shows several possible configurations of N incorporation in GaAs.[17, 111] For substitutional N, N_{As}, a N atom takes the place of an As atom; for the N-N split interstitial complex, $(NN)_{As}$, an N_2 molecule takes the place of an As atom; for the N-As split interstitial complex, $(NAs)_{As}$, a N and an As atom are both located on the As lattice site. According to the first principle total energy calculations of Zhang *et al.*[112], $(NN)_{As}$ is expected to be the dominant intrinsic defect because of the exceptionally strong N-N bond and the small size of the N atom. The calculated N-N bond length is 1.39 Å, which is only slightly longer than the bond length for the N_2

molecule (1.10 Å). In addition, the calculated formation energy, ΔH_f, for $(NN)_{As}$ is 1.52 eV, considerably smaller than those of other atomic defects such as As antisites (2.24eV) and As_{Ga}-N_{As} (1.96 eV).[17] In addition, the formation of $(NAs)_{As}$ and $(NN)_{As}$ might help release surface tension during growth. Since N atoms are smaller than As atoms, GaAsN growth is under tensile strain.[113] $(NN)_{As}$ and $(NAs)_{As}$ dilate the lattice and compensate the tensile strain of the GaAsN alloy; therefore, these point defects are energetically favorable.

Various methods have been used to indirectly or directly detect the N interstitial incorporation in GaAsN. By comparing the local vibrational modes observed in GaAsN with those for Si_{As} and Si_{Ga} in GaAs, Ramsteiner assigned the origin of features in GaAsN Raman spectra to $(NN)_{As}$ and $(NN)_{Ga}$.[114] Krispin *et al*. detected two predominant electron traps at about 1.1 and 0.8 eV above the valence band (VB) edge, and associated them with $(NAs)_{As}$ and $(NN)_{As}$, respectively.[115] Using in-situ substrate curvature monitoring and ex-situ x-ray diffraction measurements, Adamcyk *et al*. attributed the residual strain in GaAsN to N interstitial incorporation.[116]

Nuclear reaction analysis (NRA) is so far the only direct method to quantitatively determine the interstitial N fraction, f_{int}, in GaAsN films. [18, 19, 117-119] In previous work from our group,[18] significant composition-dependent interstitial N incorporation was found in GaAsN films with total N compositions ranging from 0.7-3.8%. However, Bisognin *et al*.[120] instead asserted that the apparent interstitial N measured by NRA was instead due to N surface contamination.

In addition, it has been suggested that f_{int} is influenced by the surface reconstruction during growth and post-growth RTA. In previous work from our group,[18]

the (2x1) reconstruction was identified as the surface structure which leads to the highest substitutional N incorporation, likely due to the high number of group V sites per unit area available for N–As exchange.[18] In addition, using NRA, two groups reported with two data points that annealing reduces f_{int}.[19, 118] However, using PL, two other groups reported that annealing causes N atoms to hop from substitutional to interstitial sites, i.e., a substitutional "kick-out" effect,[121, 122] thereby increasing f_{int}.

To date, the influence of N interstitials on the electronic properties of GaAsN has been investigated computationally. It has been predicted that the N interstitials produce single electron occupancy deep levels below the GaAsN CB edge, acting as recombination centers for minority carriers.[123] Thus, N interstitials are expected to be detrimental to both electron and hole mobilities.[124] At present, the effect of surface reconstruction and annealing on the N interstitial incorporation and its influence on the electronic properties of (In)GaAsN remain unknown.

1.5 Optical and electronic properties of GaAsN alloys

To date, literature reports have presented substantially lower electron mobilities, μ, for (In)GaAsN alloys in comparison with those of (In)GaAs. [101, 110, 125, 126] Fig. 1.5 shows a plot of μ as a function of N composition, x, for $GaAs_{1-x}N_x$ films, including data from our group and from those of literature reports.[101, 125, 127-129] As x is increased from 0 to ~0.01, μ is reduced by more than one order of magnitude. As x is further increased to 0.02, μ continues to slowly decrease.

To date, only a few theoretical studies have focused on understanding this drastic degradation of μ with increasing x in $GaAs_{1-x}N_x$.[110, 126, 130] Hashimoto *et al.* attributed the

decreasing μ to an unspecified N-induced scattering.[128] Skierbiszewski *et al.* argued that the reduction in μ results from the enhanced m_e^* with x due to the nonparabolic energy dispersion of GaAsN CB predicted by the BAC model.[129] However, calculations which include contributions from the band nonparabolicity predicted by BAC model as well as polar optical, acoustic phonon, piezoelectric, ionized impurity, and neutral impurity scattering, predicted a GaAsN low field μ of ~ 1000 $cm^2V^{-1}s^{-1}$ (as indicated by the dashed line in Fig. 1.5) [126], which is still an order of magnitude higher than measured values (as indicated by the scattered data points in Fig. 1.5). The discrepancy between experimental and calculated μ values suggests that the electron scattering in GaAsN cannot be accounted for solely by the CB nonparabolicity-induced increase in m_e^*, as predicted by the BAC model.

More recently, Fahy *et al.* modified the BAC model to include the influence of nitrogen clusters.[110] With an independent scattering approximation (i.e., the total scattering rate is the sum of the scattering rates of the individual N atoms), Fahy estimated a μ of ~400 cm^2/Vs for $GaAs_{1-x}N_x$ with x=0.01-0.02 (as indicated by the solid line in Fig. 1.5), which is much lower than Vaughan's result, but still about a factor of two higher than measured values. The discrepancy between the x-dependence of μ and the theoretical predictions suggests that scattering sources in addition to substitutional N and N clusters, such as $(NN)_{As}$ or $(NAs)_{As}$ split interstitials, need to be taken into account theoretically.

For the optical properties of $GaAs_{1-x}N_x$, as x is increased, a red-shift (shift to longer wavelength) in photoluminescence (PL) emission is usually accompanied by a drastic degradation in the emission intensity.[1, 27, 28] For example, when x in $GaAs_{1-x}N_x$ is

increased from 0.01 to 0.045, the near-band-edge (NBE) PL efficency decreases by a factor of 60.[58] This degradation in PL efficiency is commonly attributed to "poor structural quality" and the influence of "nonradiative recombination centers" in GaAsN alloys.[42, 131, 85] However, at present, limited information is available regarding the atomic and electronic structure of these nonradiative defects.

Several other features are also commonly observed in NBE PL spectra of GaAsN, such as absorption/emission Stokes shifts, excitation-power-dependent emission blueshift, and asymmetric emission peak lineshape with long tails on the low energy side.[58] These features are typically associated with carrier localization.[132] For localization in GaAsN, Buynova *et al.* estimated a localization potential (schematically shown in Fig. 4.3), $\triangle$E ~ 40-60 meV, which is higher than the 7-10 meV value for other alloys systems, such as GaAsP, AlGaAs and SiGe.[58] Furthermore, in near-field PL measurements below 70K, Mintairov *et al.* observed narrow lines with FWHM 0.2–2 meV.[133, 134] The lines were attributed to "quantum-dot-like" excitonic recombination, which suggests the presence of nitrogen clustering above that of a random distribution.

A key quantity for solar cell and HBT applications is the minority carrier diffusion length, L_m, which depends on the electron mobility and the carrier lifetime, as follows:

$$L_m = (\mu \tau k_B T / e)^{1/2} \tag{1.1}$$

for the non-degenerate case. In solar cells, L_m is ideally substantially longer than the optical absorption length for solar photons, allowing all incident photons to be absorbed and all optically-generated carriers to contribute to the electrical current of the device. For example, in GaAs, the optical absorption length is ~ 3 µm, while L_m is ~ 10 µm. [47, 65,

[135] On the other hand, for InGaAsN with 1 eV bandgap, a lifetime of 0.3 ns and μ of 200 cm^2/Vs is typically considered good material,[127] which would result in L_m=0.4 μm. Indeed, it has been reported that the performance of four junction GaInP/GaAs/GaInNAs/Ge solar cells has been limited due to the short L_m of InGaAsN.[47, 65, 136]

Although there seems to be a discrepancy between the desired and obtained L_m in GaAsN, the increase in absorption coefficient, α, due to increased m_e^* in GaAsN has not been taken into account. The possibility of improving electron mobility with optimal growth conditions and post-growth thermal treatment also needs to be considered. α depends on the carrier effective mass as follows:

$$\alpha \propto m_r^{*3/2} \tag{1.2}$$

where $m_r^* = \frac{m_e^* m_h^*}{m_e^* + m_h^*}$ is the reduced effective mass, and m_e^* and m_h^* are the electron and hole effective masses, respectively. Since m_e^* of GaAsN is substantially larger than that of GaAs, [89, 90, 97-99] α is expected to be larger in GaAsN; thus, a somewhat shorter L_m might be acceptable for GaAsN. For example in $GaAs_{0.097}N_{0.013}$, m_e^* is expected to double, and α is expected to more than double in comparison with those of GaAs; thus, L_m ~ 1.5μm might be sufficient. In addition, various methods have been proposed to improve the electron mobility in GaAsN. For example, in this dissertation work, we observed post-growth rapid thermal annealing induced a 2-fold increase electron mobility in GaAsN films.[137]

1.6 Dissertation objectives

As discussed in Section 1.2, (In)GaAsN alloys with a few percent of N have shown significant promise for a wide range of applications. However, the incorporation of N degrades the optical and electronic properties, resulting in low electron mobilities, μ, and optical emission efficiencies, both of which have not been sufficiently accounted for by any theory. In general, the concentration, formation, and evolution of point defects have a significant impact on the optical and electronic properties of semiconductor materials. To date, few experimental studies have been devoted to identifying the physical model of N-related point defects; some results are contradictory to each other. This dissertation research was therefore devoted to investigations of N-related point defect complexes in GaAsN, including intrinsic N-related defects such as N interstitials, and extrinsic N-related defect complexes such as Si-N pairs. In particular, we examined the formation of these N-related point defects and their influence on the electronic and optical properties of (In)GaAsN alloys and heterostructures. In addition, we explored methods for controlling the concentration of these point defects, such as post-growth annealing treatment and the use of alternative dopants. Our goal was to understand the influence of the N-related defects on the free carrier trapping and scattering, and ultimately, to improve the minority carrier diffusion length of (In)GaAsN alloys for long-wavelength optoelectronic device applications.

1.7 Outline of the dissertation

The thesis is organized as follows: Chapter 2 describes the experimental procedures used for this work, including molecular beam epitaxy growth (MBE),

reflection high-energy electron diffraction (RHEED), rapid thermal annealing (RTA), x-ray rocking curves (XRC), atomic force microscopy (AFM), Rutherford backscattering spectroscopy (RBS), nuclear reaction analysis (NRA), photolithography device fabrication, variable temperature transport measurements, and Photoluminescence (PL), and Raman measurements.

Chapter 3 and chapter 4 describe our investigations of extrinsic and intrinsic N-related point defects, i.e., defects with or without the introduction of additional external elements. In chapter 3, we discuss our investigations of the influence of Si-N complexes on the electronic properties of GaAsN alloys, by comparing GaAsN films grown with various dopant-N spatial separations, dopant species, and surface reconstructions. First, we compare bulk-like $GaAs_{1-x}N_x$:Si films, where Si and N reside in the same layer, with modulation-doped heterostructures, where N and Si atoms are spatially separated. A decrease in *n* with increasing x was observed in bulk-like films but not in heterostructures, suggesting that Si-N complexes in the bulk GaAsN layers are acting as trapping centers. For GaAsN:Te (GaAsN:Si), *n* increases substantially (minimally) with annealing-*T*; for GaAsN:Si, *n* increases minimally with annealing-*T*, suggesting a competition between annealing-induced Si-N complex formation and a reduced concentration of N-related traps. Since Si-N complex formation is enhanced for GaAsN:Si growth with the (2 x 4) reconstruction, which has limited group V sites for As-N exchange, the $(Si\text{-}N)_{As}$ interstitial pair is identified as the dominant Si-N complex. Finally, modulation-doped GaAs(N)/AlGaAs heterostructures were utilized to study N-related carrier scattering mechanisms without the influence of Si-N defect complexes, and the dominant carrier scattering sources are identified to be neutral scatterers, such as N interstitials.

In Chapter 4, we present our investigations of the influence of intrinsic N-related point defects on the electronic properties of GaAsN alloy films. We observed four effects in as-grown GaAsN that are either removed or reduced following rapid thermal annealing (RTA). All four effects are likely explained by the RTA-induced reduction of the interstitial N fraction in GaAsN. First, for the as-grown GaAsN films, Hall and resistivity measurements reveal the onset of a metal-insulator transition (MIT), at a much higher n than that in GaAs. The MIT in GaAsN is accompanied by a shrinkage of the electron Bohr radius with increasing N composition, suggesting an increase in electron effective mass for GaAsN in comparison with that of GaAs. Furthermore, the temperature-dependence of n for $T > 150$K suggests the presence of a N-induced electron trapping level below the GaAsN CB edge, which is accompanied by a persistent photoconductivity (PPC) effect. Following RTA, significant increases in n and μ, and a transition occurs in the low T transport mechanism from hopping to extended band conduction are observed. Furthermore, following RTA, the temperature dependence of n is suppressed and the PPC effect vanishes, suggesting a reduction in the concentration of the N-induced electron trapping defects. Interestingly, NRA reveals an RTA-induced decrease in interstitial N fraction, f_{int}, and the corresponding signatures for the reduction in f_{int} are also identified in Raman Spectra. Therefore, it is likely that N interstitials are responsible for the MIT, the shrinkage in electron Bohr radius, the N-induced trapping level, and PPC effect discussed above. Thus, N interstitial defects are identified as the dominant form of intrinsic N defects in GaAsN alloys.

Summary and suggestions for future work are discussed in Chapter 5.

1.8 Figures

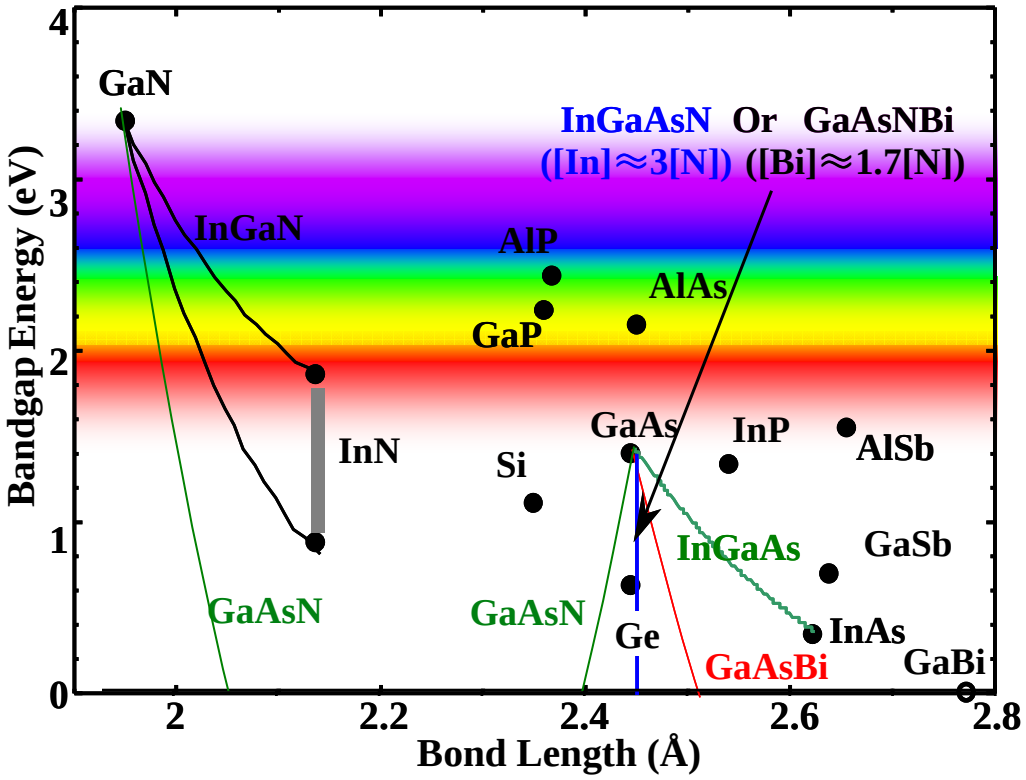

Figure 1.1 Bandgap energy vs. bond length for various III-V compound and elemental semiconductors. [1, 2, 21-25] The points correspond to the energy bandgap and bond length for each elemental or binary semiconductor, and the lines connecting those points correspond to the alloys. The shaded region between the two points for InN indicates the uncertainty in the InN bandgap energy.

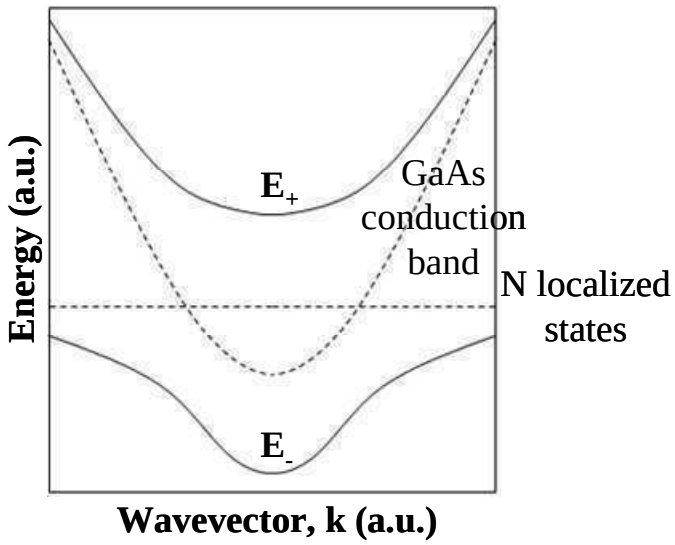

Figure 1.2 Schematics of dispersion relationships for subbands (solid lines) of $GaN_{0.01}As_{0.99}$ using the band anticrossing model. The dotted lines represent the unperturbed energies of the N-induced localized states and the GaAs CB; the solid line represent the hybridized E_- and E_+ bands.

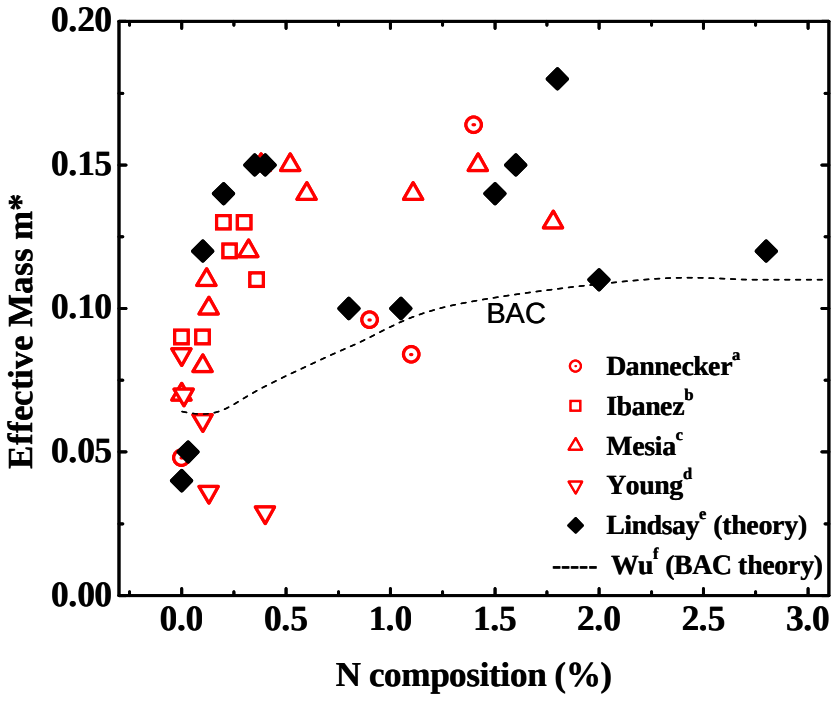

Figure 1.3 A summary of electron effective mass as a function of N composition determined by various experimental methods and by calculation. The m_e^* predicted by BAC model is significantly lower than the experimental observation. The nonmonotonic trend of m_e^* is well captured by the calculation including the resonant N levels. [a]by Tassilo Dannecker (the author's colleague at University of Michigan), [b]Ref.[100] [c]Ref.[98] [d]Ref.[101], [e]Ref.[92] , [f]Ref.[11]

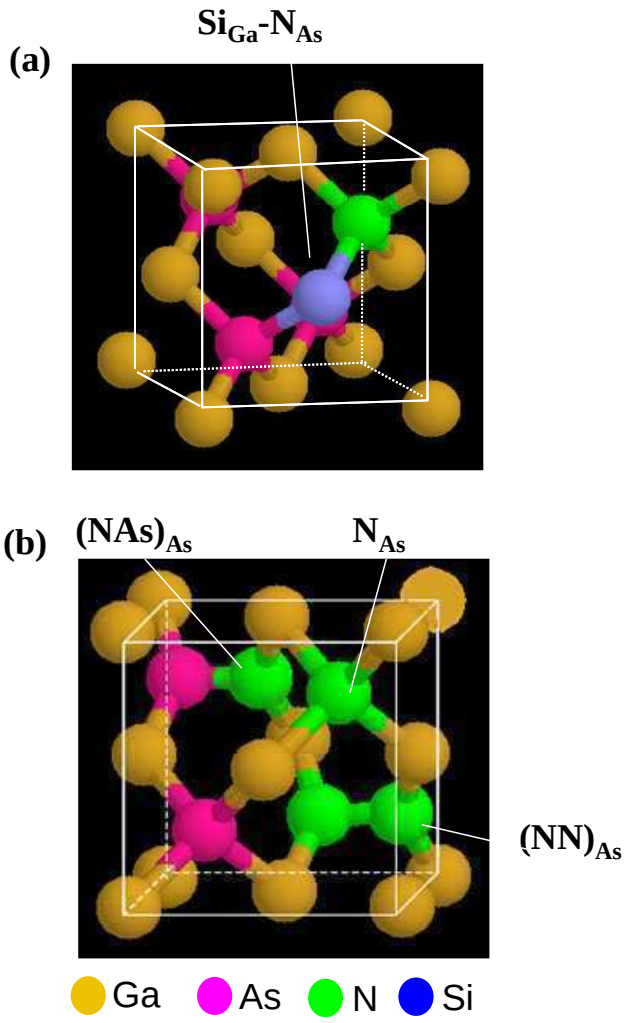

Figure 1.4 Several possible configurations for N incorporation in GaAs, including (a) extrinsic defect Si-N pair and (b) N substitutional, N_{As}, and intrinsic defects NN split interstitial, $(NN)_{As}$, and NAs split interstitial, $(NAs)_{As}$.

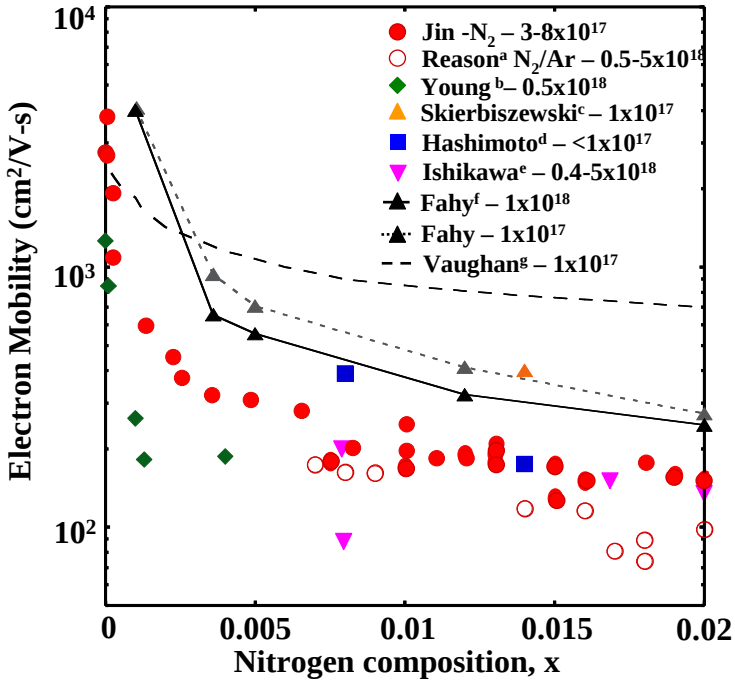

Figure 1.5 Electron mobility, μ, vs. N composition for bulk $GaAs_{1-x}N_x$ films of various targeted free carrier concentrations, in units of cm^{-3}. The solid (open) circles represent our results for films grown with pure N_2 (N_2/Ar mixture) as the N source gas. Other solid points are measured μ collected from literature. The calculated μ by Fahy and Vaughan are also included for comparison. The measured μ decreases substantially with increasing N composition, and is lower than the prediction of all the theories. [a]see Ref.[138]. [b]see Ref.[101] [c]see Ref.[139] [d]see Ref.[128] [e]see Ref.[13] [f]see Ref.[110] [g]see Ref.[126]

1.9 References

[1]W. G. Bi and C. W. Tu, Appl. Phys. Lett. **70**, 1608 (1997).

[2]K. Uesugi, N. Morooka and I. Suemune, Appl. Phys. Lett. **74**, 1254 (1999).

[3]S. G. Spruytte, M. C. Larson, W. Wampler, C. W. Coldren, H. E. Petersen and J. S. Harris, J. Cryst. Growth **227**, 506 (2001).

[4]U. Tisch, E. Finkman and J. Salzman, Appl. Phys. Lett. **81**, 463 (2002).

[5]R. S. Goldman, R. M. Feenstra, B. G. Briner, M. L. Osteen and R. J. Hauenstein, Appl. Phys. Lett. **69**, 3698 (1996).

[6]H. A. McKay, R. M. Feenstra, T. Schmidtling and U. W. Pohl, Appl. Phys. Lett. **78**, 82 (2001).

[7]S. B. Zhang, A. Janotti, S. H. Wei and C. G. Van de Walle, IEE P-Optoelectron. **151**, 369 (2004).

[8]S. Fahy and E. P. O'Reilly, Appl. Phys. Lett. **83**, 3731 (2003).

[9]P. R. C. Kent and A. Zunger, Phys. Rev. B **64**, 115208 (2001).

[10]P. R. C. Kent and A. Zunger, Phys. Rev. Lett. **86**, 2613 (2001).

[11]A. Lindsay and E. P. O'Reilly, Phys. Rev. Lett. **93**, 196402 (2004).

[12]J. Teubert, P. J. Klar, W. Heimbrodt, K. Volz, W. Stolz, P. Thomas, G. Leibiger and V. Gottschalch, Appl. Phys. Lett. **84**, 747 (2004).

[13]F. Ishikawa, G. Mussler, K. J. Friedland, H. Kostial, K. Hagenstein, L. Daweritz and K. H. Ploog, Appl. Phys. Lett. **87**, 262112 (2005).

[14]J. Li, P. Carrier, S. H. Wei, S. S. Li and J. B. Xia, Phys. Rev. Lett. **96**, 035505 (2006).

[15]K. M. Yu, W. Walukiewicz, J. Wu, D. E. Mars, D. R. Chamberlin, M. A. Scarpulla, O. D. Dubon and J. F. Geisz, Nat. Mater. **1**, 185 (2002).

[16]A. Janotti, P. Reunchan, S. Limpijumnong and C. G. Van de Walle, Phys. Rev. Lett. **100**, 045505 (2008).

[17]S. B. Zhang and S.-H. Wei, Phys. Rev. Lett. **86**, 1789 (2001).

[18]M. Reason, H. A. McKay, W. Ye, S. Hanson, R. S. Goldman and V. Rotberg, Appl. Phys. Lett. **85**, 1692 (2004).

[19]S. G. Spruytte, C. W. Coldren, J. S. Harris, W. Wampler, P. Krispin, K. Ploog and M. C. Larson, J. Appl. Phys. **89**, 4401 (2001).

[20]L. Vegard, Z. Phys. **5**, 17 (1921).

[21]I. Vurgaftman, J. R. Meyer and L. R. Ram-Mohan, J. Appl. Phys. **89**, 5815 (2001).

[22]H. J. Hovel and J. J. Cuomo, Appl. Phys. Lett. **20**, 71 (1972).

[23]T. L. Tansley and C. P. Foley, J. Appl. Phys. **59**, 3241 (1986).

[24]P. Specht, J. C. Ho, X. Xu, R. Armitage, E. R. Weber, R. Erni and C. Kisielowski, Solid State Commun. **135**, 340 (2005).

[25]B. Monemar, P. P. Paskov and A. Kasic, Superlattices Microstruct. **38**, 38 (2005).

[26]M. Weyers and M. Sato, Appl. Phys. Lett. **62**, 1396 (1993).

[27]M. Weyers, M. Sato and H. Ando, Jpn. J. Appl. Phys. 2 **31**, L853 (1992).

[28]M. Kondow, K. Uomi, K. Hosomi and T. Mozume, Jpn. J. Appl. Phys. 2 **33**, L1056 (1994).

[29]K. Uesugi and I. Suemune, Jpn. J. Appl. Phys. 2 **36**, L1572 (1997).

[30]S. H. Wei and A. Zunger, Phys. Rev. Lett. **76**, 664 (1996).

[31]L. Bellaiche, S. H. Wei and A. Zunger, Phys. Rev. B **54**, 17568 (1996).

[32]L. Bellaiche, S. H. Wei and A. Zunger, Appl. Phys. Lett. **70**, 3558 (1997).

[33]L. Bellaiche, S. H. Wei and A. Zunger, Phys. Rev. B **56**, 10233 (1997).

[34]Vanvecht.Ja and Bergstre.Tk, Phys. Rev. B **1**, 3351 (1970).

[35]Richards.D and R. Hill, J Phys. C Solid State **5**, 821 (1972).

[36]J. J. Gersten and F. W. Smith, *The physics and chemistry of materials.* (Wiley Interscience, New York, USA, 2001)

[37]W. Gordy and W. J. O. Thomas, J. Chem. Phys. **24**, 439 (1956).

[38]S. Tixier, S. E. Webster, E. C. Young, T. Tiedje, S. Francoeur, A. Mascarenhas, P. Wei and F. Schiettekatte, Appl. Phys. Lett. **86**, 112113 (2005).

[39]M. Fischer, D. Gollub and A. Forchel, Jpn. J. Appl. Phys. 1 **41**, 1162 (2002).

[40]D. Gollub, S. Moses, A. Fischer, M. Kamp and A. Forchel, Electron. Lett. **40**, 427 (2004).

[41]J. F. Geisz and D. J. Friedman, Semicond. Sci. Technol. **17**, 769 (2002).

[42]J. S. Harris, Semicond Sci Tech **17**, 880 (2002).

[43]L. H. Li, V. Sallet, G. Patriarche, L. Largeau, S. Bouchoule, K. Merghem, L. Travers and J. C. Harmand, Electron. Lett. **39**, 519 (2003).

[44]H. Riechert, A. Ramakrishnan and G. Steinle, Semicond Sci Tech **17**, 892 (2002).

[45]G. Steinle, F. Mederer, M. Kicherer, R. Michalzik, G. Kristen, A. Y. Egorov, H. Riechert, H. D. Wolf and K. J. Ebeling, Electron. Lett. **37**, 632 (2001).

[46]M. R. Gokhale, J. Wei, P. V. Studenkov, H. Wang and S. R. Forrest, IEEE Photonic Tech. L. **11**, 952 (1999).

[47]S. R. Kurtz, A. A. Allerman, E. D. Jones, J. M. Gee, J. J. Banas and B. E. Hammons, Appl. Phys. Lett. **74**, 729 (1999).

[48]P. C. Chang, N. Y. Li, A. G. Baca, H. Q. Hou, C. Monier, J. R. Laroche, F. Ren and S. J. Pearton, IEEE Electron. Dev. Lett. **22**, 113 (2001).

[49]C. Monier, A. G. Baca, P. C. Chang, N. Y. Li, H. Q. Hou, F. Ren and S. J. Pearton, Electron. Lett. **37**, 198 (2001).

[50]P. M. Asbeck, R. J. Welty, C. W. Tu, H. P. Xin and R. E. Welser, Semicond. Sci. Technol. **17**, 898 (2002).

[51]M. Kondow, K. Uomi, A. Niwa, T. Kitatani, S. Watahiki and Y. Yazawa, Jpn. J. Appl. Phys. 1 **35**, 1273 (1996).

[52]M. Kondow, T. Kitatani, S. Nakatsuka, M. C. Larson, K. Nakahara, Y. Yazawa, M. Okai and K. Uomi, IEEE J. Sel Top. Quant. **3**, 719 (1997).

[53]M. Kondow, T. Kitatani, K. Nakahara and T. Tanaka, Jpn. J. Appl. Phys. 2 **38**, L1355 (1999).

[54]T. Miyamoto, K. Takeuchi, F. Koyama and K. Iga, IEEE Photonic Tech. L. **9**, 1448 (1997).

[55]S. Sato and S. Satoh, IEEE Photonic Tech. L. **11**, 1560 (1999).

[56]B. Borchert, A. Y. Egorov, S. Illek, M. Komainda and H. Riechert, Electron. Lett. **35**, 2204 (1999).

[57]M. Fischer, M. Reinhardt and A. Forchel, Electron. Lett. **36**, 1208 (2000).

[58]I. A. Buyanova, W. M. Chen and B. Monemar, MRS Internet J. Nitride Semicond. Res. **6**, 2 (2001).

[59]M. Kondow, S. Nakatsuka, T. Kitatani, Y. Yazawa and M. Okai, Jpn. J. Appl. Phys. 1 **35**, 5711 (1996).

[60]S. R. Forrest, P. H. Schmidt, R. B. Wilson and M. L. Kaplan, Appl. Phys. Lett. **45**, 1199 (1984).

[61]M. Hetterich, M. D. Dawson, A. Y. Egorov, D. Bernklau and H. Riechert, Appl. Phys. Lett. **76**, 1030 (2000).

[62]M. Galluppi, L. Geelhaar and H. Riechert, Applied Physics Letters **86**, 131925 (2005).

[63]E. T. Yu, J. O. McCaldin and T. C. McGill, Solid State Physics: Advances in Research and Applications **46**, 1 (1992).

[64]S. R. Bank, H. Bae, L. L. Goddard, H. B. Yuen, M. A. Wistey, R. Kudrawiec and J. S. Harris, IEEE J. Sel. Top. Quant. **43**, 773 (2007).

[65]D. J. Friedman, J. F. Geisz, S. R. Kurtz and J. M. Olson, J. Crys. Growth **195**, 409 (1998).

[66]P. H. Wu, Y. K. Su, Y. C. Tzeng, H. F. Hong, K. Y. Chu and Y. R. Chen, Semicond Sci Tech **22**, 549 (2007).

[67]M. Yamaguchi, H. Suzuki, K. I. Nishimura, N. Kojima, Y. Ohsita and Y. Okada, Proceedings of Ises Solar World Congress 2007: Solar Energy and Human Settlement, Vols I-V 1028 (2007).

[68]R. R. King, C. M. Fetzer, D. C. Law, K. M. Edmondson, H. Yoon, G. S. Kinsey, D. D. Krut, J. H. Ermer, P. Hebert, B. T. Cavicchi and N. H. Karam, Conference Record of the 2006 IEEE 4th World Conference on Photovoltaic Energy Conversion, Vols 1 and 2 1757 (2006).

[69]S. Kurtz, D. Friedman, J. Geisz and W. McMahon, J. Crys. Growth **298**, 748 (2007).

[70]A. Freundlich, A. Fotkatzikis, L. Bhusal, L. Williams, A. Alemu, W. Zhu, J. A. H. Coaquira, A. Feltrin and G. Radhakrishnan, J. Crys. Growth **301**, 993 (2007).

[71]H. P. Hjalmarson, P. Vogl, D. J. Wolford and J. D. Dow, Phys. Rev. Lett. **44**, 810 (1980).

[72]W. Shan, W. Walukiewicz, K. M. Yu, J. W. Ager, E. E. Haller, J. F. Geisz, D. J. Friedman, J. M. Olson, S. R. Kurtz and C. Nauka, Phys. Rev. B **62**, 4211 (2000).

[73]W. Shan, W. Walukiewicz, K. M. Yu, J. W. Ager, E. E. Haller, J. F. Geisz, D. J. Friedman, J. M. Olson, S. R. Kurtz, H. P. Xin and C. W. Tu, Phys. Status Solidi B **223**, 75 (2001).

[74]W. Shan, K. M. Yu, W. Walukiewicz, J. Wu, J. W. Ager and E. E. Haller, J. Phys-Condense Mat. **16**, S3355 (2004).

[75]W. Shan, K. M. Yu, W. Walukiewicz, J. W. Beeman, J. Wu, J. W. Ager, M. A. Scarpulla, O. D. Dubon and E. E. Haller, Appl. Phys. Lett. **84**, 924 (2004).

[76]P. R. C. Kent and A. Zunger, Phys. Status Solidi B **228**, 253 (2001).

[77]P. R. C. Kent, L. Bellaiche and A. Zunger, Semicond Sci Tech **17**, 851 (2002).

[78]A. Lindsay and E. P. O'Reilly, Solid State Commun. **118**, 313 (2001).

[79]A. Lindsay and E. P. O'Reilly, Solid State Commun. **112**, 443 (1999).

[80]W. Shan, W. Walukiewicz, J. W. Ager, E. E. Haller, J. F. Geisz, D. J. Friedman, J. M. Olson and S. R. Kurtz, Phys. Rev. Lett. **82**, 1221 (1999).

[81]W. Shan, W. Walukiewicz, J. W. Ager, E. E. Haller, J. F. Geisz, D. J. Friedman, J. M. Olson and S. R. Kurtz, J. Appl. Phys. **86**, 2349 (1999).

[82]I. Vurgaftman and J. R. Meyer, J. Appl. Phys. **94**, 3675 (2003).

[83]J. D. Perkins, A. Mascarenhas, Y. Zhang, J. F. Geisz, D. J. Friedman, J. M. Olson and S. R. Kurtz, Phys. Rev. Lett. **82**, 3312 (1999).

[84]E. D. Jones, N. A. Modine, A. A. Allerman, S. R. Kurtz, A. F. Wright, S. T. Tozer and X. Wei, Phys. Rev. B **60**, 4430 (1999).

[85]J. Endicott, J. Ibanez, A. Patane, L. Eaves, A. Bissiri, A. Hopkinson, R. Airey, G. Hill, D. Gollub and A. Forchel, Physica E **21**, 892 (2004).

[86]R. Kudrawiec, J. A. Gupta, M. Motyka, M. Gladysiewicz, J. Misiewicz and X. Wu, Appl. Phys. Lett. **89**, 171914 (2006).

[87]J. Plaza, J. L. Castano, B. J. Garcia, H. Carrere and E. Bedel-Pereira, Appl. Phys. Lett. **86**, 121918 (2005).

[88]T. Mattila, S. H. Wei and A. Zunger, Phys. Rev. B **60**, R11245 (1999).

[89]P. N. Hai, W. M. Chen, I. A. Buyanova, H. P. Xin and C. W. Tu, Appl. Phys. Lett. **77**, 1843 (2000).

[90]G. B. von Hogersthal, A. Polimeni, F. Masia, M. Bissiri, M. Capizzi, D. Gollub, M. Fischer and A. Forchel, Phys. Rev. B **67**, 233304 (2003).

[91]G. Pettinari, F. Masia, A. Polimeni, M. Felici, A. Frova, M. Capizzi, A. Lindsay, E. P. O'Reilly, P. J. Klar, W. Stolz, G. Bais, M. Piccin, S. Rubini, F. Martelli and A. Franciosi, Phys. Rev. B **74**, 245202 (2006).

[92]A. Lindsay and E. P. O'Reilly, Physica E **21**, 901 (2004).

[93]S. B. Healy, A. Lindsay and E. P. O'Reilly, Physica E **32**, 249 (2006).

[94]S. B. Healy, A. Lindsay and E. P. O'Reilly, IEE P-Optoelectron. **151**, 397 (2004).

[95]S. W. Johnston and S. R. Kurtz, J. Vac. Sci. Tech. A **24**, 1252 (2006).

[96]P. R. C. Kent and A. Zunger, Appl. Phys. Lett. **79**, 2339 (2001).

[97]S. Kurtz, S. Johnston and H. M. Branz, Appl. Phys. Lett. **86**, 113506 (2005).

[98]F. Masia, G. Pettinari, A. Polimeni, M. Felici, A. Miriametro, M. Capizzi, A. Lindsay, S. B. Healy, E. P. O'Reilly, A. Cristofoli, G. Bais, M. Piccin, S. Rubini, F. Martelli, A. Franciosi, P. J. Klar, K. Volz and W. Stolz, Phys. Rev. B **73**, 073201 (2006).

[99]E. P. O'Reilly, A. Lindsay and S. Fahy, J. Phys-Condense Mat. **16**, S3257 (2004).

[100]J. Ibanez, R. Cusco, E. Alarcon-Llado, L. Artus, A. Patane, D. Fowler, L. Eaves, K. Uesugi and I. Suemune, J. Appl. Phys. **103**, 103528 (2008).

[101]D. L. Young, J. F. Geisz and T. J. Coutts, Appl. Phys. Lett. **82**, 1236 (2003).

[102]A. Polimeni, G. Ciatto, L. Ortega, F. Jiang, F. Boscherini, F. Filippone, A. A. Bonapasta, M. Stavola and M. Capizzi, Phys. Rev. B **68**, 085204 (2003).

[103]G. Baldassarri, M. Bissiri, A. Polimeni, M. Capizzi, M. Fischer, M. Reinhardt and A. Forchel, Appl. Phys. Lett. **78**, 3472 (2001).

[104]S. Sanna and V. Fiorentini, Phys. Rev. B **69**, 125208 (2004).

[105]A. Polimeni, G. B. H. von Hogersthal, F. Masia, A. Frova, M. Capizzi, S. Sanna, V. Fiorentini, P. J. Klar and W. Stolz, Phys. Rev. B **69**, 041201 (2004).

[106]G. Ciatto, F. Boscherini, A. A. Bonapasta, F. Filippone, A. Polimeni and M. Capizzi, Phys. Rev. B **71**, 201301 (2005).

[107]F. Jiang, M. Stavola, M. Capizzi, A. Polimeni, A. A. Bonapasta and F. Filippone, Phys. Rev. B **69**, 041309 (2004).

[108]K. M. Yu, W. Walukiewicz, J. Wu, W. Shan, J. W. Beeman, M. A. Scarpulla, O. D. Dubon, M. C. Ridgway, D. E. Mars and D. R. Chamberlin, Appl. Phys. Lett. **83**, 2844 (2003).

[109]K. M. Yu, J. Wu, W. Walukiewicz, W. Shan, J. W. Beeman, D. E. Mars, D. R. Chamberlin, M. A. Scarpulla, O. D. Dubon, M. C. Ridgway and J. F. Geisz, Physica B **340**, 389 (2003).

[110]S. Fahy, A. Lindsay, H. Ouerdane and E. P. O'Reilly, Phys. Rev. B **74**, 035203 (2006).

[111]E. Arola, J. Ojanen, H.-P. Komsa and T. T. Rantala, Phys. Rev. B **72**, 045222 (2005).

[112]S. B. Zhang and S.-H. Wei, Phys. Rev. Lett. **86**, 1789 (2001).

[113]Q. D. Zhuang, A. Krier and C. R. Stanley, J. Appl. Phys. **101**, 103536 (2007).

[114]M. Ramsteiner, D. S. Jiang, J. S. Harris and K. H. Ploog, Appl. Phys. Lett. **84**, 1859 (2004).

[115]P. Krispin, S. G. Spruytte, J. S. Harris and K. H. Ploog, Physica B **308**, 870 (2001).

[116]M. Adamcyk, J. H. Schmid, T. Tiedje, A. Koveshnikov, A. Chahboun, V. Fink and K. L. Kavanagh, Appl. Phys. Lett. **80**, 4357 (2002).

[117]T. Ahlgren, E. Vainonen-Ahlgren, J. Likonen, W. Li and M. Pessa, Appl. Phys. Lett. **80**, 2314 (2002).

[118]T. Ahlgren, E. Vainonen-Ahlgren, J. Likonen, W. Li and M. Pessa, Appl. Phys. Lett. **80**, 2314 (2002).

[119]J. N. Beaudry, R. A. Masut, P. Desjardins, R. Wei, M. Chicoine, G. Bentoumi, R. Leonelli, F. Schiettekatte and S. Guillon, J. Vac. Sci. Tech. A **22**, 771 (2004).

[120]G. Bisognin, D. De Salvador, C. Mattevi, M. Berti, A. V. Drigo, G. Ciatto, L. Grenouillet, P. Duvaut, P. Gilet and H. Mariette, J. Appl. Phys. **95**, 48 (2004).

[121]W. K. Loke, S. F. Yoon, S. Z. Wang, T. K. Ng and W. J. Fan, J. Appl. Phys. **91**, 4900 (2002).

[122]B. S. Ma, W. J. Fan, Y. X. Dang, W. K. Cheah and S. F. Yoon, Appl. Phys. Lett. **91**, 041905 (2007).

[123]S. M. Sze, *Semiconductor Devices: Physics and Technology* (Wiley, New York, 1985) pp. 48.

[124]D. J. Friedman, J. F. Geisz and A. J. Ptak, *Physics and Applications of Dilute Nitrides* (Taylor & Francis, 2004) pp. 371-394.

[125]F. Ishikawa, G. Mussler, K.-J. Friedland, H. Kostial, K. Hagenstein, L. Daweritz and K. H. Ploog, Appl. Phys. Lett. **87**, 262112 (2005).

[126]M. P. Vaughan and B. K. Ridley, Phys. Rev. B **72**, 075211 (2005).

[127]M. Reason, Y. Jin, H. A. McKay, N. Mangan, D. Mao, R. S. Goldman, X. Bai and C. Kurdak, J. Appl. Phys. **102**, 103710 (2007).

[128]A. Hashimoto, T. Yamaguchi, T. Suzuki and A. Yamamoto, J. Cryst. Growth **278**, 532 (2005).

[129]C. Skierbiszewski, P. Perlin, P. Wisniewski, T. Suski, W. Walukiewicz, W. Shan, J. W. Ager, E. E. Haller, J. F. Geisz, D. J. Friedman, J. M. Olson and S. R. Kurtz, Phys. Status Solidi B **216**, 135 (1999).

[130]S. Tomic, E. P. O'Reilly, P. J. Klar, H. Gruning, W. Heimbrodt, W. M. Chen and I. A. Buyanova, Phys. Rev. B **69**, 245305 (2004).

[131]J. S. Ng, W. M. Soong, M. J. Steer, M. Hopkinson, J. P. R. David, J. Chamings, S. J. Sweeney and A. R. Adams, J. Appl. Phys. **101**, 064506 (2007).

[132]M. Oueslati, M. Zouaghi, M. E. Pistol, L. Samuelson, H. G. Grimmeiss and M. Balkanski, Phys. Rev. B **32**, 8220 (1985).

[133]A. M. Mintairov, T. H. Kosel, J. L. Merz, P. A. Blagnov, A. S. Vlasov, V. M. Ustinov and R. E. Cook, Phys. Rev. Lett. **87**, 277401 (2001).

[134]A. M. Mintairov, P. A. Blagnov, J. L. Merz, V. M. Ustinov, A. S. Vlasov, A. R. Kovsh, J. S. Wang, L. Wei and J. Y. Chi, Physica E **21**, 385 (2004).

[135]D. J. Friedman and S. R. Kurtz, Prog. Photovoltaics **10**, 331 (2002).

[136]C. Baur, A. W. Bett, F. Dimroth, S. van Riesen, B. Kunert, M. Traversa, K. Volz and W. Stolz, Proceedings of 3rd World Conference on Photovoltaic Energy Conversion, Vols a-C 677 (2003).

[137]Y. Jin, Y. He, H. Cheng, R. M. Jock, T. Dannecker, M. Reason, A. M. Mintairov, C. Kurdak, J. L. Merz and R. S. Goldman, Appl. Phys. Lett. **95**, 092109 (2009).

[138]M. Reason, N. G. Rudawski, H. A. McKay, X. Weng, W. Ye and R. S. Goldman, J. Appl. Phys. **101**, 083520 (2007).

[139]C. Skierbiszewski, P. Perlin, P. Wisniewski, W. Knap, T. Suski, W. Walukiewicz, W. Shan, K. M. Yu, J. W. Ager, E. E. Haller, J. F. Geisz and J. M. Olson, Appl. Phys. Lett. **76**, 2409 (2000).

CHAPTER 2

EXPERIMENTAL PROCEDURES

2.1 Overview

This chapter describes the experimental procedures for the synthesis and characterization of (In)GaAsN films in this dissertation work.

All films were grown by molecular-beam epitaxy (MBE) on semi-insulating GaAs (001) substrate. During growth, the surface morphology was examined using reflection high-energy electron diffraction (RHEED). Post growth rapid thermal annealing (RTA) was applied for select samples. Following growth, X-ray rocking curve (XRC) measurements were performed to examine the crystalline quality and to estimate the N composition in the film. The surface morphology was inspected using atomic force microscopy (AFM). Rutherford backscattering (RBS) and nuclear reaction analysis (NRA) were performed in [001] channeling and non-channeling conditions to determine the total N concentration and N interstitial fraction. Photoluminescence (PL) spectra were collected to study the optical emission efficiency. Raman spectroscopy was performed to identify various N point defects related local vibration models in GaAsN.

The heart of the work in this dissertation is variable temperature transport measurements, which were performed on both GaAsN bulk films and AlGaAs/GaAsN heterostructures. Some of the samples were prepared into Van der Pauw geometry, while others were defined into Hall bar devices using photolithography. The variable temperature transport measurements include Hall effect, magnetoresistance, and persistent photoconductivity measurements. These measurements reveal valuable information on the carrier scattering processes, carrier localization, and N-related electronic states. All procedures were carried out by the author except where noted.

2.2 Molecular-Beam Epitaxy (MBE)

All the samples described in this dissertation were grown in a Modified Varian Gen II MBE system in Dr. Goldman's research laboratory in the Material Science and Engineering Department, University of Michigan. Molecular beam epitaxy (MBE) is a refined vacuum deposition technique used to prepare high quality epitaxial films one atomic layer at a time.[1, 2] In an ultra-high vacuum environment, molecular beams are produced by evaporation or sublimation from heated liquids and solids, which interact chemically on the surface by condensation of the elemental components, to form an epitaxial film.[3] Because the incoming molecules are reactive, growth can occur at conditions which are far from equilibrium. MBE is commonly used for the growth of (In)GaAsN films, [4-8] due to the ability to grow high purity crystals with lower defect concentrations, which is essential for improving the material electron mobility and optical emission efficiency as discussed in Section 1.5.

As shown schematically in Fig. 2.1, the Modified Varian Gen II chamber consists of a separately pumped growth chamber, buffer chamber, and load-lock, which are connected by magnetic transfer rods and trolleys. The growth chamber source flange houses 7 solid sources (In, Ga, Al, Si, Be, GaTe and As cracker), as well as a rf plasma source for the production of active N from an ultrahigh purity N_2 gas. The solid sources are contained in pyrolytic boron nitride (PBN) crucibles housed in Knudsen effusion cells. The flux of the molecular beam is exponentially dependent on the temperature of the effusion cell, which is typically controlled with heating filaments wrapped around the crucibles, and monitored by a thermocouple in contact with the crucible. For Ga, In, and As bulk-zone, the heating filaments are designed to provide extra heating in the area of

the crucible orifice and create a “hot lip”, to reduce the level of condensation in the crucible. The beam flux is measured using an ionization gauge which sits at the growth position. Computer controlled pneumatic shutters are used to control the exposure of each molecular beam. For the As source, the As flux is controlled with a needle valve in front of the As cell which can be adjusted between 0 an 300 mil. Samples are held in the growth position by the manipulator referred to as the CAR (for Continuous Azimuthal Rotation). The CAR is typically rotated to improve the uniformity of growth. The growth chamber also contains facilities for *in-situ* reflection high-energy electron diffraction (RHEED) and a residual gas analyzer (RGA) for *in-situ* mass spectrometry. The chamber pressure is monitored by an ionization gauge on the side wall of the chamber. The base pressure of the chamber during idling is ~ $2x10^{-9}$ Torr. When LN_2 is flowing through the cryopanel, the base pressure is lowered to less than $3x10^{-10}$ Torr. The chamber pressure ranges from $1x10^{-8}$ during the growth without N_2, to $3x10^{-5}$ Torr during the growth with N_2.

All films were grown on “epi-ready” GaAs substrates, which arrive from the manufacturer in a dry N_2 sealed container, ready for immediate introduction into the load-lock. All substrates were indium-mounted on heated molybdenum blocks (T>156°C), pre-baked at 150 °C for 8 hours in the load-lock, and outgassed at 180°C for at least 30 minutes in the buffer chamber. In the growth chamber, the substrate temperature was raised to 300 °C, at which point As_2 shutter was opened, providing an As_2 over pressure of ~ $5x10^{-6}$ Torr. The substrate temperature was then continuously raised until a transition in the RHEED pattern from diffuse rings to a streaky pattern was observed, indicating desorption of the surface oxide. For GaAs, oxide desorption has been reported to occur in

the range of 580 to 610 °C.[9, 10] Typically, the corresponding measured substrate temperature ranged from 750°C to 830°C. Since the substrate temperatures were determined via a thermocouple in contact with the backside of each molybdenum block, the oxide desorption temperature was used as an internal block calibration for each growth. Following oxide desorption, the block temperature was then increased an additional 30 °C and outgassed for 5 minutes to ensure that surface oxide was completely desorbed.

The N flux was controlled with a residual gas analyzer (RGA) and a mass flow controller (MFC) as follows: The RGA was used to monitor the partial pressure of 14 amu, and the MFC was adjusted to achieve a targeted value of the RGA 14 amu reading. For the (In)$GaAs_{1-x}N_x$ films grown at growth rate between 0.5 and 1 µm/hr, to achieve x between 0.005 and 0.025, the typical RGA14 value was in the range 2 - 6 $x10^{-9}$ Torr, and the corresponding MFC flows were in the range 0.2 – 0.8 sccm. It is worth noting that the limited precision of the MFC[11] was found to lead to a large spread of N composition in GaAsN films for a fixed MFC flow; thus, the MFC was not directly used to control the N flux.

To strike the plasma, the input power was gradually increased to 400 – 500 Watt with a fairly high N flow rate, i.e. MFC flow ~ 0.5 sccm. If the plasma chamber had been recently vented or idle in low vacuum condition (a few millitorr) for more than a month, the plasma can be difficult to strike, even with the high N_2 flow rate. In this case, the manufacturer suggested the following: with the plasma power at 500 Watt, close the N_2 gas line for a few seconds and then immediately reopen it. This “trick” proved to be efficient in most cases.

2.3 Reflection High-Energy Electron Diffraction

In-situ monitoring of growth rates, incorporation rate ratios and surface reconstruction during growth was accomplished using a Staib RH 30 RHEED gun, typically operating at 18 KV.

The intensity oscillations in the RHEED streaks occurs as film growth begins; assuming that the time for one oscillation corresponds to the growth of one complete monolayer, the growth rate is extracted from the RHEED oscillation frequency.[12 13, 14] A typical RHEED oscillation is shown in Fig. 2.2 (a). RHEED was also used to determine the minimum amount of As flux needed to maintain the proper stoichiometry, often termed the "incorporation rate ratio". We typically monitor the [110] direction of (2x4) pattern to determine the incorporation ratio of GaAs. This measurement starts with a sample growing at the growth temperature with both As and Ga shutter opened, so that the sample surface is As terminated. The As shutter is then closed for a few seconds, causing the surface to become Ga terminated and the RHEED pattern to transform from 2x to 4x. The As shutter is then reopened with the Ga shutter still open; the time required for the surface to change back to 2x reconstruction is recorded. Shown in Fig. 2.2 (b) is a typical plot of RHEED intensity as a function of measurement time for the incorporation rate ratio measurement, where t_1 is the moment when the As shutter is closed, t_2 is the moment when the As shutter is reopened, and t_3 is the moment when the growth recovered to the As terminated growth mode. An incorporation rate ratio is expressed as the total time the Ga shutter is open until the surface recovers divided by the time it takes for the surface to recover after the As shutter is reopened, or

$$\left(\frac{As}{Ga}\right)_{inc} = \frac{t_3 - t_1}{t_3 - t_2} = \frac{t_{Ga-open}}{t_{As-open}} \tag{2.1}$$

For growth of GaAs and AlAs, streaky RHEED patterns are typically observed obtained using an incorporation rate ratio, $(\frac{As}{Ga})_{inc}$, in the range 1.3 to 1.8.[15] In this work, we aimed for $(\frac{As}{Ga})_{inc}$ of 1.4 - 1.5. If $(\frac{As}{Ga})_{inc}$ >>1.5, the As pressure was considered to be too high and the As needle valve setting was decreased. If $(\frac{As}{Ga})_{inc}$ <<1.4, the As pressure was considered to be too low and the As needle valve setting was increased. In this dissertation work, our films were typically grown at a growth rate of 0.5 to 1 μm/hr, with an As_2 cracker needle valve setting 120 - 190 mil, and an incorporation rate ratio of 1.4 to 1.5.

2.4 Rapid thermal annealing

For select (In)$GaAs_{1-x}N_x$ films, post-growth rapid thermal annealing (RTA) was performed, using a JetFirst-150 Rapid Thermal Processor in the Lurie Nanofabrication Laboratory (LNF) at the University of Michigan. As shown in the schematic in Fig. 2.3, a 4 inch silicon wafer was used as the sample holder, with the substrate temperature determined by a type K thermocouple in contact with the bottom of the Si wafer. The samples were illuminated from the top with a halogen lamp apparently capable of temperature ramping at a rate of 20 °C/sec.

For each RTA sequence, As out-diffusion was prevented by capping each sample with a new GaAs substrate, polished side facing the film. RTA was then performed in the temperature range between 650°C to 800°C for 60s, in an atmospheric pressure N_2 ambient.

2.5 High Resolution X-ray Diffraction

To determine the lattice constant of the epi (In)GaAsN films, double-axis x-ray rocking curves (XRC) were performed on bulk-like (In)GaAsN films (i.e. >500 nm in thickness). All XRC's were carried out using a BEDE D^1 system, which has been described in detail in Section 2.5 of M.Reason's Ph.D. thesis.[16]

In the XRC measurements, the sample was "rocked" about the substrate Bragg angle, while the detector remained fixed at $2\theta_B$. Two sets of reflections, the symmetric (004) and asymmetric glancing-incidence (224), were measured. A schematic of these geometries is shown in Fig. 2.4.[17] To average out any epilayer tilt, each set of reflections was measured at φ = 0° and φ = 180°. To determine the epilayer peak position with respect to that of the substrate, the separation between the substrate and epilayer peaks was determined by fitting to Gaussians or Lorentzians. To calculate the N composition and strain relaxation, the epilayer-substrate peak separations in the (004) and (224) geometries were then input into the Bede software called "Peak Split". Using the epilayer-substrate peak separations, "Peak Split" calculates the in-plane and out-of-plane strains, which are then used to find the epilayer lattice parameters and N composition, assuming a linear interpolation of binary lattice parameters. The details of these analyses are described in Appendix A.2 of M. Reason's Ph.D. thesis.[16] It is important to note that some of the terminologies used in Peak Split software are different from those commonly used in XRC analysis. In particular, $\frac{a_{film_{//}} - a_{sub}}{a_{sub}}$ and $\frac{a_{epi_{\perp}} - a_{sub}}{a_{sub}}$, commonly referred to as "in-plane" and "out-of-plane strain", are referred to by Peak Split as "Parallel Mismatch" and "Perpendicular Mismatch".

2.6 Atomic Force Microscopy

The surface morphology of GaAsN films was investigated using tapping mode atomic force microscopy (AFM) with Digital Instruments Nanoscope III AFM in the Electron Microbeam Analysis Laboratory. The piezoelectric scanners typically move the probe in a curved motion over the surface, which results in a "Bowing" in the AFM image. Therefore, all as-collected images were "flattened" using the Digital Instruments software, which is basically subtracting a polynomial function (usually order 2 or 3) from the image. A variety of other image analysis functions were performed using the software, including section analysis, roughness measurements, and power spectral density (PSD) analysis. Details of these procedures are explained in Section 2.7 of X.Weng's Ph.D. Thesis.[17]

2.7 Ion Beam Analysis

Nuclear reaction analysis (NRA) and Rutherford backscattering spectrometry (RBS) of GaAsN and GaAs films were performed in both the [001] channeling and non-channeling conditions. The ion beam measurements were initially performed at the Michigan Ion Beam Laboratory (MIBL) by Dr. V. Rotberg using a General Ionex 1.7 MV Tandetron accelerator. Later measurements in MIBL were performed by Dr. F. Naab, with a few modifications to the experimental setup. The reminder of the measurements were performed by Dr. Y Wang of the Ion Beam Material Laboratory, at Los Alamos National Laboratory (LANL). The author participated in all ion beam measurements. A table comparing the key features of the three ion beam measurement

setups in MIBL and LANL is presented in Appendix B.2. The rest of this section will focus on the description of the experimental setup used at LANL.

Figure 2.5 shows a schematic of the RBS and NRA experiment setup. 1.2 MeV positively charged deuterons ($^1_1$H or d) were collimated into a beam and directed at the GaAs(N) sample surface. The total number of ions incident on the sample was measured by a charge integrator electrically connected to the sample holder. In addition, to prevent the inclusion of sputtered electrons in the incident ion dose measurement, a Faraday cup was utilized to produce an electric field around the sample.[18] The backscattered ions were collected by two charged-particle radiation detectors, one for NRA signal detection, and the other for RBS signal detection. Both detectors have solid angles $\Omega = 60$ milli-steradians (msr). They were mounted symmetrically at scattering angles of $\theta = 150°$, at which angle the NRA reaction cross-section has been characterized.[19, 20] A 26 μm Kapton film was placed in front of the NRA detector to filter out backscattered low energy deuterons and prevent saturation of the detector.[21] The counts of scattered ions collected by both detectors were plotted as a function of their channels, and outputted as NRA and RBS spectrum, as shown in Fig. 2.6 and Fig. 2.7, respectively. In these plots, the channel number is linearly dependent on the energy of the emitted particles, and the larger channel numbers represent higher energy. The beam alignment procedure used at LANL is described in Appendix B.3. All ion beam measurements were repeated multiple times for greater accuracy.

Typical RBS spectra for a GaAs film in channeling and non-channeling conditions are shown in Fig. 2.6. Since the channels near the edge of the spectra correspond to incident ions that have undergone scattering from only the top few nm of

the sample, these high energy particles were used to calculate χ_{min}(GaAs). The channels away from the edge were not used in this analysis, since they correspond to incident ions that travel further into the film and undergo multiple scattering events, which introduce significant errors in the backscattering analysis. Therefore, χ_{min}(GaAs) was defined as the ratio of the channeling and non-channeling yields of the top 4-5 channels.

For NRA measurements, to identify the channel number associated with specific N-related reactions, a TiN film was used as the reference sample. The stoichiometry of this TiN film was confirmed using NRA and RBS measurements with a deuterium beam to measure the N and Ti concentrations, respectively. Shown in Fig. 2.8 is a typical NRA spectrum from a TiN film. N-related peaks associated with several nuclear reactions are labeled, including $^{14}N(d,\alpha)^{12}C$ and $^{14}N(d,p)^{15}N$. Interestingly, the reaction $^{14}N(d,\alpha)^{12}C$, which corresponds to ${}^{2}_{1}H+{}^{14}_{7}N\rightarrow{}^{16}_{8}O\rightarrow{}^{4}_{2}He+{}^{12}_{6}C+E$, has two emitted particles, α_0 and α_1, which are easily distinguishable from the background. Therefore, the quantitative analysis of the total and interstitial N fraction was accomplished using the α_0 and α_1 yields.

The total N concentration for each sample was calculated directly by using the non-channeling NRA yield, *Y*, the cross-section of the nuclear reaction, σ, the solid angle of the NRA detector, Ω, the epi-film thickness, *t*, and the total charge, Q, as follows:[16]

$$N = Y / \sigma \cdot \Omega \cdot Q \cdot t \tag{2.2}$$

The total N concentration in GaAsN film was also calculated by comparing the sample NRA yield with that of the TiN film with known N composition. The advantage of this method is that it does not depend on knowledge of the absolute values of the incident

charge and the detector solid angle, and thus reduces the sources of measurement error. The fraction of N incorporating interstitially, f_{int}, was then calculated from the yields of the RBS on GaAs films and NRA on GaAsN films, based upon an assumption that the $GaAs_{1-x}N_x$ is stoichiometric, i.e., $f_{Ga}=f_{As}+f_N$. These calculations are also described in detail in Section A.3 of M.Reason's Ph.D. thesis.[16]

2.8 Variable Temperature Hall and magnetoresistance Measurements

To determine the *T*-dependence of the electronic properties of (In)GaAsN films, transport measurements were implemented in both Van der Pauw and Hall bar geometries, and variable *T* resistivity and Hall measurements were performed from 1.6 K to room *T*. The Hall bars were fabricated with standard photolithography process and e-beam evaporation in the Lurie Nanofabrication Laboratory (LNF) at University of Michigan. The room temperature Hall and resistivity measurement were performed in Prof. Goldman's lab in the MSE department. The Variable Temperature Hall and magnetoresistance measurements were carried out at Prof. Cagliyan Kurdak's research laboratory in the Physics Department, University of Michigan, by Yu Jin, with the help from Ryan Jock, Christer Akouala, Niall Mangan, and Hailing Cheng.

Figure 2.8 shows a schematic of the Van der Pauw sample geometry.[17] For this purpose, the samples were cleaved into 5 mm by 5 mm squares, and small (~0.5 mm^2) indium contacts were deposited on each of the four corners. The samples were then annealed at 410 °C for 2 minutes in atmosphere pressure N_2 to form ohmic contacts. 25 µm diameter gold wire was then manually bonded to each contact and subsequently soldered to the sample holder. The Van der Pauw geometry samples were straightforward

to fabricate, but have two intrinsic sources of error. First, due to the finite size of the contacts, the error induced in the resistance measurement is:

$$\frac{\Delta R}{R} \sim \frac{d^2}{D^2} \tag{2.3}$$

where d is the dimension of the contact and D is the dimension of sample.[22] The second source of error is the asymmetric shape of the sample. If the Van der Pauw sample is not perfectly square, a correction factor needs to be considered as follows:

$$\rho_{real} = f \cdot \rho_{measured} \tag{2.4}$$

where $f \leq 1$, and depends on the degree of asymmetry of the sample geometry.[22] Alternatively, these errors are minimized by instead using the Hall bar geometry, as discussed next.

In this thesis, we also used an eight - arm gated Hall bar, adapted from Section 3.5 of A.Young's Ph.D. thesis.[23] Figure 2.9 is a schematic drawing of the gated Hall bar, showing the dimensions as well as the definitions of the different voltages measured. The detailed lithography recipe manner is described in Appendix D. Similar to the Van der Pauw samples, gold wires of 25 µm diameter were then manually bonded to each contact and soldered to the sample holder. For modulation-doped heterostructures, the free carrier concentration in the channel layer was controlled by front gating. Gate definition required one extra lithography step, namely, e-beam evaporation of 300 nm Al. To minimize leakage current along the top periphery of the mesa, the area of the gate was defined beyond the edge of the mesa by ~20 µm.

Prior to Hall and resistivity measurements, the ohmic nature of all contacts was verified using a Hewlett Packard 4156B precision semiconductor parameter analyzer.

For $GaAs_{1-x}N_x$ films with x = 0-0.02 and n-type doping concentration 0.5-5 x 10^{18} cm^{-3}, the contact resistance was typically within the range of 100 Ω – 10 KΩ.

For room temperature Hall and resistivity measurements, a DC current of 10-100 mA was sent between two contacts, using a Keithley 224 programmable current source. The voltage drop parallel to the current was measured using a Hewlett Packard 34420A nanovolt / microOhm meter in the absence of a magnetic field. The voltage drop perpendicular to the current was measured in the presence of a magnetic field, ~ 0.1 Tesla. The default input impedance of the voltmeter is 10 MΩ, which can be used to measure the sample with contact resistance < 1 MΩ. For samples with Ohmic contact but contact resistance > 1 MΩ, the input impedance of the voltmeter needs to be switched to > 10 GΩ. From these measurements, the electron mobility, μ, and free carrier concentration, n, were determined using ASTM Standard F76.[24]

For the variable temperature (1.6K to room temperature) Hall and magnetoresistance measurement, the sample was mounted in a cryostat equipped with a superconducting magnet, as shown in Fig. 2.10. The cryostat has three shells: a vacuum outer shell used to insulate heat exchange in order to maintain the low temperature in the chamber; a middle shell filled with LHe, and an inner shell as the sample chamber, which is kept at low pressure by a mechanical pump. The sample chamber can be cooled to 1.6K by opening a needle valve at the bottom of the sample chamber connecting the middle and inner shell. When the needle valve is opened, LHe flows into the inner shell and becomes vaporized due to the low pressure in the sample chamber, thus, cooling the chamber to below LHe temperatures. A heater is also located at the bottom of the sample chamber, so that the chamber can be heated up to room temperature. A current is passed

through the NbTi superconducting wire from -72 to +72 A (ramp rate up to 0.6 A/s), resulting in a magnetic field ranging from –8 to +8 Tesla (the conversion between Amp and Tesla is determined to be 10.62, i.e. magnetic field =10.62 x current). Two Stanford lock-in amplifiers were used to measure the transverse and longitudinal voltage across the contact probes. The Lock-ins enable simultaneous measurement of both the in-phase (resistance) and the out-of-phase (capacitance) component of the impedance. When the magnitude of the out-of-phase signal is > 1/10 of the in-phase signal, the data is considered to be faulty, since measurement noise, such as the capacitance in the connecting cables, has become a significant fraction of the measured signal. This typically happened for high N compositions (>1.5%) and low measurement temperatures (<20K)

In addition, two light emitting diode (LED) assisted experiments were performed. In both cases, the LED was mounted directly above the sample, using two of the remaining leads on the sample holder. For the heterostructure samples discussed in Section 3.8 of this thesis, a commercial infrared light emitting diode (LED) was used to vary the carrier density in the channel layer. For the bulk GaAs(N) alloy films discussed in Section 4.4.3 of this thesis, the persistent photoconductivity effect was investigated using a LED with wavelength λ=940 nm. To minimize heating effects, the LED bias voltage was kept below 1 V, leading to a current of ~ 50 mA. The detailed procedures for each LED-assisted experiment will be described in Sections 3.3 and 4.3,.

2.9 Photoluminescence and Raman spectroscopy

To determine the optical emission efficiency of select GaAsN films, 3K to room temperature Photoluminescence (PL) spectra were performed with a 488 nm Ar laser operating at 6.4-83 mW/cm^2 (attenuation 0-2 and exposure time 1-10 seconds) and an HR320 spectrometer equipped with liquid nitrogen cooled IGA detector. The PL measurements were performed by Ms. Yan He in Prof. J. L. Merz's group in the Electrical Engineering Department, University of Notre Dame,

In addition, resonant Raman spectroscopy was used to detect the local vibrational modes, presumably associated with N-related defect states. The resonant Raman spectroscopy uses lasers with frequencies at or close to the target vibrational modes, so that the intensity of these vibrations is enhanced and can be detected. Raman spectra were obtained using a Renishaw inVia Raman microscope at the Center for Nanoscale Materials at Argonne National Laboratory.[25] For these measurements, a 633 nm laser operating at 5 mW was used, The laser was focused to a 1 μm spot using a 50x objective lens. Raman scattered light was collected using 180º backscattering geometry and dispersed on a cooled CCD detector using an 1800 g/mm grating. The signal integration time was 60 sec. The Raman measurements were performed by Dr. Mintairov of the Electrical Engineering Department, University of Notre Dame.

2.10 Figures

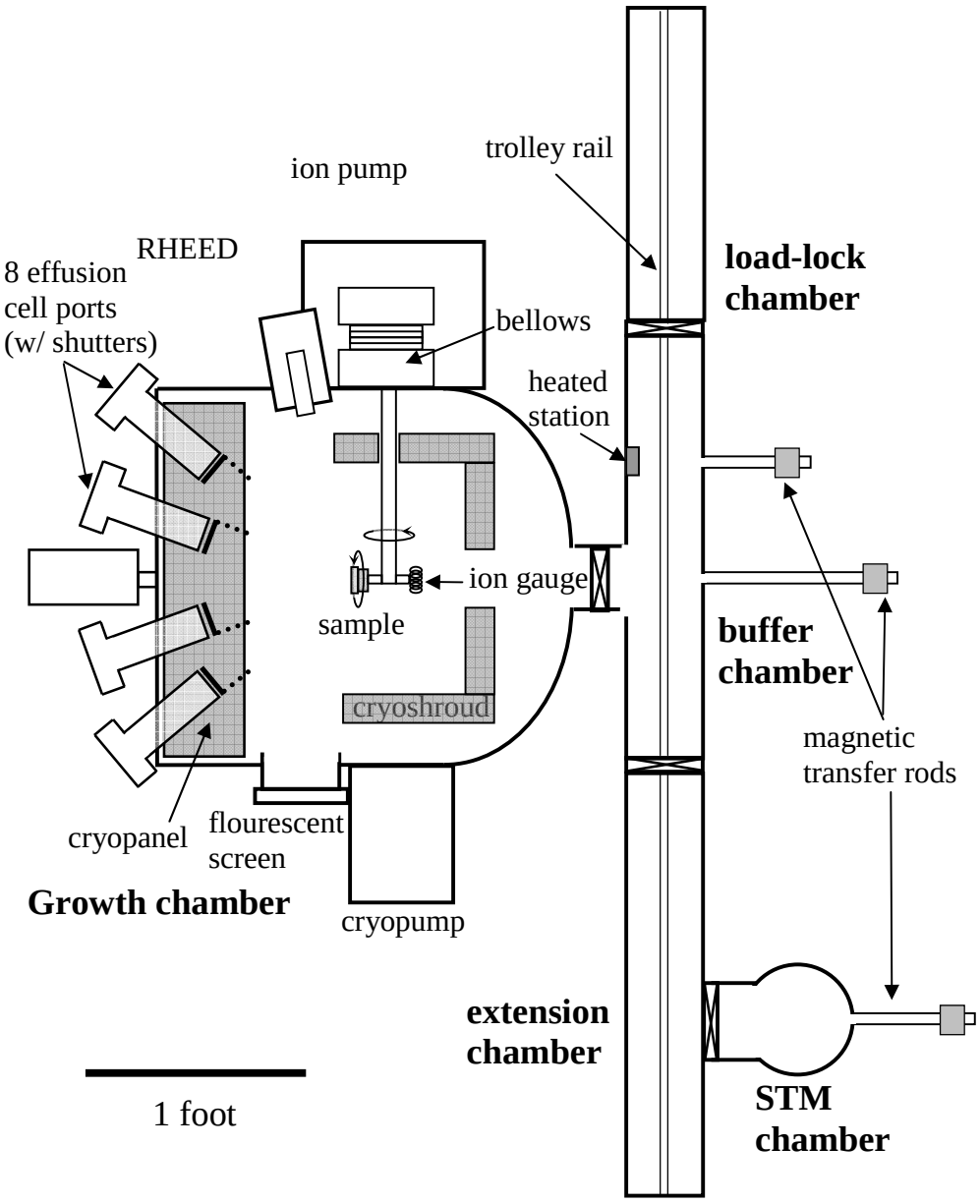

Figure 2.1 Schematic of the Modified Varian Gen II molecular-beam epitaxy system used in these studies. The radio frequency plasma source is located on one of the effusion cell ports, with a gate valve separating it from the main chamber, along with seven solid sources (Ga, In, Al, Be, Si, GaTe, and As cracker). Reprinted with permission from M. Reason., Ph.D. Thesis, University of Michigan. Copyright 2006

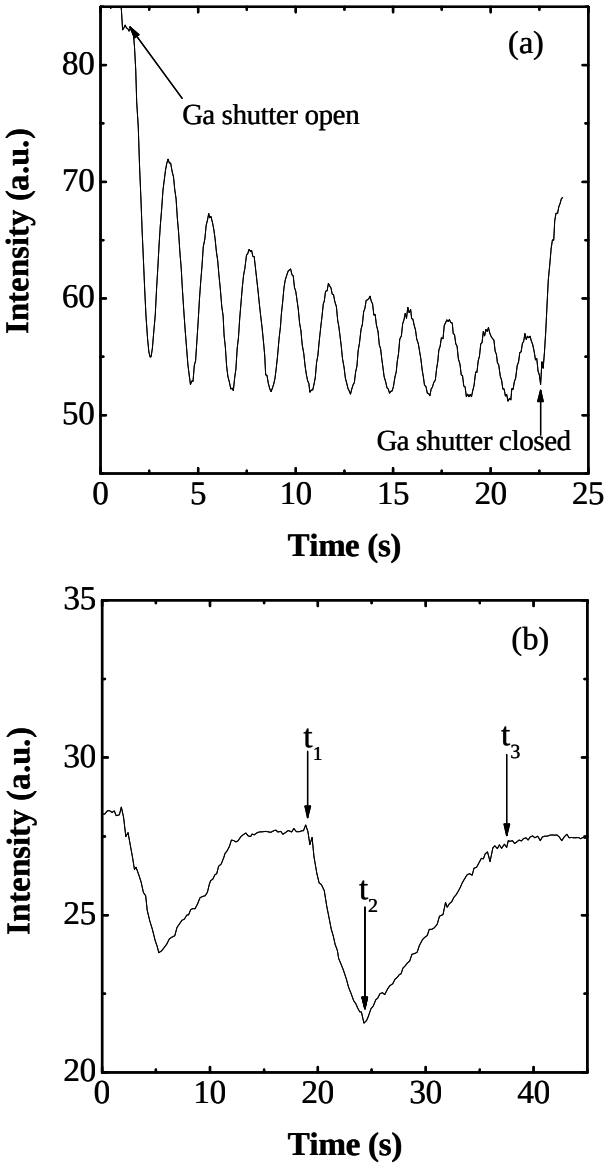

Figure 2.2 RHEED intensity as a function of measurement time for (a) GaAs growth rate calibration and (b) incorporation rate ratio measurement. For the growth rate calibration, the As shutter is always open; the opening and closing of Ga shutter are labeled in (a). For incorporation rate ratio calibration, the As shutter is initially open and the Ga shutter is always open; the As shutter closing, reopening, and the surface reconstruction recovery are labeled t_1, t_2, t_3 in (b) respectively.

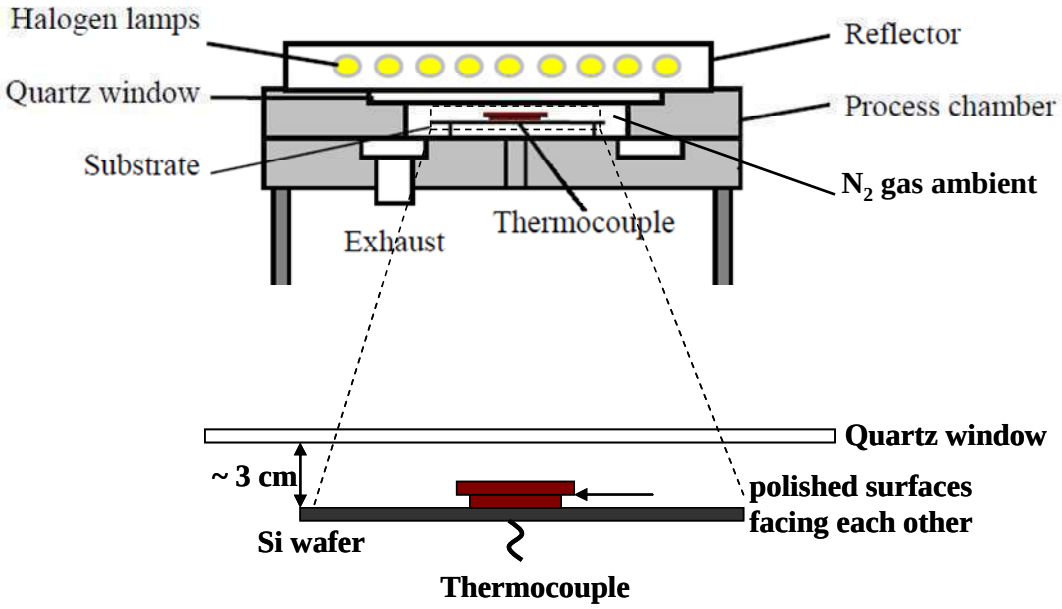

Figure 2.3 Schematic of the rapid thermal annealing setup. The sample is sandwiched between the Si wafer sample holder and a GaAs proximity cap. Illumination from the top is achieved using a halogen lamp.

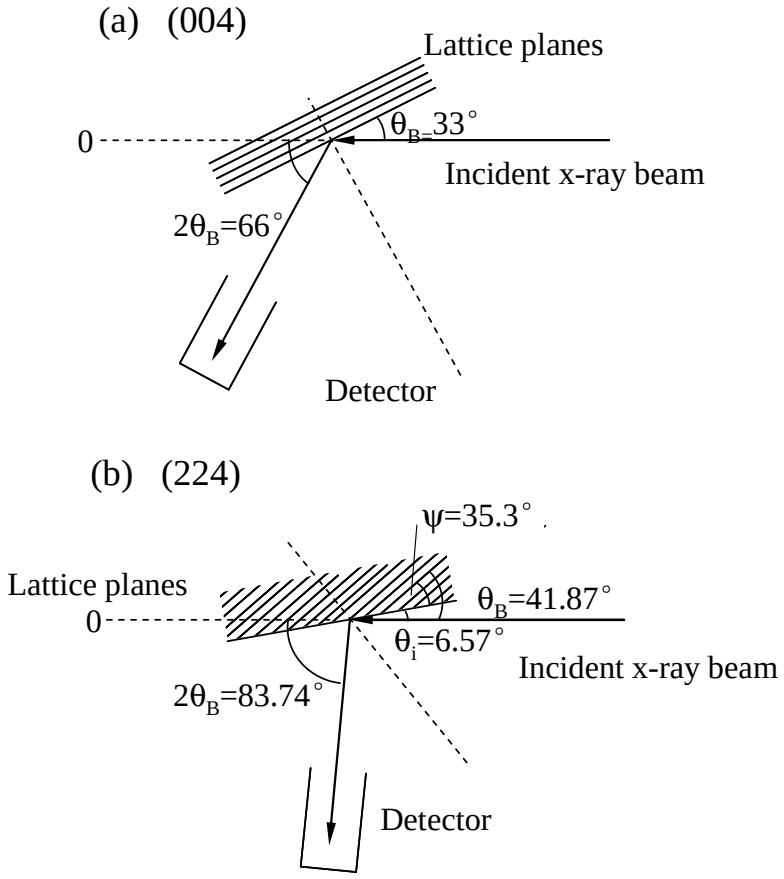

Figure 2.4 Schematics of (a) the symmetric (004) and (b) asymmetric glancing-incidence (224) diffraction geometries of x-ray diffraction measurement.

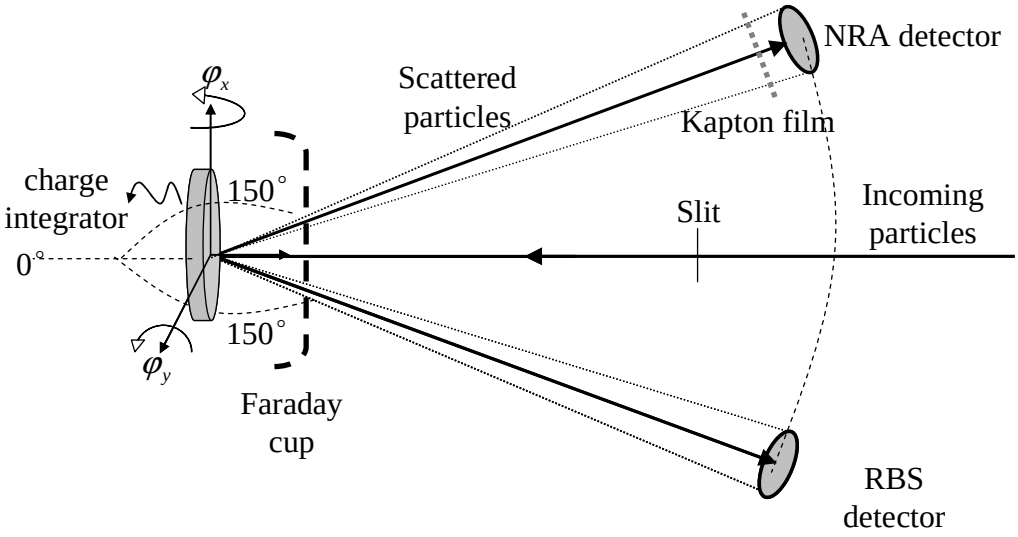

Figure 2.5 A schematic of the Rutherford backscattering spectroscopy (RBS) and nuclear reaction analysis (NRA) experimental setup used at Ion Beam Materials Laboratory at Los Alamos National Laboratory. The incident ion beam is parallel to the normal of the sample surface and the scattered ions were collected by RBS and NRA detectors mounted at a scattering angle of 150° with respect to the incident beam direction. To measure the total number of incident ions, the charge integrator was electrically connected to the sample holder. The sample holder can be rotated around the x- and y-axis, with azimuthal angles φ_x and φ_y, as labeled in the figure.

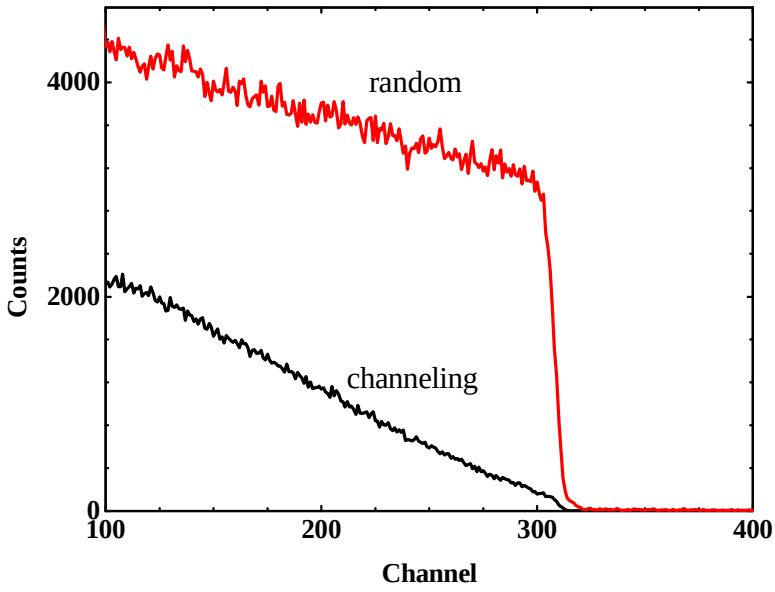

Figure 2.6 RBS spectra for a GaAs sample measured in channeling and non-channeling conditions. The counts of top 4-5 channels near the edge of the spectra (as shown by the shaded region) are chosen to calculate χ_{min}(GaAs), which is then used to calculated interstitial N fraction.

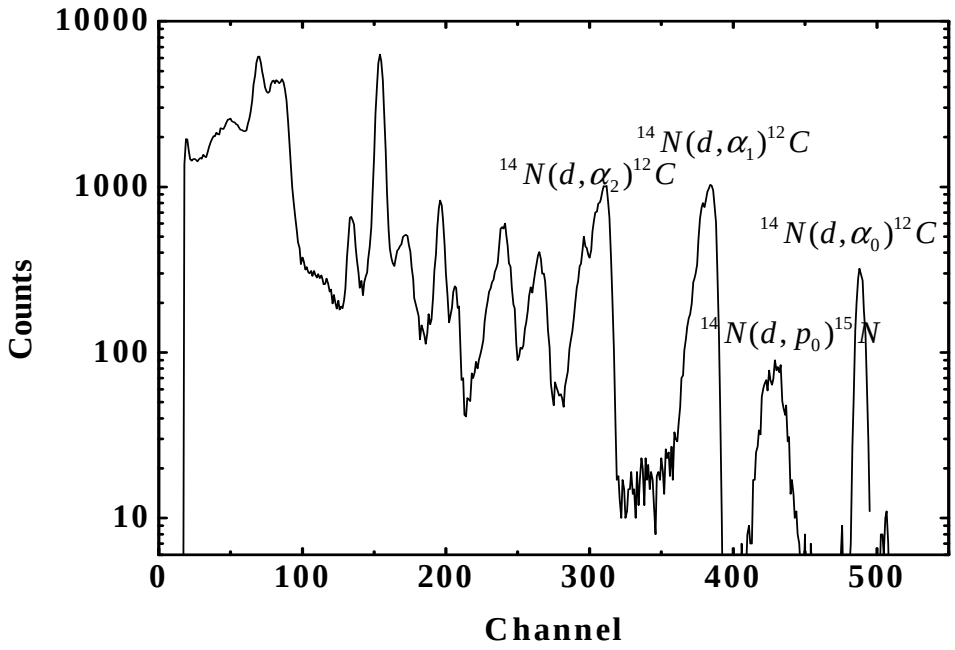

Figure 2.7 NRA yield (counts) vs. channel number for a 32 nm thick TiN film on Si substrate measured in non-channeling conditions. The channel number is linearly dependent on the energy of the emitted particles, and the larger channel numbers represent higher energy. Several high energy N-related nuclear reactions are labeled. The energy of emitted alpha-particles (α_0 and α_1) is higher than the energy from other nuclear reactions; thus, the α_0 and α_1 peaks were used to calculated N composition with minimal interference from the background.

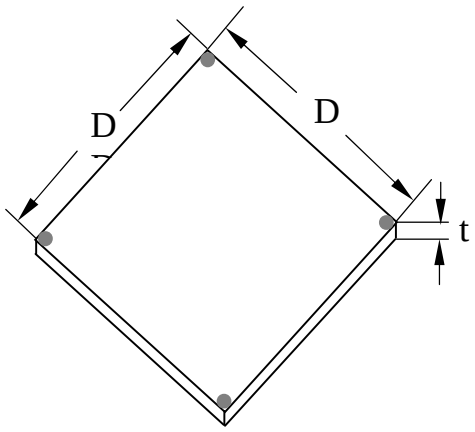

Figure 2.8 Schematic of a typical symmetric Van der Pauw specimen. In our studies, the length of the specimen sides, D, is ~ 5 mm, the specimen thickness, t, is ~ 0.5 mm, and the size of the contacts is typically ~0.05 mm^2. Reprinted with permission from M. Reason., Ph.D. Thesis, University of Michigan. Copyright 2006

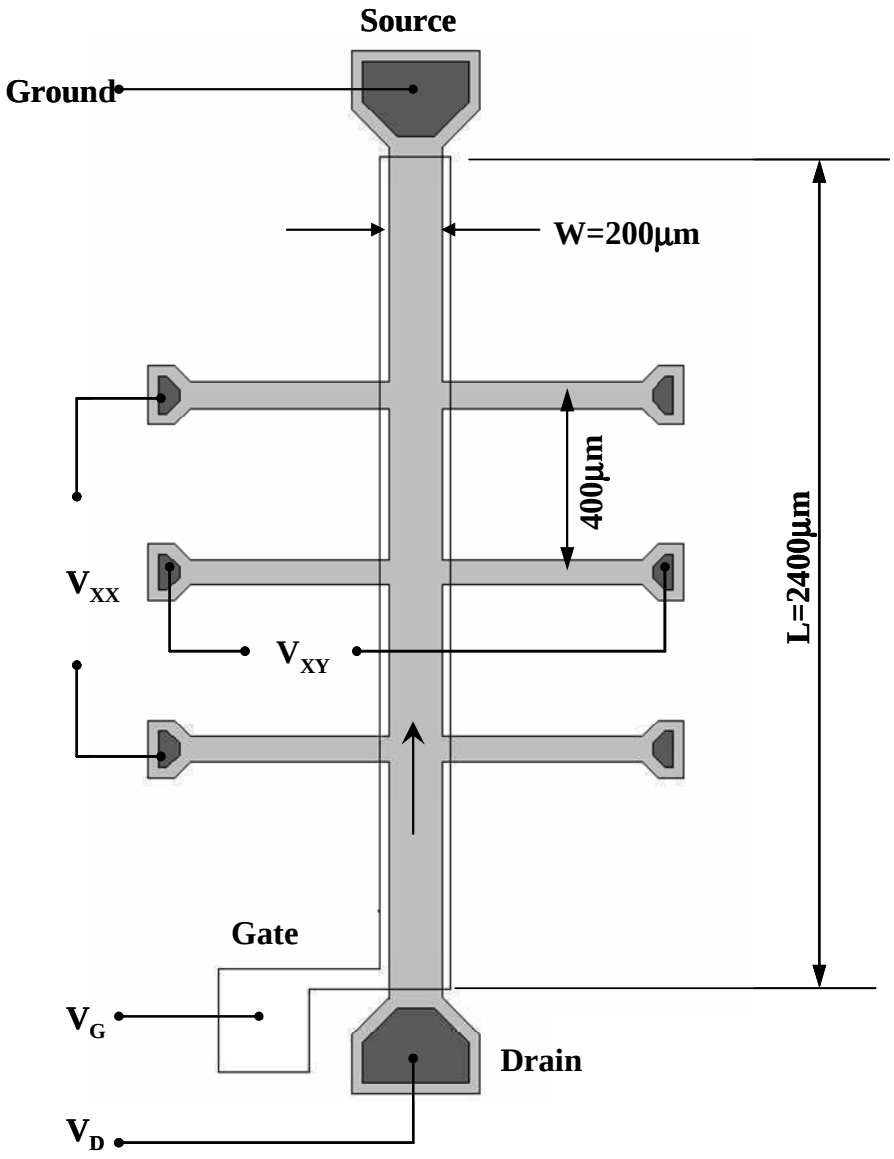

Figure 2.9 Schematic of lithographically-defined 8-arm gated Hall bar used for the electron transport measurements. The area of the gate was defined beyond the edge of the mesa to minimize leakage current along the top periphery of the mesa. This structure is adapted from A.Young's Ph.D. thesis.[23]

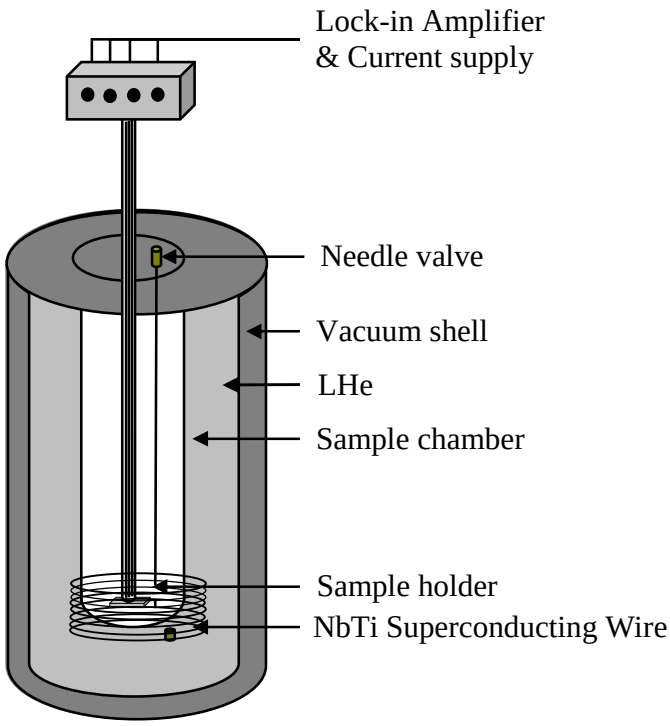

Figure 2.10 Schematic of the cryostat used for variable temperature transport measurements. The cryostat is equipped with a superconducting wire in the vicinity of the sample. A current is passed through the superconductor wire from -72 to +72 A, resulting in a magnetic field ranging from –8 to +8 Tesla.

2.11 References

[1]A. Y. Cho and J. R. Arthur, Progr. Solid State Ch. **10**, 157 (1975).

[2]A. Y. Cho, J. Crys. Growth **202**, 1 (1999).

[3]C. T. Foxon and B. A. Joyce, *Growth and Characterisation of Semiconductors* (Adam Hilger, 1991) pp. 35.

[4]S. G. Spruytte, C. W. Coldren, A. F. Marshall, M. C. Larson and J. S. Harris, MRS Internet J. Nitride Semicond. Res. **5**, art. no.-W8.4 (2000).

[5]M. Reason, Y. Jin, H. A. McKay, N. Mangan, D. Mao, R. S. Goldman, X. Bai and C. Kurdak, J. Appl. Phys. **102**, 103710 (2007).

[6]A. Pulzara-Mora, M. Melendez-Lira, C. Falcony-Guajardo, M. Lopez-Lopez, M. A. Vidal, S. Jimenez-Sandoval and M. A. Aguilar-Frutis, J. Vac. Sci. Technol. B **24**, 1591 (2006).

[7]A. J. Ptak, S. W. Johnston, S. Kurtz, D. J. Friedman and W. K. Metzger, J. Crys. Growth **251**, 392 (2003).

[8]V. V. Preobrazhenskii, D. I. Lubyshev, K. Reginski and J. Muszalski, Thin Solid Films **267**, 51 (1995).

[9]T. Vanbuuren, M. K. Weilmeier, I. Athwal, K. M. Colbow, J. A. Mackenzie, T. Tiedje, P. C. Wong and K. A. R. Mitchell, Appl. Phys. Lett. **59**, 464 (1991).

[10]A. J. Springthorpe, S. J. Ingrey, B. Emmerstorfer, P. Mandeville and W. T. Moore, Appl. Phys. Lett. **50**, 77 (1987).

[11]Manufacturer reported precision of MFC: 0.2% of full scale (10sccm) for readings below 20% of full scale, i.e. 0.02sccm

[12]J. H. Neave, B. A. Joyce and P. J. Dobson, Appl. Phys. a-Mater **34**, 179-184 (1984).

[13]J. M. Van Hove, C. S. Lent, P. R. Pukite and P. I. Cohen, J. Vac. Sci. Technol. B **1**, 741 (1983).

[14]R. Farrow, *Molecular Beam Epitaxy* (Noyes, Park Ridge, NJ, 1995), pp. 84-87.

[15]http://lase.ece.utexas.edu/mbe.php; Download 10:49pm (January 24, 2010)

[16]M. Reason, Ph.D. thesis, Ch. 2. University of Michigan, 2006

[17]X. Weng, Ph.D. thesis, University of Michigan, Ch.2, 2003

[18]J. R. Tesmer and M. Nastasi, *Handbook of Modern Ion Beam Materials Analysis* (Materials research Society, Pittsburgh, 1995) pp. 345.

[19]G. Amsel, J. P. Nadai, Dartemar.E, D. David, E. Girard and J. Moulin, Nucl. Instrum. Meth. **92**, 481 (1971).

[20]S. Pellegrino, L. Beck and P. Trouslard, Nucl. Instrum. Meth. B **219**, 140 (2004).

[21]L. C. Feldman and J. W. Mayer, *Fundamentals of surface and Thin Film Analysis* (North-Holland, New York, 1986)

[22]L. J. Van der Pauw, Philips Res. Repts. **26**, 220 (1958).

[23]A. Young, Ph.D. thesis, Ch. 3. University of California, San Diego, 1997

[24]ASTM Standards, Designation F 76

[25]http://nano.anl.gov/facilities/nanophotonics_cap.html; downloaded 10:48pm (January 24th, 2010)

CHAPTER 3

INFLUENCE OF Si-N COMPLEXES ON THE ELECTRONIC PROPERTIES OF GaAsN ALLOYS

3.1 Overview

This chapter describes investigations of extrinsic N-related point defects, namely, Si-N complexes, on the optical and electronic properties of GaAsN films. First, we summarize the advantages and disadvantages of Si and GaTe as n-type dopants in GaAs MBE growth. Then, we review of earlier investigations of Si-N complex formation in GaAsN. Next, the experimental details for are described.

The bulk of this chapter is devoted to the study the formation of Si-N complexes and their influence on the optical and electronic properties of GaAsN films and modulation-doped heterostructures. The presence of Si-N complexes is first suggested by a decrease in free carrier concentration, *n*, with increasing N composition, which is observed in bulk-like films but not in modulation-doped heterostructures, where N and Si donors are spatially separated in two layers. For GaAsN:Te (GaAsN:Si), *n* increases minimally (substantially) with annealing *T*, suggesting a competition between annealing-induced increases in Si-N complex formation and decreases in N-related free carrier traps. Since the formation of Si-N complexes is enhanced for GaAsN:Si growth with the (2 x 4) reconstruction, which has limited group V sites available for As-N exchange, the

interstitial Si-N pair, $(Si\text{-}N)_{As}$, is identified as the dominant Si-N complex. Finally, the heterostructures were also used to study carrier scattering mechanisms in GaAsN alloys. With minimal Si-N defect complexes, the dominant source of carrier scattering was identified to be neutral scatterers, likely N interstitial-related point defects.

3.2 Background

3.2.1 Si-doping of GaAs

Si is commonly used as an n-type dopant for GaAs-based materials and devices grown by molecular beam epitaxy (MBE) and metalorganic chemical vapor deposition (MOCVD). As a hydrogenic shallow donor, the ionization energy of Si in GaAs is 4-6 meV. Si has the following advantages when used as a dopant in MBE growth: it has a low vapor pressure, low toxicity, low diffusivity, and negligible surface segregation in the film growth direction. In addition, the doping concentration can be fairly well controlled at low to middle doping level ($<5x10^{18}$ cm^{-3}), by adjusting the effusion cell temperature. However, the doping efficiency of Si decreases as the doping concentration increases. As the Si doping level increases above $\sim 7x10^{18} cm^{-3}$, the number of free carriers first saturates and then begins to drop with further higher doping.[1] This is likely due to the amphotericity of Si in GaAs. Since Si is a group IV element, it can act as a donor or an acceptor, depending on its occupation of Ga or As lattice sites, i.e. Si_{Ga} or Si_{As}. At high doping levels, the amphotericity of Si leads to significant autocompensation, which lowers the doping efficiency and induces additional electron scattering.[2-4] Indeed, it has been suggested that for the growth of stoichiometric GaAs on (001) GaAs substrates, Si predominantly occupies group III sites, leading to electron donor behavior.[5, 6] For other growth conditions, such as liquid phase epitaxy from a gallium-rich solution at relatively low temperatures, or growth on (n11) substrate using MBE, where $n \leq 3$, p-type GaAs:Si has been reported.[7-9]

The maximum free carrier concentration achieved for Si-doped GaAs, $1.8 x10^{19}$ cm^{-3}, was obtained at a relatively low growth temperature < 420 ^{o}C.[10] This has been

explained in terms of reduced autocompensation at lower growth temperatures (i.e. ~400 ºC vs. ~600 ºC). The resulting higher surface vacancy concentration ratio $[V_{Ga}]/[V_{As}]$ would facilitate incorporation of substitutional dopant atoms.[11] However, others have suggested that autocompensation would only account for a minor ("up to half") effect of the electrical inactivity in GaAs.[12,13,14] Instead, the reduced Si activity has been attributed to the presence of Si_{Ga}-V_{Ga} pairs, Si_{Ga}-Si_{As} dimers, and/or Si_n (n>2) clusters.[13,15,1]

3.2.2 Alternative group VI sources for n-doping in GaAs

Group VI elements (Chalcogens), such as S, Se, and Te are expected to predominantly occupy group V sites, acting as donors (n-type dopants) in III-V compounds. Indeed, Sb-containing III/V semiconductors, such as GaSb and GaAsSb, are typically doped with Te.[16] For GaAs and InP, the n-type doping with Te has several other advantages, including a high incorporation efficiency, which leads to high achievable doping levels, and a low diffusion coefficient.[17-19] In addition, the donor activation energy is lower for AlGaAs:Te than for AlGaAs:Si.[20] Furthermore, for MOCVD growth, n-type doping is commonly achieved using group VI-based sources, such as H_2Se[21] and dielthyltellurium (DETe).[18]

However, during MBE growth, it is not straightforward to use Te as a dopant. First, elemental Te has a very high vapor pressure (i.e. low temperature for sublimation), which leads to poor source temperature stability and makes it more likely to stay in the chamber after growth. Thus, elemental Te source is not suitable for UHV MBE growth.[22] In addition, during GaAs growth, Te acts as a surfactant, which modifies the kinetic processes occurring at the growth surface.[23, 24] Furthermore, as shown by Newstead *et al.*,

using a combination of MBE growth and SIMS profiling, Te exhibits surface segregation in GaAs layers grown at 600 ºC and above,[25] and Te desorption is also apparent at 600 °C and 630 °C.

Alternative group VI sources for n-type doping of during MBE growth of III-Vs include III-VI chalcogenides, such as GaTe, PbTe and PbSe. For GaTe, the cell temperature required to achieve 1 x 10^{18}cm^{-3} Te doping in GaAs is ~ 500ºC, which is high enough to achieve precise temperature control.[26] n-type doping with chalcogenides has been achieved in various III-V semiconductors, such as GaTe doping in AlGaSb,[22] and PbTe doping in AlSb and GaSb.[27] More recently, Bennett *et al*. performed a systematic study of using GaTe as an n-type dopant in several antimonide and arsenide III–V compounds. For a fixed GaTe flux, similar free carrier concentrations were obtained in various arsenide and antimonide compound host materials. Specifically, for source temperatures ranging from 350 ºC to 550 ºC, free carrier concentrations from 3x10^{16} cm^{-3} to 1x10^{19} cm^{-3} were achieved. Following the use of GaTe, insignificant cell cross-talk or memory problems were found in the MBE.[28]

3.2.3 N-Si pair formation

It is interesting to note that the highest reported mobility for InGaAsN is μ ~ 2000 cm^{2}V^{-1}s^{-1} is achieved by MOCVD, using DETe as the Te source.[29] This is an order of magnitude higher than the typical μ for (In)GaAsN:Si alloys.[30] Thus, it has been suggested that the degraded electronic properties of (In)GaAsN:Si might be related to the interaction between N and Si donors, which form a Si-N complex, leading to a reduced electrical activity of Si in InGaAsN.[31-33]

The formation of N-Si pairs has also been suggested by observations of unusual annealing behavior in GaAsN:Si.[31] Rapid thermal annealing (RTA) is frequently used to improve the electron mobility and photoluminescence efficiency of GaAsN alloys.[34-38] However, in highly Si doped (Si ~ $1x10^{19}cm^{-3}$) GaAsN films, Yu *et al*. reported that RTA substantially increases the resistivity of GaAsN films, with a negligible effect on those doped with Se.[31] A slight increase in the effective bandgap following annealing also was reported for GaAsN:Si.[31]

Yu *et al.* attributed the above phenomena to the formation of substitutional Si-N pairs, Si_{Ga}-N_{As}, as shown in Fig. 3.1 (a). The presence of Si_{Ga}-N_{As} was also suggested by Li *et al.*'s calculations, which showed that Si_{Ga}-N_{As} binding in GaAsN is energetically favored, and that Si_{Ga}-N_{As} formation pushes the shallow Si_{Ga} donor levels deep into the bandgap.[32] However, according to the calculations of Janotti *et al.*, the binding energy (0.26 eV) for the substitutional Si-N pair, Si_{Ga}-N_{As}, is too small to explain the formation of a high concentration of Si_{Ga}-N_{As} pairs at temperatures above 800 ºC. In addition, the Si_{Ga}-N_{As} model does not explain the appearance of a deep level at 0.8 eV above the valence band (VB) maximum observed in photoluminescence experiments.[33, 39] On the other hand, Janotti *et al*. proposed a more energetically favorable Si-N interstitial pair, $(Si\text{-}N)_{As}$, which acts as a deep acceptor in n-type GaAsN.[33] The schematic of the $(Si\text{-}N)_{As}$ pair is shown in Fig. 3.1 (b). Prior to this dissertation research, no experimental evidence has been reported to support either form of the Si-N complexes, and the influence of Si-N complexes on the GaAsN electronic properties was unknown.

3.2.4 Modulation-doping of AlGaAs/GaAs(N)

To investigate the influence of N-dopant spatial separation on the electronic properties of GaAsN, modulation-doped heterostructures were employed. Modulation-doping is commonly utilized to enhance the mobility of semiconductor alloys by reducing the ionized impurity scattering via spatial separation of the free carriers and the ionized impurities.[40-42] In particular, a modulation-doped two-dimensional electron gas (2DEG) heterostructure consists of a junction between wide and narrow bandgap semiconductors, such as AlGaAs/GaAs. The wide bandgap material is doped in the vicinity of the junction while the narrow bandgap material is undoped. For n-type doping, since the conduction band (CB) of the wide gap material is higher in energy than that of the narrow gap material, electrons are transferred across the interface to the lower band, forming a two dimensional electron system at the narrow gap side of the interface.[43 44, 45]

AlGaAs/GaAs(N) 2DEGs provide a unique opportunity to study the carrier scattering/trapping in GaAsN without Si-N defect complexes. In addition, the 2DEGs enable studies of the carrier scattering and/or trapping mechanism associated with the N defects in GaAsN with minimal ionized impurity scattering from the ionized Si donors.[43, 44, 46] Furthermore, the free carrier density in the 2DEG channel layers can be easily adjusted by applying front gate voltage, or by illumination (utilizing the persistent photoconductivity effect in AlGaAs).[43 44] In semiconductors, the dependence of the relaxation time, τ, and the electron mobility, μ, on Fermi energy varies with scattering mechanism. For example, in 3D, for ionized impurity scattering, $\tau \sim E_f^{3/2}$, for piezoelectric scattering $\tau \sim E_f^{1/2}$, and for neutral impurity scattering, τ is independent of E_f. Therefore, to further investigate the N-related scattering mechanisms, it is ideal to study

μ as a function of Fermi energy. However, in bulk films, the Fermi level can only be varied by growing films with different doping concentration. This is not only tedious but also induces additional extrinsic impurities, which would complicate the analysis. In this case, the modulation-doped heterostructure is useful as it enables us to manipulate the Fermi level in the 2DEG layer by either gating or illumination, without having to grow a series of samples or introducing additional scattering sources.

3.3 Experimental Details:

The $GaAs_{1-x}N_x$ alloy films were grown on semi-insulating (001) GaAs substrates by molecular-beam epitaxy (MBE), using Ga, As_2, Si or GaTe (for n-type doping) and an N_2 rf plasma source. For bulk-like films, after an initial 250 nm thick GaAs buffer layer was grown at 580 °C, 500 nm GaAs(N) films were grown with either Si or GaTe doping.[26, 28] The sample cross-section of the bulk-like films is shown in Fig. 3.2. First, for the purpose of doping calibration, a series of GaAs:Te and GaAs:Si films were grown with different Si and Te cell settings, substrate temperatures, and GaAs growth rates. For the growth of GaAsN films, the Si and GaTe cell *T*s were chosen to target equivalent *n* in GaAs:Te and GaAs:Si control films. Most GaAsN layers were grown at relatively low *T* (~400°C), to avoid growth in the so-called "forbidden window", a specific *T* range where multilayer growth has been reported for GaAsN, as introduced in Section 3.6 of M. Reason's PhD thesis.[47] These films will be referred to as "low-*T* GaAsN:Si". Several GaAsN:Si layers were also grown at elevated substrate *T*, 580 °C, which will be referred to as "high-*T* GaAsN:Si".

For the modulation-doped heterostructures, the sample cross-section is shown in Fig. 3.3. First, a 50 nm thick GaAs(N) channel was grown at 400 °C. Next, a 5 minute pause was used to ramp the substrate temperature to 580°C, and layers of 1 nm GaAs, 20 nm undoped $Al_{0.3}Ga_{0.7}As$, 60 nm Si-doped $Al_{0.3}Ga_{0.7}As$, and 10 nm GaAs were then grown in succession. All layers were grown with the V/III beam equivalent pressure (BEP) ratios adjusted to produce a ratio of As/Ga incorporation rates of ~1.5,[48] which corresponds to a V/III BEP ratio of ~15 (~10) for growth temperatures of 580 °C (400 °C). 2DEG heterostructures containing GaAs or GaAsN as the channel layer will be referred to as a "control 2DEG" or "nitride 2DEG", respectively.

For select samples, rapid thermal annealing (RTA) was performed for 60s in the temperature range 650 to 800 °C. (004) and (224) x-ray rocking curves (XRC) were compared before and after annealing. For example, (004) and (224) XRCs collected from a $GaAs_{0.983}N_{0.017}$ film before and after annealing are shown in Fig. 3.4. In all cases, the substrate reflections are set to 0, and the GaAsN epilayer peaks are marked with a dashed line. For the (004) reflections, the substrate-epilayer peak separation is ~1000 arcsec before and after RTA, suggesting negligible RTA-induced changes in the (004) lattice plane spacing. Similarly, for the (224) reflections, the substrate-epilayer peak separation is ~1500 arcsec before and after RTA. Since both the (004) and (224) lattice plane spacings of the film remain unchanged with RTA, it is likely that the average N composition remains constant following RTA. Indeed, analysis of a series of (004) and (224) XRCs indicates that the average N composition in the GaAsN films remains unchanged after RTA up to 800 °C. For the dilute nitride 2DEG samples, the N compositions in the channel layers were determined using NRA of similarly-grown 1 μm

thick GaAsN bulk-like films.

The 2DEG samples were all fabricated into Hall bar geometry, and transport measurements were performed at 1.5 K, 4.2 K, and room temperature. Parallel resistivity, ρ_{xx}, and transverse resistivity, ρ_{xy}, were measured as a function of magnetic field, from 0 to 7 T. To modulate the free carrier density, the gate voltage was swept from -100 mV to 70 mV, and magnetoresistance measurements were collected in increments of 10 mV. To increase the carrier density, samples were illuminated with an LED during the measurement. These type of measurements will be termed "illumination-assisted" measurements. After illumination for 10-15 minutes, the LED was switched off and the magnetoresistance data was immediately collected in the dark. Any variation in time-lag between switching off the LED and performing the measurement is not expected to be significant, due to the typically long relaxation time (hours or even days) of carriers activated by the persistent photoconductivity effect in AlGaAs/GaAs modulation-doped heterostructures.[49-51]

3.4 Influence of N-dopant spatial separation

Here, we compare the electronic properties of $GaAs_{1-x}N_x$ alloys with various Si-N spatial separations. Figure 3.5 (a) presents the free carrier fraction, i.e., the ratio of n_{GaAsN} for Si-doped bulk-like GaAsN films to that of n_{GaAs} with equivalent GaTe targeted doping concentration. The free carrier fraction is significantly lower than unity, and decreases with increasing x. This trend is consistent with the results of Ishikawa *et al*., also plotted in Fig. 3.5 (a).[52] The trend of decreasing free carrier fraction with increasing x suggests the presence of N-related charge trapping centers in the GaAsN:Si films.

Shown in Fig. 3.6 is the CB diagram of the AlGaAs/$GaAs_{1-x}N_x$ modulation-doped heterostructures calculated with 1D Poisson/Schrödinger simulation software.[53-55] Magnetoresistance measurements of longitudinal resistivity, ρ_{xx}, and transverse resistivity, ρ_{xy}, as a function of magnetic field, for (a) control 2DEGs, (b) a dilute nitride (x=0.0008) 2DEG prior to illumination, and (c) a dilute nitride (x=0.0008) 2DEG following illumination are presented in Fig. 3.7. For both types of 2DEGs, quantum Hall (QH) plateaus are observed at $\rho_{xy}=h/ie^2$, where h is Planck's constant, e is the charge of an electron, and i is an integer.[56] In addition, both 2DEGs exhibit oscillations of ρ_{xx} as a function of inverse magnetic field, typically referred to as Shubnikov-de Haas (SdH) oscillations.[51] The presence of the quantum Hall plateaus and SdH oscillations confirms the two-dimensional nature of the electron gases,[46] and the single oscillation period in ρ_{xx} is indicative of the occupation of one subband of the 2DEG. Charge-carrier confinement in the 2DEG is confirmed through a comparison of the total electron concentration, n_s determined from illumination-assisted SdH measurements, and the apparent electron concentration, n, determined from illumination-assisted Hall measurements. As shown in Table 3.1, n(n_s) for the control and the dilute nitride 2DEGs were varied by increasing the duration of illumination at a fixed intensity.

Fig 3.5 (b) shows the sheet free carrier concentration, n_s, vs. measurement T for several control and dilute nitride 2DEGs (x=0.0008) with equivalent targeted Si doping concentrations in the AlGaAs doping supply layer. In contrast to the bulk-like films, n_s are similar for the control and dilute nitride 2DEGs at all three measurement Ts. In the bulk films, Si and N reside in the same layer; in 2DEGs Si donors are spatially separated from the GaAsN channel layer, reducing the likelihood for formation of N-Si nearest

neighbors. Since the electron trapping is observed in bulk-like films but not in 2DEGs, the electron trapping is likely related to the presence of Si dopants in the vicinity of N atoms, presumably due to the formation of Si-N complexes.[30]

Table 3.1: Comparison of the total electron concentration, n_s, determined from illumination-assisted Shubnikov-de Haas (SdH) oscillations, and the apparent electron concentration, n, determined from illumination-assisted gated Hall measurements, for the control and dilute nitride samples, $GaAs_{1-x}N_x$ with x=0.0008. For both the control and the dilute nitride 2DEGs, fixed intensity illumination, for a variety of durations, was used to simultaneous increase n and n_s, as described in Section 3.3. Values are in agreement within 3% and 7% for the control and nitride samples, respectively.

	Control - n_s ($x10^{11}cm^{-2}$)	Control – n ($x10^{11}cm^{-2}$)	Dilute Nitride - n_s ($x10^{11}cm^{-2}$)	Dilute Nitride – n ($x10^{11}cm^{-2}$)
↓ Increasing duration of illumination at a fixed intensity	1.27	1.25	1.15	1.14
	1.31	1.30	1.29	1.24
	1.4	1.3	1.4	1.3
	1.50	1.47	1.59	1.52
	1.62	1.58	1.75	1.67
	-	1.84	1.90	1.81
	-	2.45	2.09	1.97
	2.70	2.65	2.34	2.20
	3.15	3.10	2.69	2.52
			2.95	2.76

3.5 Effects of n-type dopant species

The charge trapping effects of Si-N complexes are further investigated through a comparison of the influence of Si and Te-doping on resistivity, Hall, and PL measurements of GaAsN bulk-like films. Figure 3.8 shows n and μ as a function of annealing-T for GaAsN:Si and GaAsN:Te bulk films, in comparison with GaAs:Si and GaAs:Te control samples. As-grown GaAsN films exhibit significantly lower n and μ than the GaAs control samples, and GaAsN:Te films have slightly higher n than GaAsN:Si films. After annealing, minimal changes in n and μ are observed for the GaAs

control samples. In GaAsN:Te, a substantial increase in both n and μ with increasing annealing T is observed. However, in GaAsN:Si films, we observed a similar increase of μ as in the GaAsN:Te films, with minimal increase of n.

The charge trapping effect of Si-N complexes in GaAsN:Si is also evident in the optical properties. Figure 3.9 presents PL spectra for as-grown and annealed GaAsN:Te and GaAsN:Si films with equivalent N compositions. For the as-grown films, the near-bandedge (NBE) PL emission intensity of GaAsN:Te is 1.5 times higher than that of the GaAsN:Si film. For both films, the FWHM are similar and are reduced ~15 % following annealing. Thus, the improvement of NBE PL efficiency is more significant for GaAsN:Te than for GaAsN:Si.

The insignificant annealing-induced increase in n and PL emission intensity of GaAsN:Si provides additional evidence for the charge trapping effect of Si-N complexes. For GaAsN:Te, annealing leads to higher n and μ, presumably due to the reduction in N-related free carrier traps, such as N interstitials. In case of GaAsN:Si, the annealing-induced reduction in electron trapping is presumably balanced by the enhanced formation of Si-N pairs. Calculations suggest that Si-N complex formation is energetically favorable in the GaAsN:Si system.[33, 57] In addition, the diffusion length of Si in GaAs at 750°C for 60s is estimated to be 1.5nm,[58] comparable to the average distance between N atoms in $GaAs_{1-x}N_x$ with x=0.01-0.02. Indeed, for a random N distribution in GaAsN, N-N separations of 1.3 to 1.6 nm are calculated, by assuming N atoms distribute uniformly in GaAs lattice. Thus, it is likely that annealing induces Si diffusion to N atoms, and the consequent formation of Si-N complexes. Similar effects have not been predicted or reported for group VI dopants in GaAsN.

3.6 Effects of surface reconstruction

Table 3.2 compares n and μ for low and high-T $GaAs_{1-x}N_x$:Si films with x=0.005-0.02. The low-T GaAsN:Si films are n-type with n ~2 to $5x10^{17}$ cm^{-3} and μ ~ 200 cm^2/Vs, consistent with literature reports.[52] However, for high-T GaAsN films, degenerately Si-doped films are observed to be slightly p-type, with hole concentrations ~ $1x10^{15}$ cm^{-3}. Although Si is amphoteric in GaAs, Si is expected to predominantly occupy Ga sites, acting as a donor for GaAs(N) films grown at 580°C.[59] Indeed, for the high-T GaAs:Si films, n-type conductivity is observed, as shown in Table 3.2. For high-T GaAsN:Si, most Si are presumably electrically inactive due to the formation of Si-N complexes in either Si_{Ga}-N_{As} or $(Si\text{-}N)_{As}$ form, while a negligible fraction of Si atoms replacing As sites act as acceptors, leading to p-type conductivity. After annealing, for both low-T and high-T GaAsN:Si films, n and μ are improved, presumably due to the annealing-induced reduction in interstitial N fraction, which will be described in Section 4.5.

Table 3.2: Free carrier concentrations, n, and mobility, μ, for as-grown and annealed low-T GaAsN:Si and high-T GaAsN:Si films with various N compositions, N%.

		as-grown			780 ºC RTA		
N composition (%)		n/p(cm-3)	ρ(Ωcm)	type	n/p(cm-3)	ρ(Ωcm)	type
GaAsN:Si (400ºC)	1.0	$3.1x10^{17}$	230	n	$3.3x10^{17}$	242	n
	1.3	$2.7x10^{17}$	192	n	$4.0x10^{17}$	286	n
	1.9	$1.5x10^{17}$	161	n	$3.7x10^{17}$	329	n
HT-GaAs(N):Si (580 ºC)	0	$1.3x10^{18}$	2000	n	$1.3x10^{18}$	2000	n
	0.6	$3x10^{15}$	130	p	$5.6x10^{16}$	94	p
	1.0	$6.5x10^{15}$	246	p	$1.7x10^{16}$	141	p
	1.3	highly resistive			$4.2x10^{16}$	78	p

The enhanced formation of Si-N complexes for the high-T growth provides important information regarding the atomic structure of Si-N defect complexes, which was under debate in the literature.[33, 57] As mentioned in Section 3.2, two models has been proposed for the geometry of the Si-N complexes, Si_{Ga}-N_{As}, and $(Si\text{-}N)_{As}$. During the growth of the GaAsN at 400 and 580 °C, the surface reconstructions are (2 x 1) and (2 x 4), respectively, as shown in Fig. 3.10.[60, 61] It has been suggested that the (2 x 4) GaAs surface leads to a greater fraction of N incorporated interstitially, since (2 x 4) GaAs surfaces have fewer group V sites per unit area than (2 x 1) GaAs surfaces, as shown in Fig. 3.10.[60-62] Similarly, $(N\text{-}Si)_{As}$ are more likely to form on the (2 x 4) GaAs surface. On the other hand, for (2 x 1) GaAs, due to the high areal density of group V sites, N and Si atoms may more effectively incorporate substitutionally and form Si_{Ga}-N_{As} bonds. Thus, the enhanced formation of Si-N pairs for HT-GaAsN:Si with (2 x 4) reconstruction suggests that $(Si\text{-}N)_{As}$ is the most likely physical model for Si-N complexes in GaAsN:Si.

3.7 Carrier Scattering in GaAsN without Si-N complexes

The AlGaAs/GaAs(N) modulation-doped heterostructure also enables us to study N-related scattering mechanisms in GaAsN, presumably independent of Si-N defect complexes. Figure 3.11 presents μ, determined from the sheet carrier density, n_s, and sheet resistivity, $\rho_{xx,}$ as a function of n_s, for the control and dilute nitride 2DEGs. n_s is varied by illumination with the LED or by applying a gate voltage, as described in Section 3.3 μ of our dilute nitride 2DEGs are higher than those reported Mouillet *et al.*[40] (0.05% N) and Fowler *et al.*,[41] (0.1% N), likely due to the reduction of residual N incorporation in the non-channel layer with the improved "gate-valve" control of the N

plasma source, as discussed in Reason's 2007 paper.[30] For comparison, tight-binding calculations by Fahy for a 10 nm 0.1% N GaAsN quantum well[63] are also included. For the control 2DEGs, the power law dependence of μ on carrier density is consistent with literature reports.[23] In addition, μ for the control 2DEG increases continuously with increasing n_s, while μ for the dilute nitride 2DEG saturates for $n_s > 2\text{x}10^{11}$ cm^{-2}.

It has been reported that the dominant low temperature scattering mechanism in AlGaAs/GaAs 2DEGs is the Coulomb interaction between the free carriers and the ionized impurities, termed "long-range ionized impurity scattering."[43, 46] As the carrier density in the channel is increased, there is increased screening of the Coulomb interaction with the ionized Si dopants, leading to an increase in μ.[64] More specifically, μ is proportional to the momentum relaxation time, τ. For ionized impurity scattering, τ varies as $E_f^{1.5}$,[65] where E_f is the Fermi energy; in two-dimensional systems, E_f increases linearly with n_s.[43, 46] Thus, for control 2DEGs, μ is predicted to depend on n_s according to $\mu \sim n_s^{\gamma}$, where γ=1.5. Experimentally, for AlGaAs/GaAs 2DEGs, γ usually ranges from 1 to 1.7, depending on the thickness of the spacer layer.[65] On the other hand, in channel layers for which the dominant scatterers are neutral, increasing the carrier density does not screen the scattering potential. Thus, when neutral scattering sources are dominant, μ typically has a weak dependence on n_s, i.e., $\gamma \sim 0$.[64]

As shown in Fig. 3.11, the control 2DEG electron mobility increases continuously with carrier density, while the electron mobility of the dilute nitride 2DEG increases with n_s to a constant value for $n_s \sim 1.5\text{x}10^{11}$ cm^{-2}. To investigate the N-related carrier scattering mechanisms, a linear least-squares fit to the μ vs. n_s data for $n_s > 2\text{x}10^{11}$ cm^{-2} is applied, and the mobility dependence on the carrier density is expressed as $\mu \sim n_s^{\gamma}$. For the control

2DEGs, γ=0.9, indicating that long-range ionized impurity scattering is the dominant scattering mechanism. On the other hand, for the dilute nitride 2DEGs, a weak dependence of μ on n_s is apparent, with γ=0.1, and μ is saturated for $n_s > 1.5\text{x}10^{11}$ cm^{-2}. Thus, increasing the carrier density in the GaAsN channel does not reduce scattering, and we conclude that the N-related defects are apparently behaving as neutral scattering sources, rather than long-range ionized impurity scattering sources.

This trend of weak dependence of electron mobility on carrier density in the dilute nitride 2DEG is consistent with the tight-binding model calculations of Fahy *et al.*, also plotted in Fig. 3.11, which include the interaction of the CB with nitrogen-related cluster states.[63] At low carrier densities ($n_s < 1\text{x}10^{11}$ cm^{-2}), the deviation of the mobility from a power law dependence is likely due to metal-insulator transition (MIT) [44, 66] which was not taken into account in the calculations of Fahy *et al.*[63] The MIT effect will be discussed in more detail in section 4.2.2

3.8 Conclusions

In summary, we have investigated the influence of Si-N complexes on the electronic properties of GaAsN alloys. The presence of Si-N complexes is suggested by a N-composition dependent decrease in *n*, which is observed in bulk-like films but not modulation-doped heterostructures. In addition, for GaAsN:Te (GaAsN:Si), *n* increases minimally (substantially) with annealing *T*, suggesting a competition between annealing-induced increases in Si-N complex formation and decreases in the N interstitial concentration. Since the formation of Si-N complexes is enhanced for GaAsN:Si growth with the (2 x 4) reconstruction, which has limited group V sites available for As-N

exchange, the interstitial Si-N pair, $(Si\text{-}N)_{As}$, is identified as the dominant Si-N complex. Finally, modulation-doped AlGaAs/GaAsN heterostructures with the N and Si donor spatially separated were used to study the scattering mechanism in GaAsN with the absence of Si-N defect complexes. The dominant source of scattering is identified to be neutral scatterers, likely N interstitial related point defects.

3.9 Figures

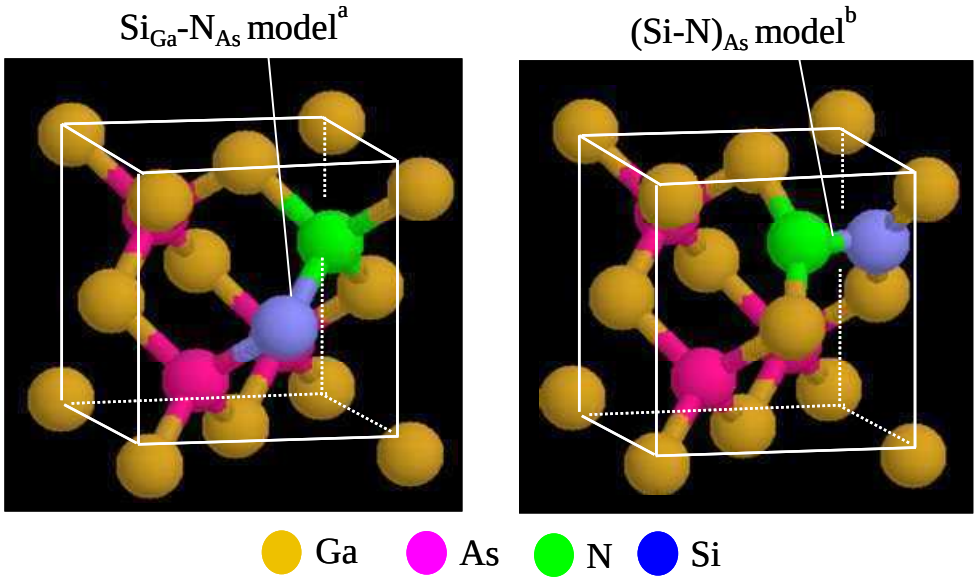

Figure 3.1 Ball and stick schematic for the GaAs unit cell containing (a) substitutional Si_{Ga}-N_{As} defect complex, Ref.[57] (b) interstitial $(Si\text{-}N)_{As}$ defect complex, Ref.[33]

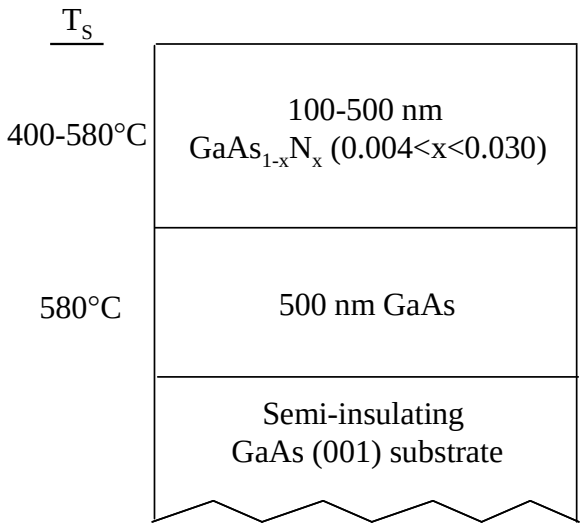

Figure 3.2 Cross-section of $GaAs_{1-x}N_x$ films which consisted of an undoped 250 nm thick GaAs buffer layer and a 500 nm thick $GaAs_{1-x}N_x$ layer grown by solid source molecular beam epitaxy.

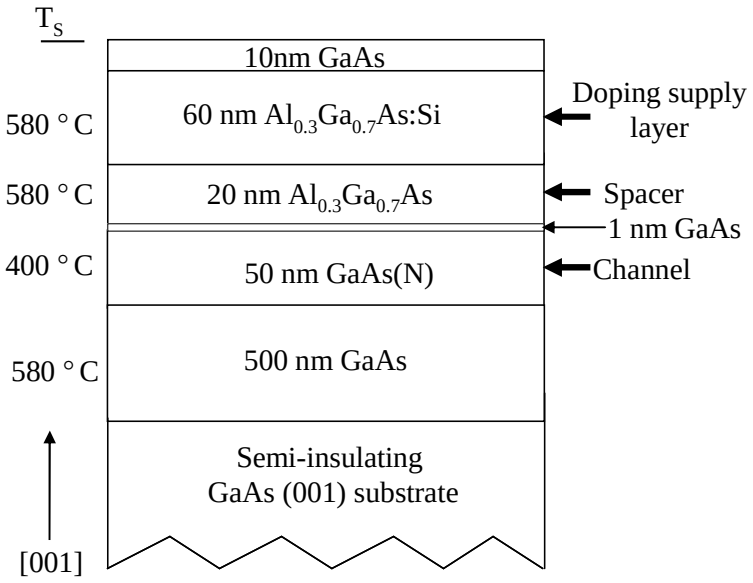

Figure 3.3 Cross-section of AlGaAs/GaAsN modulation-doped heterostructure which consisted of a 50 nm thick GaAs(N) channel layer, 1 nm GaAs, 20 nm undoped $Al_{0.3}Ga_{0.7}As$, 60 nm Si-doped $Al_{0.3}Ga_{0.7}As$, and 10 nm GaAs grown by solid source molecular beam epitaxy. The whole structure is grown on top of 500nm undoped GaAs buffer layer grown at 580˚C.

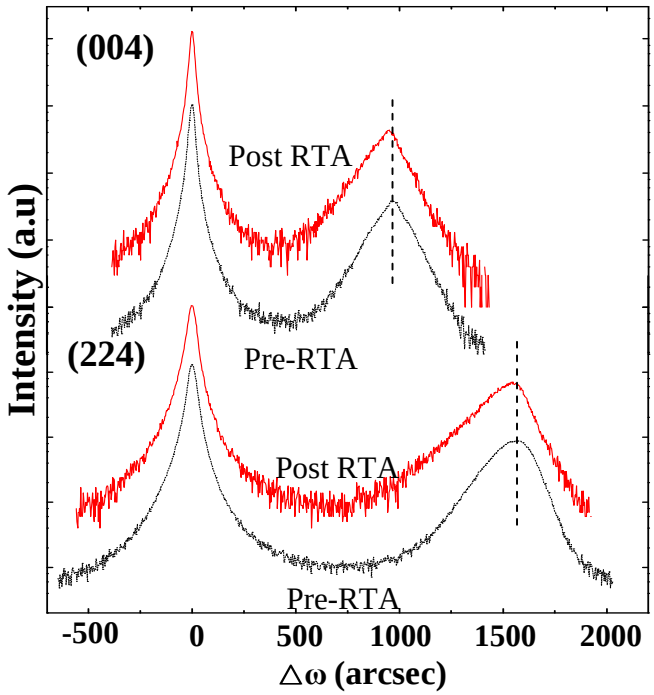

Figure 3.4 (004) and (224) x-ray rocking curves collected from a $GaAs_{0.983}N_{0.017}$ film before and after annealing. In all cases, the substrate reflections are set to 0, and the GaAsN epilayer peaks are marked with a dashed line. For the (004) reflections, the substrate-epilayer peak separation is ~1000 arcsec before and after RTA, suggesting negligible changes in the (004) lattice plane spacing. Similarly, for the (224) reflections, the substrate-epilayer peak separation is ~1500 arcsec before and after RTA. Since both the (004) and (224) lattice plane spacings of the film remain unchanged with RTA, it is likely that the average n composition does not change with RTA.

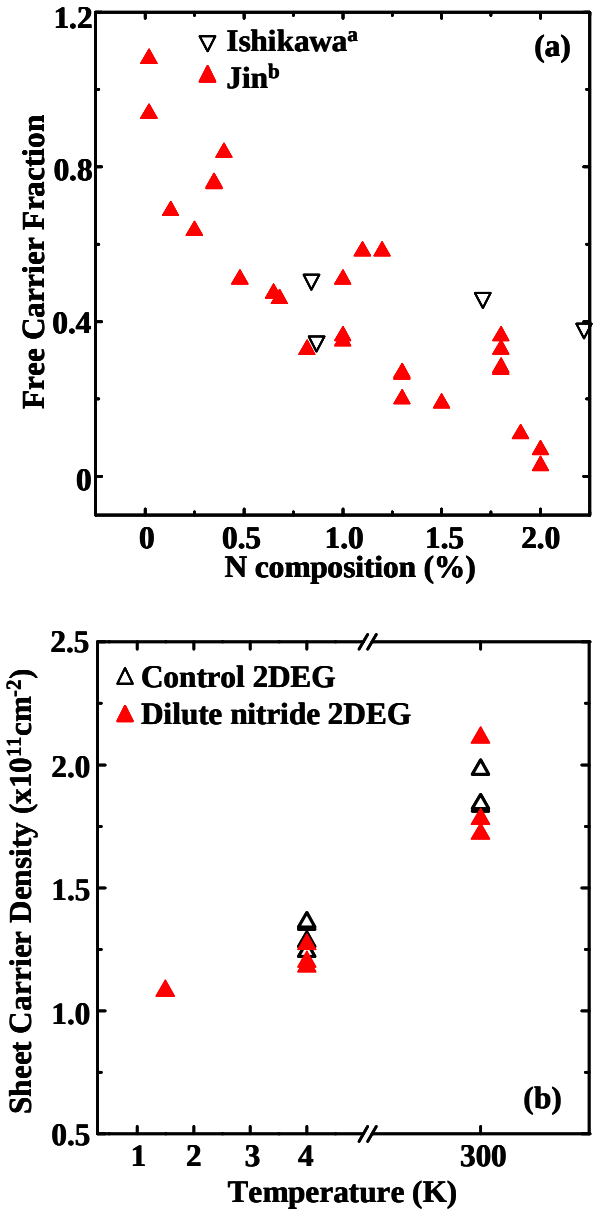

Figure 3.5 (a). Free carrier fraction as a function of N composition, x, for GaAsN:Si bulk-like films. The free carrier fraction is defined as the ratio of free carrier concentration in the GaAsN film to that of the GaAs film doped with equivalent target doping concentration. For comparison, data from Ishikawa *et al.* are also plotted. The free carrier fractions of GaAsN:Si films are significantly lower than unity, and tend to decrease with increasing x. [a]Ref[67], [b]Ref[52] (b). the sheet free carrier concentration, n_s, for several control and nitride 2DEGs, where n_s are similar for the control and dilute nitride 2DEGs at all three measurement-*T*s. Reprinted with permission from Y. Jin *et al.*, Appl. Phys. Lett. **95**, 092109 (2009). Copyright 2009, American Institute of Physics.

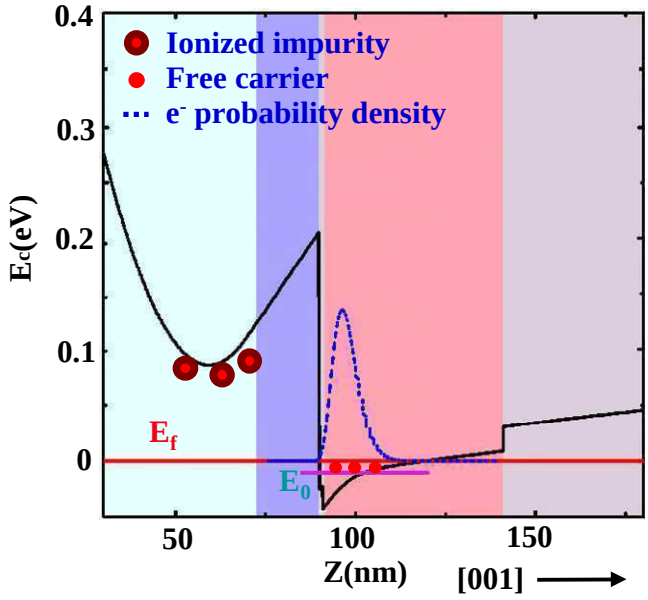

Figure 3.6 CB diagram for the AlGaAs/GaAsN modulation-doped heterostructures calculated with 1D Poisson/Schrödinger simulation software.[53-55] A 2-dimensional electron gas layer is formed near the AlGaAs GaAsN interface, and ionized Si donor in the AlGaAs layer is spatially separated from the GaAsN layer.

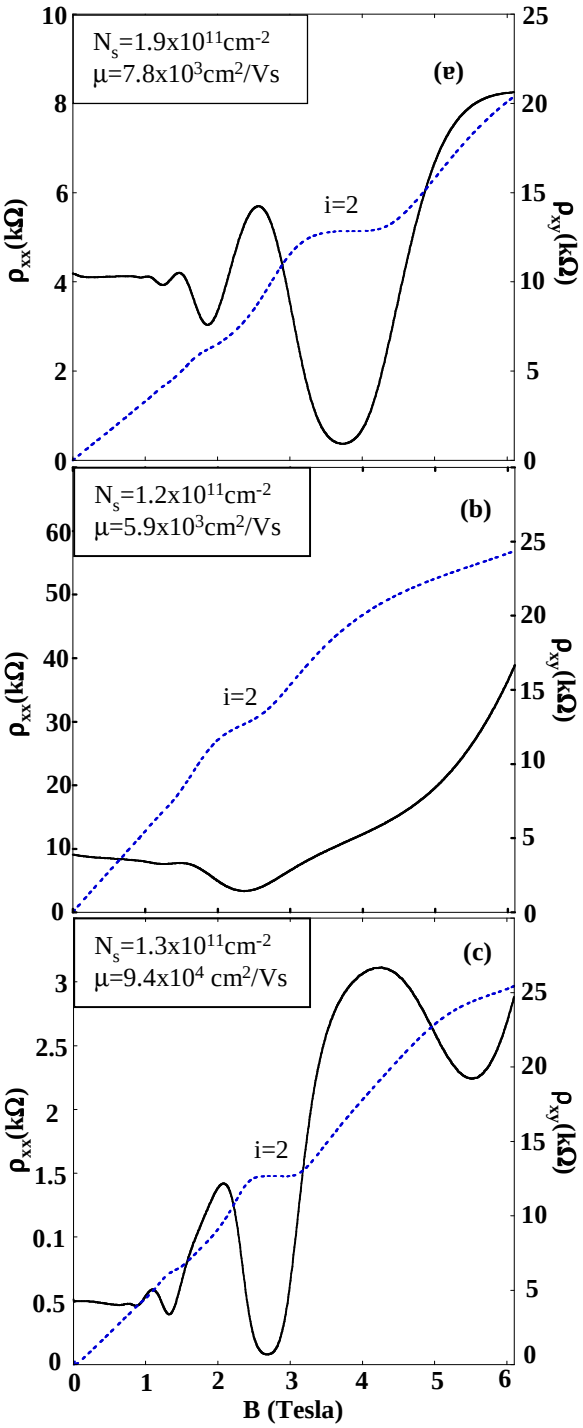

Figure 3.7 Longitudinal (ρ_{xx}, solid line) and transverse (ρ_{xy}, dotted line) resistivity as a function of magnetic field measured at 4K for (a) control and (b) and (c) dilute nitride two-dimensional electron gases. The data were collected prior to (a,b) and following (c) illumination with a light-emitting diode. The second quantum Hall plateaus are labeled as i=2. Reprinted with permission from Y. Jin *et al.*, J. Appl. Phys. **102** 103710 (2007). Copyright 2007, American Institute of Physics.

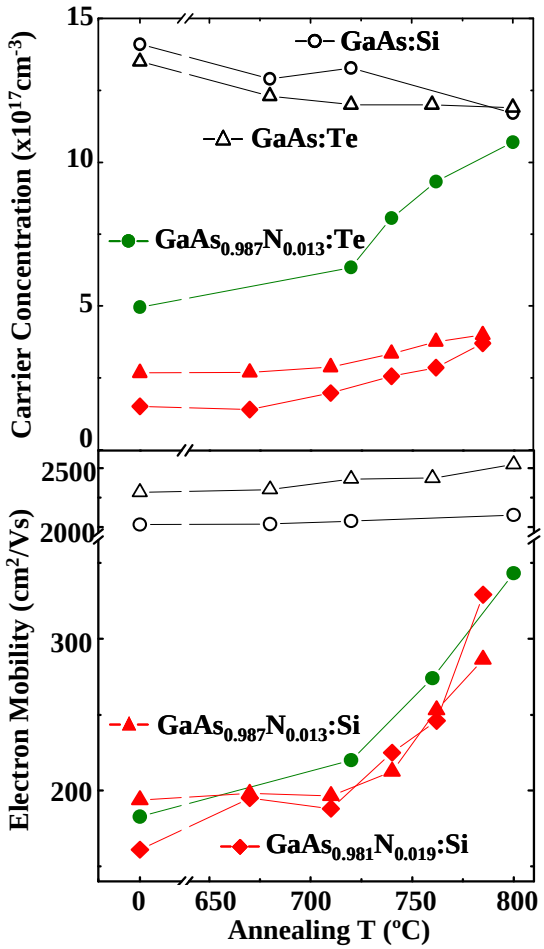

Figure 3.8 Free carrier concentration, *n*, and electron mobility, μ, for GaAs(N):Si and GaAs(N):Te as a function of annealing-*T*. With increasing annealing-*T*, μ increases for both films, while n increases minimally (substantially) for GaAsN:Si (GaAsN:Te) films. Reprinted with permission from Y. Jin *et al.*, Appl. Phys. Lett. **95**, 092109 (2009). Copyright 2009, American Institute of Physics.

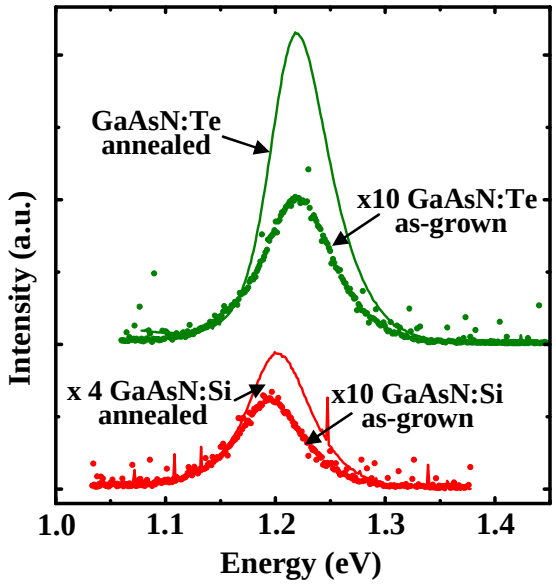

Figure 3.9 Photoluminescence (PL) spectra for as grown and annealed GaAsN:Si and GaAsN:Te films. For the as-grown films, the NBE PL peak emission intensity of GaAsN:Te is 1.5 times higher than that of the GaAsN:Si film. For both films, the FWHM are similar and are reduced ~15% following annealing. However, the PL emission intensity exhibits a 20-fold (6-fold) increase for GaAsN:Te (GaAsN:Si) after annealing. Reprinted with permission from Y. Jin *et al.*, Appl. Phys. Lett. **95**, 092109 (2009). Copyright 2009, American Institute of Physics.

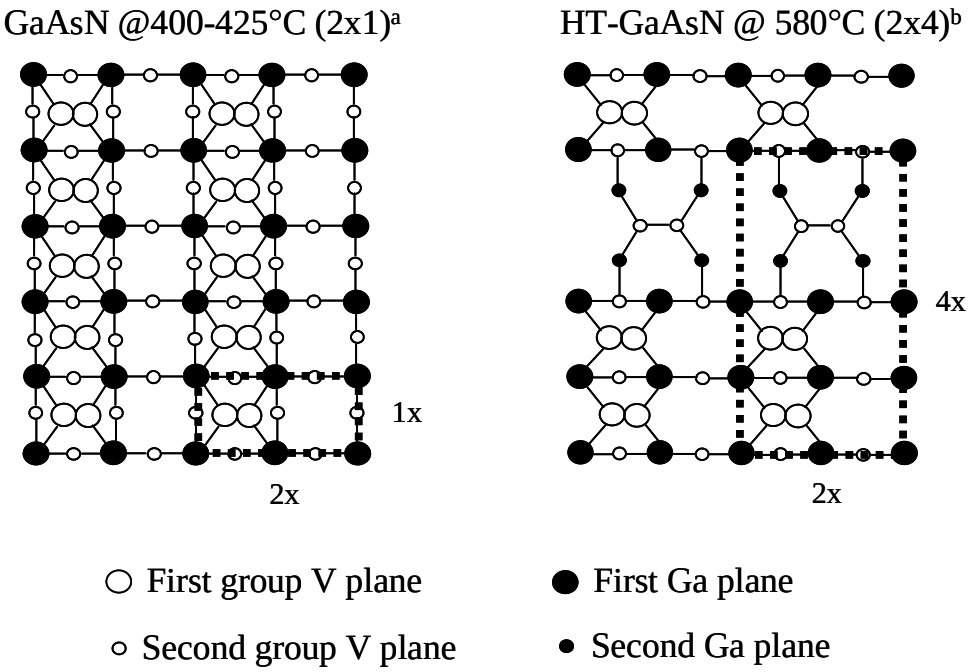

Figure 3.10 Top view of GaAs (001) As-terminated surface reconstructions, (a) 2x1,[60] and (b) 2x4.[61] Open and solid circles represent As and Ga atoms, respectively. Positions in the uppermost two atomic layers are indicated by larger symbols. Since (2 x 4) GaAs surfaces have fewer group V sites per unit area than (2 x 1) GaAs surface, $(N\text{-}Si)_{As}$ are more likely to form on (2 x 4) GaAs surface. Therefore, the enhanced formation of Si-N pairs for HT-GaAsN:Si suggests that $(Si\text{-}N)_{As}$ is the most likely physical model for Si-N complexes in GaAsN:Si.

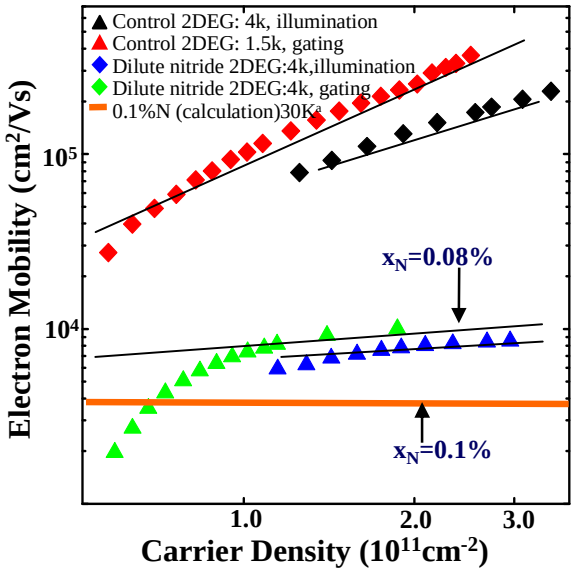

Figure 3.11 Electron mobility as a function of sheet carrier density measured at 4K for control and dilute nitride 2DEG samples. The linear least-squares fits include data points for $n_s > 2x10^{11}cm^{-2}$. For the control sample, $\gamma=1.04$, indicating that the dominant scattering mechanism is remote ionized impurity scattering, while the mobility of the dilute nitride sample flattens out for carrier densities above $2x10^{11}cm^{-2}$, suggesting the dominant source of carrier scattering is short-ranged neutral scatters, likely N interstitial related point defects. [a]See Ref.[63] Reprinted with permission from Y. Jin *et al.*, J. Appl. Phys. **102** 103710 (2007). Copyright 2007, American Institute of Physics.

3.10 References

[1]J. Maguire, R. Murray, R. C. Newman, R. B. Beall and J. J. Harris, Appl. Phys. Lett. **50**, 516 (1987).

[2]J. H. Neave, P. J. Dobson, J. J. Harris, P. Dawson and B. A. Joyce, Appl. Phys. a-Mater **32**, 195 (1983).

[3]E. F. Schubert, *Doping in III-V semiconductors* (Cambridge Universtiy Press, UK, 1993) pp. 192-198.

[4]E. S. Tok, J. H. Neave, M. J. Ashwin, B. A. Joyce and T. S. Jones, J. Appl. Phys. **83**, 4160 (1998).

[5]W. G. Spitzer and M. B. Panishi, J. Appl. Phys. **40**, 4200 (1969).

[6]H. Rupprecht, j. m. Woodall, K. Konnerth and D. G. Pettit, Appl. Phys. Lett. **9**, 221 (1966).

[7]T. Egawa, Y. Niwano, K. Fujita, K. Nitatori, T. Watanabe, T. Jimbo and M. Umeno, Jpn. J. Appl. Phys. 1 **34**, 1270 (1995).

[8]I. Teramoto, J. Phys. Chem. Solids **33**, 2089 (1972).

[9]J. M. Ballingall and C. E. C. Wood, Appl. Phys. Lett. **41**, 947 (1982).

[10]M. Ogawa and T. Baba, Jpn. J. Appl. Phys. 2 **24**, L572 (1985).

[11]J. Nagle, R. J. Malik and D. Gershoni, J. Crys. Growth **111**, 264 (1991).

[12]S. Schuppler, D. L. Adler, L. N. Pfeiffer, K. W. West, E. E. Chaban and P. H. Citrin, Appl. Phys. Lett. **63**, 2357 (1993).

[13]S. Schuppler, D. L. Adler, L. N. Pfeiffer, K. W. West, E. E. Chaban and P. H. Citrin, Phys. Rev. B **51**, 10527 (1995).

[14]R. Nottenburg, H. J. Buhlmann, M. Frei and M. Ilegems, Appl. Phys. Lett. **44**, 71 (1984).

[15]T. Laine, K. Saarinen, J. Makinen, P. Hautojarvi, C. Corbel, L. N. Pfeiffer and P. H. Citrin, Phys. Rev. B **54**, 11050 (1996).

[16]E. F. Schubert, *Doping in III-V semiconductors* (Cambridge Universtiy Press, UK, 1993) pp. 277-290.

[17]Y. M. Houng and T. S. Low, J. Crys. Growth **77**, 272 (1986).

[18]S. Z. Sun, E. A. Armour, K. Zheng and C. F. Schaus, J. Crys. Growth **113**, 103 (1991).

[19]M. J. Antonell, C. R. Abernathy and R. W. Gedridge, J. Crys. Growth **164**, 420 (1996).

[20]I. Ishikawa, T. Saito, S. Sasa and S. Hiyamizu, Appl. Phys. Lett. **21**, L675 (1982).

[21]R. Azoulay, L. Dugrand, D. Ankri and E. V. K. Rao, J. Crys. Growth **68**, 453 (1984).

[22]M. Furukawa and M. Mizuta, Electron. Lett **24**, 1378 (1988).

[23]J. Massies, N. Grandjean and V. H. Etgens, Appl. Phys. Lett. **61**, 99 (1992).

[24]S. H. Lee and G. B. Stringfellow, Appl. Phys. Lett. **73**, 1703 (1998).

[25]S. M. Newstead, T. M. Kerr and C. E. C. Wood, J. Appl. Phys **66**, 4184 (1989).

[26]A. Furukawa and M. Mizuta, Electron. Lett. **24**, 1378 (1988).

[27]S. Subbanna, G. Tuttle and H. Kroemer, J. Electron. Mater. **17**, 297 (1988).

[28]B. R. Bennett, R. Magno and N. Papanicolaou, J. Crys. Growth **251**, 532 (2003).

[29]K. Volz, J. Koch, B. Kunert and W. Stolz, J. Crys. Growth **248**, 451 (2003).

[30]M. Reason, Y. Jin, H. A. McKay, N. Mangan, D. Mao, R. S. Goldman, X. Bai and C. Kurdak, J. Appl. Phys. **102**, 103710 (2007).

[31]K. M. Yu, W. Walukiewicz, J. Wu, D. E. Mars, D. R. Chamberlin, M. A. Scarpulla, O. D. Dubon and J. F. Geisz, Nat. Mater. **1**, 185 (2002).

[32]J. Li, P. Carrier, S.-H. Wei, S.-S. Li and J.-B. Xia, Phys. Rev. B **93**, 035505 (2006).

[33]A. Janotti, P. Reunchan, S. Limpijumnong and C. G. Van de Walle, Phys. Rev. Lett. **100**, 045505 (2008).

[34]I. A. Buyanova, G. Pozina, P. N. Hai, N. Q. Thinh, J. P. Bergman, W. M. Chen, H. P. Xin and C. W. Tu, Appl. Phys. Lett. **77**, 2325 (2000).

[35]Y. Jin, R. M. Jock, H. Cheng, Y. He, A. M. Mintarov, Y. Wang, C. Kurdak, J. L. Merz and R. S. Goldman, Appl. Phys. Lett. **95**, 062109 (2009).

[36]L. H. Li, Z. Pan, W. Zhang, Y. W. Lin, Z. Q. Zhou and R. H. Wu, J. Appl. Phys. **87**, 245 (2000).

[37]M. Ramsteiner, D. S. Jiang, J. S. Harris and K. H. Ploog, Appl. Phys. Lett. **84**, 1859 (2004).

[38]P. Krispin, S. G. Spruytte, J. S. Harris and K. H. Ploog, Physica B **308**, 870 (2001).

[39]K. M. Yu, W. Walukiewicz, J. Wu, D. E. Mars, D. R. Chamberlin, M. A. Scarpulla, O. D. Dubon and J. F. Geisz, Nat. Mater. **1**, 185 (2002).

[40]R. Mouillet, L. A. de Vaulchier, E. Deleporte, Y. Guldner, L. Travers and J. C. Harmand, Solid State Commun. **126**, 333 (2003).

[41]D. Fowler, O. Makarovsky, A. Patane, L. Eaves, L. Geelhaar and H. Reichert, Phys. Rev. B **69**, 153305 (2004).

[42]Y. G. Hong, C. W. Tu and R. K. Ahrenkiel, J. Cryst. Growth **227**, 536 (2001).

[43]C. Jiang, D. C. Tsui and G. Weimann, Appl. Phys. Lett. **53**, 1533 (1988).

[44]A. Gold, Phys. Rev. B **44**, 8818 (1991).

[45]K. Hirakawa, H. Sakaki and J. Yoshino, Surf. Sci. **170**, 440 (1986).

[46]K. Hirakawa and H. Sakaki, Phys. Rev. B **33**, 8291 (1986).

[47]M. Reason, N. G. Rudawski, H. A. McKay, X. Weng, W. Ye and R. S. Goldman, J. Appl. Phys. **101**, 083520 (2007).

[48]H. Q. Hou, B. W. Liang, T. P. Chin and C. W. Tu, Appl. Phys. Lett. **59**, 292 (1991).

[49]H. L. Stormer, R. Dingle, A. C. Gossard, W. Wiegmann and M. D. Sturge, Solid State Commun. **88**, 933 (1993).

[50]G. Weimann, W. Schlapp and H. Burkhard, Phys. Stat. Sol. A **64**, K99 (1981).

[51]H. L. Stormer, A. C. Gossard, W. Wiegmann and K. Baldwin, Appl. Phys. Lett. **39**, 912 (1981).

[52]F. Ishikawa, G. Mussler, K. J. Friedland, H. Kostial, K. Hagenstein, L. Daweritz and K. H. Ploog, Appl. Phys. Lett. **87**, 262112 (2005).

[53]1D Poisson/Schrodinger, Greg Snider, U-Notre Dame; www.nd.edu/~gsnider; downloaded 10:47pm (January 24, 2010)

[54]G. L. Snider, I. H. Tan and E. L. Hu, J. Appl. Phys. **68**, 2849 (1990).

[55]I. H. Tan, G. L. Snider, L. D. Chang and E. L. Hu, J. Appl. Phys. **68**, 4071 (1990).

[56]K. von Klitzing, G. Dorda and M. Pepper, Phys. Rev. Lett. **45**, 494 (1980).

[57]J. Li, P. Carrier, S. H. Wei, S. S. Li and J. B. Xia, Phys. Rev. Lett. **96**, 035505 (2006).

[58]E. F. Schubert, J. B. Stark, T. H. Chiu and B. Tell, Appl. Phys. Lett. **53**, 293 (1988).

[59]Y. G. Chai, R. Chow and C. E. C. Wood, Appl. Phys. Lett. **39**, 800 (1981).

[60]Y. C. Chang and D. E. Aspnes, Phys. Rev. B **41**, 12002 (1990).

[61]W. G. Schmidt, Appl. Phys. a-Mater **75**, 89 (2002).

[62]M. Reason, H. A. McKay, W. Ye, S. Hanson, R. S. Goldman and V. Rotberg, Appl. Phys. Lett. **85**, 1692 (2004).

[63]S. Fahy, A. Lindsay, H. Ouerdane and E. P. O'Reilly, Phys. Rev. B **74**, 035203 (2006).

[64]J. H. Davies, *The Physics of Low-Dimensional Semiconductors* (Cambridge University Press, 1998) pp. 356-365.

[65]J. J. Harris, J. A. Pals and R. Woltjer, Rep. Prog. Phys. **52**, 1217 (1989).

[66]C. Jiang, D. C. Tsui and G. Weimann, Appl. Phys. Lett. **53**, 1533 (1988).

[67]Y. Jin, Y. He, H. Cheng, R. M. Jock, T. Dannecker, M. Reason, A. M. Mintairov, C. Kurdak, J. L. Merz and R. S. Goldman, Appl. Phys. Lett. **95**, 092109 (2009).

CHAPTER 4

INFLUENCE OF INTRINSIC N POINT DEFECTS ON THE ELECTRONIC PROPERTIES OF GaAsN

4.1 Overview

This chapter describes the investigation of intrinsic N point defects on the electronic and optical properties of GaAsN alloy films. As discussed in Section 1.4, the intrinsic N point defects refer to defects that do not involve the introduction of additional external elements such as donors. To ensure the conclusions of this chapter are independent of dopant species, all measurements were performed for both Si and Te doped GaAsN films, and similar results were observed in both cases.

This chapter opens with background information relevant to intrinsic N-related point defects in GaAsN. We first summarize earlier studies of the influence of annealing on the electronic properties of GaAsN. We then review the physical phenomena discussed in the chapter, including the metal-insulator transition (MIT), hopping and variable range hopping (VRH) conduction, and the persistent photoconductivity (PPC) effect. Next, the experimental details are described. The bulk of the chapter is then devoted to the examination of the influence of intrinsic N point defects on the electronic properties of GaAsN alloy films.

We observed three effects in as-grown GaAsN that are removed or reduced after rapid thermal annealing (RTA), all of which are explained by the corresponding reduction of the N interstitial fraction, f_{int}, following RTA. First, for the as-grown GaAsN films, we observed a metal-insulator transition (MIT) with an onset at a much higher carrier concentration than what has been observed in GaAs. The MIT in $GaAs_{1-x}N_x$ is accompanied by a shrinkage of electron Bohr radius with increasing x, suggesting a x-dependent increase in electron effective mass. In addition, temperature-dependent transport measurements reveal a N-induced electron trapping level below the GaAsN conduction band (CB) edge and a persistent photoconductivity (PPC) effect. Following RTA, a significant increase in n and μ is observed with a transition in the low T transport mechanisms from hopping to extended band conduction. In addition, following RTA, the T dependence of n is suppressed and the PPC effect vanishes, presumably due to a reduced concentration of N-induced electron traps. Finally, nuclear reaction analysis reveals an RTA-induced decrease in f_{int}; corresponding signatures for the reduced f_{int} are also identified in Raman spectra. Thus, it is likely that the N interstitial defects are responsible for the MIT, the shrinkage in electron Bohr radius, the N-induced trapping level, and PPC effect discussed above. Therefore, N interstitials are likely the dominant form of intrinsic N defects in GaAsN alloys.

4.2 Background

4.2.1 Effect of annealing on GaAsN alloys

In dilute nitride (In)GaAsN alloys, RTA can drastically improve the near-band-edge (NBE) emission photoluminescence (PL) efficiency by a factor of 30-75.[1-3] This improvement was initially attributed to N out-diffusion during annealing.[4, 5] However, in later studies, XRC revealed a negligible influence of RTA on the lattice parameter of (In)GaAsN films, suggesting insignificant annealing-induced N out-diffusion.[6, 7] Buyonova *et al.* argued that annealing of GaAsN alloys reduces the disorder due to fluctuations in alloy composition and local strain, leading to the elimination of the so-called "competing non-radiative channels".[7-9] It has also been proposed that the low GaAsN growth temperature (400 ºC) leads to a high concentration of V_{Ga}, which are in turn removed by annealing.[1, 10] However, as will be discussed in Appendix D.3, for both the "low" and "high" temperature grown GaAs films, similar electron mobilities were observed, suggesting that significant V_{Ga} are not likely to be present in either GaAs or GaAsN alloys. Therefore, it is likely that V_{Ga} is not the dominant source of electron trapping and scattering centers in GaAs(N) alloys.

The effect of annealing f_{int} has been discussed by several groups, and contradicting conclusions have been reported. [11, 12, 13-15] Ramsteiner *et al.* and Mussler *et al.* found that the intensity of Raman features, which they assigned to $(NN)_{As}$, was reduced by annealing at 800 °C.[2, 14] Krispin *et al.* showed the deep level at 0.8 eV above the valence band (VB) edge, which they attributed to $(NN)_{As}$, is removed by annealing at 720 °C.[3, 16] However, the quantitative comparison of f_{int} before and after RTA is limited to two data points in two papers.[11, 12] Using NRA, Spruytte *et al.* report a lower

channeling yield for one $GaAs_{0.97}N_{0.03}$ film after annealing at 760 °C for 1 min. Also using NRA, Ahlgren *et al*. reported an RTA-induced (750 °C for 30 s) decrease in the N channeling to random ratio for a $GaAs_{0.956}N_{0.043}$ film. Both results suggest a RTA-induced reduction in f_{int}.[11, 12] On the other hand, it has also been reported that RTA increases f_{int}. Loke *et al*. reported a redshift (wavelength increase) in the GaAsN NBE PL following annealing in the range of 550 to 700 °C for 10min, which they attributed to a "kick-out" effect of the substitutional As atoms by interstitial nitrogen atoms, leading to an increase in f_{int}.[17, 18] To date, the influence of annealing on the f_{int} in (In)GaAsN, and the relationship between interstitial N incorporation and the electronic properties of (In)GaAsN remain unknown.

4.2.2 Metal-insulator transition in semiconductors

In heavily doped semiconductors, the resistivity, ρ, is typically a weak function of temperature. This is because the shallow donors form an impurity band near the conduction band edge (i.e., with negligible ionization energy), leading to a temperature-independent carrier concentration.[19] In semiconductors with very low doping concentration or in strongly compensated semiconductors, the free carrier concentration decreases with temperature. At low temperature, the contribution of the free carriers to the conductivity, σ, becomes negligible, and the carrier transport occurs via thermally activated hopping between localized states, often termed "hopping conduction". In hopping conduction, the jump probability is temperature-dependent; thus, the resistivity is expected to have exponential temperature dependence, as follows:

$$\rho \sim \exp(\varepsilon / k_B T) \tag{4.1}$$

where ε is the activation energy of hopping. Typically, carriers that undergo hopping conduction have a very low mobility, since the electron jumps are associated with a weak overlap of wave-function tails from neighboring donors.

As the doping concentration further decreases, the typical resistances between neighboring impurities become larger than those between remote impurities with energy levels near the Fermi level. In this case, the characteristic hopping length decreases with increasing temperature, following Mott's law for variable-range hopping (VRH) conduction:

$$\rho \sim \exp((\frac{T_0}{T})^{1/4}) \tag{4.2}$$

with $T_0 = \frac{\beta}{k_B g(E_f) a_B{}^3}$, k_B is Boltzmann's constant, $g(E_f)$ is the density of states at the Fermi level; a_B is the Bohr radius, which is assumed to be equivalent to the localization radius for states near the Fermi level; β is a unitless quantity calculated to be 21.2 ± 1.2, using Monte Carlo simulations.[20]

As the free carrier concentration of a semiconductor decreases, the semiconductor undergoes a metal-insulator transition (MIT), which has been described both macroscopically and microscopically. For the macroscopic definitions of metal or insulator, the temperature dependence of σ is extrapolated to 0 K using an expression derived by Altshuler and Aronov: [21, 22]

$$\sigma = \sigma_0 + bT^{1/2} \tag{4.3}$$

with metals (insulators) having $\sigma_0 > 0$ ($\sigma_0 < 0$), and an MIT at $\sigma_0 = 0$; b is a dependent on

the critical conductance and the density of states at the Fermi level of the material. On the other hand, for the microscopic picture, MIT occurs when the average distance between free carriers increases beyond the extension of the free-carrier Bohr radius. Mott quantified this microscopic picture by equating the effective valence electron-cation potential in an atom and the electron-electron screening potential, and thereby deriving the following relation between carrier concentration and Bohr radius at the MIT point:

$$n_c^{1/3} a_B \approx 0.25 \tag{4.4}$$

where n_c is the critical carrier concentration for MIT. For example, the Mott criterion predicts a critical carrier concentration of n_c = 1.56 x 10^{16} cm^{-3} in GaAs.[21] Therefore, the determination of n_c will enable us to derive a_B, which in turn, enables the derivation of m_e*,as follows:

$$m_e^* = \frac{4\pi\varepsilon\hbar^2}{a_B e^2} \tag{4.5}$$

4.2.3 Persistent photoconductivity

Persistent photoconductivity (PPC) refers to a phenomenon where an illumination-induced increase in σ persists following the termination of illumination, usually on the order of hours or even days.[23-25] PPC has been observed in various compound semiconductors, such as AlGaAs, InP, and GaAsP, as well as other materials, such as polycrystalline Si, Ge, and carbon nanotubes.[26-33] The PPC effect has been explained by various models, including the microscopic random potential fluctuation model, [34-36] the artificial macroscopic potential barrier model,[37, 38] and the large lattice

relaxation (LLR) model. [24, 25 39, 40] In the microscopic random potential fluctuation model, the separation of photoexcited carriers by local-potential fluctuations is believed to be the origin of PPC.[34] For example, this mechanism has been used to explain the origin of PPC effect in ZnCdSe alloy semiconductors.[35, 36] PPC has also been observed in artificially constructed heterostructures, such as n-i-p-i doping superlattices,[37, 38] where the artificial macroscopic potential barrier at surfaces and interfaces prevents electron-hole recombination.

The LLR model has been successfully applied to explain a variety of PPC-related experimental observations in AlGaAs.[39, 40] In the LLR model, two donor configurations co-exist in AlGaAs. When donor atoms such as Si and Te occupy group III sites, they act as shallow donors and contribute free carriers to the CB. When donor atoms incorporate interstitially, they act as deep donor levels and trap electrons at low temperatures. These deep donors are referred to as donor-complex (DX) centers.[24, 25] Upon illumination, the electrons trapped in the DX-centers are photo-excited to the CB, generating photocurrent. At the same time, DX-centers undergo a large lattice relaxation and become shallow donor states.[24, 25] A large energy barrier between the metastable shallow donor state and the DX-center state prevents the donor atoms and the photo-excited electrons from relaxing back to the equilibrium DX-center state. Therefore, even after the illumination is terminated, the increase in photocurrent persists for a long time. Upon thermal annealing, enough energy is provided to the lattice to overcome the energy barrier and relax to the DX-center state, and the photocurrent decays to its value prior to illumination.

The PPC effect has been reported in InGaAsN alloys. Li *et al.*[41] observed PPC in unintentionally doped p-type InGaAsN; Hsu *et al.*[42, 43] observed the PPC effect in an

unintentionally doped n-type InGaAsN sample. However, the origin of the PPC effect has been vaguely attributed to some unknown N-related DX or acceptor-complex (AX) centers, [41] [42, 43] and the atomic structure of these centers remains unknown.

4.3 Experimental Details

The samples used in this study are MBE-grown GaAsN bulk-like films doped with Si or Te, as described in Section 3.3. The film characterization techniques, including room temperature and variable temperature transport measurements, ion beam analysis, and Raman spectroscopy, were also described in Chapter 2.

For the PPC effect study, a light emitting diode (LED) with emission wavelength in the range of 940-950 nm was mounted in the cryostat, as described in Section 2.8. Prior to illumination, the GaAsN bulk-like films were cooled down to the measurement temperature. To achieve thermal equilibrium, samples were held at the measurement T for > 10 minutes, and then illuminated until saturation of the decrease in ρ, typically 30 – 60 s. Throughout the measurement, the LED power was fixed at ~15 mW. After the LED was switched off, ρ was recorded as a function of time for ~1 hr. In one case, ρ was recorded for 12 hrs. To ensure that each set of relaxation data was obtained with the same initial equilibrium conditions, the samples were always re-heated to 230 K for at least 30 minutes to achieve thermal equilibrium (without illumination) before cooling to the next measurement temperature.

PPC was also utilized to determine μ as a function of n in GaAsN films. For this purpose, Hall measurements were performed immediately following cessation of illumination. At 40 K and 80 K, n and μ were first measured in the dark. Next, the LED

was briefly powered to increase *n*, and *n* and μ were then measured again following cessation of illumination. This process was repeated until *n* was saturated and did not increase with further illumination.

4.4 Electronic properties of as-grown GaAsN films

4.4.1 Metal-Insulator-Transition in GaAsN alloys

As discussed in Section 4.2, near MIT, σ can be described by Eq. 4.3. As shown in Fig. 4.1, for $GaAs_{1-x}N_x$ films with various x and similar *n*, σ is plotted as a function of measurement $T^{1/2}$. Below 15K, the dashed lines are linear-least-square fits of σ, with the y-intercept defined as σ_0. As shown in Fig. 4.1, σ decreases as x increases, with $\sigma_0 \sim 0$ at x =0.013. For the x=0.013 film, the carrier concentration is determined by Hall measurements to be ~ $2x10^{17}$ cm^{-3}. Indeed, the critical carrier concentration for MIT in $GaAs_{0.987}N_{0.013}$ is one order of magnitude larger than what has been reported for GaAs, $1.56x10^{16}$ cm^{-3}.[21]

In GaAs, MIT occurs at a low *n* since as n decreases, the average distance between carriers becomes larger than the electron Bohr radius, a_B, and the carrier wavefunctions do not overlap. In GaAsN, MIT occurs at a much higher *n*, presumably due the smaller a_B in GaAsN in comparison to that of GaAs. As shown in Eq. 4.4, for films at the MIT point, by inserting $n_c = 2x10^{17}cm^{-3}$ into Eq. 4.4, a_B for $GaAs_{0.987}N_{0.01.3}$ is determined to be 5 nm, about half the a_B value in GaAs (a_B (GaAs)=10 nm).

The electron Bohr radius, a_B, can also be extracted by applying the VRH formalism (Eq. 4.2). In Fig. 4.2, we plot the resistivity, ρ, as a function of measurement temperature $T^{-1/4}$, for $GaAs_{1-x}N_x$ films with various x. For the control GaAs film, ρ

remains constant throughout the entire temperature range (1.6 K to 200 K), as expected for a degenerately-doped semiconductor.[44] For $GaAs_{1-x}N_x$ films with low x (< 0.01), ρ increases slightly with decreasing T; for the films with higher x (> 0.01), ρ increases exponentially as T decreases, suggesting the onset of hopping conduction. For x > 0.013, as discussed earlier in this section, the films become insulating, and VRH conduction dominates. In the VRH regime, T_0 is extracted from the slope of ln ρ vs. $T^{-1/4}$ in Fig. 4.2 (slope = $T_0^{1/4}$). For $GaAs_{0.987}N_{0.013}$, using a_B derived from the Mott criterion (Eq. 4.4), g(E_f) was estimated as 1.84×10^{21} $cm^{-3}eV^{-1}$. Assuming g(E_f) is similar for all $GaAs_{1-x}N_x$ films, the localization radius can then be estimated as a function of x, as shown in Table 4.1. The localization radii with * are for films with x ~ 0.013, near the MIT point, where the VHR formalism may not be applicable. Evidently, there is a trend of decreasing a_B with increasing x, suggesting carriers became more localized as x increases.

Table 4.1: Electron Bohr radius, a_B, and density of states at Fermi level, g(E_f), estimated for $GaAs_{1-x}N_x$ films with various x and dopant species. a_B with * are for films with x=0.013, near the MIT point; in those cases, the variable range hopping formalism may not be applicable.

RMBE	x	Dopant	T_0	a_B (nm)	g(E_f) ($eV^{-1}cm^{-3}$)
421	0.006	Si	-	-	-
420	0.010	Si	27		-
419	0.013	Si	287	8 *	-
596	0.013	Te	229	8 *	-
597	0.013	Si	1061	5	1.84×10^{21}
598	0.019	Te	18000	2	-
599	0.019	Si	<4000000	>0.3	-

The electron effective mass, m_e*, can be deduced from a_B using Eq. 4.5. For example, m_e* for $GaAs_{0.987}N_{0.01.3}$ film is determined to be 0.13 m_e, twice the value of m_e*

in GaAs ($0.067m_e$), and is in qualitative agreement with m_e* measured by various other experimental techniques.[45,46] As schematically shown in Fig. 4.3, N-related point defects induce potential fluctuations near the CB edge of GaAsN, leading to carrier localization. Thus, the shrinkage of a_B with increasing x likely leads to the corresponding increase in m_e^*.

4.4.2 N-induced carrier trapping state

Variable temperature Hall and resistivity measurements were used to examine the temperature dependence of *n* in GaAsN. Figure 4.4 shows a plot of log *n* vs. reciprocal *T* for as-grown and annealed $GaAs_{0.981}N_{0.019}$:Te films, in comparison with as-grown GaAs:Te. For GaAs:Te, *n* is *T*-independent in the range 50 to 300 K, typical of degenerately-doped semiconductors.[6] However, for GaAsN:Te films, there are two distinct *T* dependent regimes: for $T > 150$K, *n* increases exponentially with increasing *T*; for $T < 150$K, *n* is independent of *T*.

This T-dependence of n is reminiscent of the behavior in n-type AlGaAs, where two T-dependent regimes of n are observed, and are attributed to the co-existence of a shallow donor level and a deep electron trapping level.[47] Similar coexistence of Si/Te induced-shallow donor level and N-induced deep electron trapping level is likely occurring in GaAsN. As shown in Fig. 4.4, for GaAsN, the saturation of n below 150 K is attributed to the shallow Te donors that do not freeze out at very low T. The exponential increase in *n* above 150 K is likely due to the thermal activation of electrons that are trapped by N-induced deep levels below 150K.

Next, we extracted the thermal activation energy of the N-induced deep donor, E_a,

from the *T* dependence of *n*. However, the formulas frequently used to determine donor activation energies, $n \propto \exp(-\frac{E_a}{2k_BT})$ or $n \propto \exp(-\frac{E_a}{k_BT})$ cannot be used for cases such as this one, where shallow and deep donors co-exist in a semiconductor. Instead, E_a must be determined using a 2-level system formalism:[6]

$$\sqrt{n(n-n_S)} \propto \exp(-\frac{E_a}{2k_BT}) \tag{4.6}$$

where k_B is Boltzmann constant, *n* is the apparent free carrier concentration, and n_s is the saturated shallow donor concentration. In Fig. 4.4, $\sqrt{n(n-n_S)}$ is plotted (in open circles) vs. reciprocal *T* for $n > n_s$, overlaid on the *n* vs. reciprocal *T* plot, and E_a are extracted from the slope of the least square fit of $\sqrt{n(n-n_S)}$. Summarized in Table 4.2 is the resulting E_a values for $GaAs_{1-x}N_x$ films with various x and annealing *T*s. For, $GaAs_{1-x}N_x$ alloys with x = 0.075-0.019, E_a = 60-116 meV, which is significantly greater than the activation energy of shallow donors in GaAs (the activation energy for Si and Te donors in GaAs are 4-6 meV and 30 meV, respectively[48]), suggesting that the N-induced defect state acts as a carrier trapping center, even at room *T* (k_BT = 26 meV << E_a = 60-116 meV)

Since the thermal activation of *n* is observed in GaAsN films but not in GaAs control films, the trapping level is likely due to N-related defects. Furthermore, E_a is essentially independent of n-type dopant species, suggesting that the N-related defects are intrinsic point defect.

Table 4.2: Shallow donor concentration, n_s, and thermal activation energy, E_a determined as described above for $GaAs_{1-x}N_x$ films with various x and annealing *T*s.

RMBE	x	Dopant	Annealing *T* (ºC)	n_s ($x10^{17}cm^{-3}$)	E_a
578	0.012	Te	0	0.8	116
			700	3.4	NA
			740	4.5	NA
596	0.013	Te	0	3.0	87
597	0.013	Si	0	0.9	86
576	0.016	Te	0	NA	>88
			700	0.5	95
			740	1.0	96
			760	2.0	85
			780	3.80	NA
598	0.019	Te	0	1.2	60
			670	2.0	75
			710	2.5	65
			740	6.9	63
			780	9.2	NA

4.4.3 Persistent photoconductivity in GaAsN alloys

Shown in Fig. 4.6 is a typical set of 40K normalized photoconductivity data, g_t^N, for a GaAsN film, plotted as a function of time prior to commencement of and following termination of illumination. For the purpose of analysis, t=0 is defined as the instant that the illumination is terminated. The normalized conductivity, g_t^N, is defined as:

$$g_t^N = \frac{g_t - g_d}{g_0} = (\frac{1}{\rho_t} - \frac{1}{\rho_d}) / \frac{1}{\rho_0} \tag{4.7}$$

where ρ_d is the resistivity prior to illumination (often termed "dark resistivity"), ρ_0 is the resistivity at $t = 0$, ρ_t is the resistivity at time *t*; and g_d, g_0 and g_t are the inverse of ρ_d, ρ_0 and ρ_t, respectively. g_t^N is defined in this manner so that the decay curves are

normalized to unity at t = 0. In addition, the conductivity prior to illumination, g_d, is subtracted from the measured conductivity, so that g_t^N represents only the contribution from photo-generated free carriers. As shown in Fig. 4.6, the reduction of photo-generated current is less than 5% in 12 hours, suggesting the presence of the PPC effect in GaAsN films. PPC is observed from 1.6 K up to 160 K. Above 160 K, the photogenerated current decays rapidly, and within a few seconds, the film resistivity relaxes to it value prior to illumination.

To extract the characteristic PPC capture barrier, E_c, we examine the decay kinetics of the photo-generated conductivity in GaAsN films. For example, Fig. 4.7 (a) shows g_t^N of a GaAsN film plotted as a function of time measured at various *T*s. At low *T*, the resistivity increases slowly with time, indicating the presence of PPC. The decay mechanism of PPC is usually described by a stretched-exponential relaxation model:

$$g_t^N = \exp(-(\frac{t}{\tau})^\beta) \tag{4.8}$$

where τ is the characteristic decay time and β is the decay exponent. This behavior is commonly observed in disordered systems, where the deviation from standard exponential decay is usually due to an exponential distribution of barrier energies. In Fig. 4.7(b), to consider the stretched-exponential relaxation model, the normalized conductivity is re-plotted in the form of $\ln(\ln(1/g_t^N))$ vs. $\ln(t)$. For each *T*, we used linear least-squares fits to Fig. 4.7 (b) to determine τ, as labeled in the plot. We found that τ decreases rapidly with increasing *T*. A typical example of τ plotted as a function of inverse measurement *T* is shown in Fig. 4.8. Ln (τ) is linearly dependent on the inverse measurement temperature as follows:

$$\tau = \tau_0 \exp(\frac{E_c}{k_B T}) \quad (4.8)$$

where τ_0 is the high temperature limit of τ, and E_c is the characteristic PPC capture energy barrier. The linear dependence of Ln (τ) on 1/T suggests that the relaxation of PPC effect is thermally activated, presumably due to the T-dependent probability for localized carriers to overcome E_c. From the slope of the plot in Fig. 4.8, the resulting E_c can be determined, as summarized in Table 4.3. These values are similar to the E_c reported by Li and Hsu in similar (In)GaAsN alloys (also included in Table 4.3), [41-43] and are ~ 2x the value of E_c observed in n-type AlGaAs, attributed to the presence of DX-centers.

Table 4.3: Characteristic PPC capture barrier, E_c, for $GaAs_{1-x}N_x$ films with various x and n-type dopant species. The results from Li *et al.* [41] and Hsu *et al.* [42, 43] are also included.

RMBE	x	dopant	E_c (meV)	Error (meV)
596	0.013	Te	350	16
598	0.019	Te	216	26
583	0.016	Te	224	35
584	0.012	Te	232	41
597	0.013	Si	235	51
Li	$In_{0.05}Ga_{0.95}As_{0.097}N_{0.013}$	NA	570	NA
Hsu	$In_{0.11}Ga_{0.89}As_{0.0992}N_{0.008}$	NA	349	NA

This PPC effect and the thermally activated n discussed in the Section 4.4.2 are very similar to effects observed in n-type AlGaAs (discussed in Section 4.2.3), suggesting that both PPC effects have similar origins. As shown in Fig. 4.9, within the framework of LLR model discussed in Section 4.2.3, we consider a configuration coordinate diagram for GaAsN, where two distinct N interstitial related states coexist in GaAsN: one shallow donor state near the CB edge, and another deep state. When the

deep state is photoexcited, it converts into the shallow donor state and releases free electrons to the CB. An energy barrier between the deep and shallow states prevents the system from relaxing and recapturing the free electron. To reveal the exact physical model for this interstitial N-related defect, more experimental and theoretical modeling are needed. For example, to reveal the spectral response of the defect states, PPC measurements should be performed using a light source with tunable wavelengths.[49]

Furthermore, the PPC effect provides a unique opportunity to vary *n* continuously in a single sample through the variation of photon excitation dose (i.e., the duration of illumination at a fixed intensity), without having to grow and fabricate multiple samples with different doping concentrations. As shown in Fig. 4.10, at 40 K, as *n* is increased with illumination from 2.2 to $4x10^{17}cm^{-3}$, μ increases monotonically from 50 to 140 cm^2/Vs. A similar trend is observed at 80 K with μ shifted to a higher value for all *n* values. The dependence of carrier scattering on the position of the Fermi level suggests the existence of a N-induced "mobility edge", i.e. a tail of states near the CB minimum. This concept is depicted qualitatively in Fig. 4.11, which is a schematic of the density of states (DOS) near the CB edge of GaAsN. In the shaded area, due to the resonance between the N-induced localized states and the CB edge of GaAs, a tail of states is apparent near the band edge. Prior to commencement of illumination, *n* is low and the Fermi level lies within the N-induced localized states. In this case, carrier transport is governed by hopping or variable range hopping (VRH). Since the electron jumps are associated with a weak overlap of wave-function tails from neighboring donors, low values of μ are observed. Upon illumination of the GaAsN films, the Fermi level moves

up to the weakly localized or delocalized states. Carrier transport is then governed by extended state band conduction, and both n and μ increase.

4.5 Effect of annealing on GaAsN alloys

Following RTA, we examined the transport and structural properties of GaAsN, comparing them with those in the as-grown films. Specifically, the transport properties and f_{int} are measured. Substantial changes were found in both the transport and structural properties, suggesting they have the same origin – RTA-induced reduction in f_{int}.

Following RTA of the bulk-like GaAsN films, the transport measurements described in Section 4.4 were performed again. As shown in Figure 4.2, following RTA, for $GaAs_{1-x}N_x$ films with x=0.013 and x=0.019, ρ becomes T-independent, suggesting a crossover from electron transport via hopping conduction to that via extended-state band conduction. Furthermore, as shown in Fig. 4.4, with increasing RTA T, n increases substantially and the dependence of n on the measurement T decreases, suggesting that RTA reduces the concentration of the N-induced deep donors. Meanwhile, following RTA, the PPC effect is no longer evident. For as-grown $GaAs_{0.987}N_{0.013}$ films, the illumination induced a > 200% increase in conductivity (i.e. $\frac{g_t - g_d}{g_d}$); following RTA of the $GaAs_{0.987}N_{0.013}$ film, the illumination-induced increase in conductivity is only ~13%.

Prior to this dissertation work, direct evidence for the influence of RTA on f_{int} in GaAsN was limited to single data points in two literature reports.[11, 12] In this dissertation work, f_{int} of GaAsN films pre- and post-RTA were systematically investigated using NRA measurements. Fig. 4.12 shows a plot of the interstitial N concentration as a function of the total N concentration for a variety of GaAsN films grown at 400 °C. The

black squares are data from previous NRA measurements by M. Reason[50], showing an increase in interstitial N concentration as a function of total N concentration. The blue and red star pairs connected with dash lines are the interstitial N concentrations for GaAsN films before and after RTA, measured by Dr. Wang and the author at the NRA facility at LANL (described in Section 2.7). For as-grown GaAsN films, linear extrapolation of the data suggests ~20% of N incorporated interstitially, as labeled in Fig. 4.12. As shown in Fig. 4.12, following RTA, for $GaAs_{1-x}N_x$ films with x = 0.01 to 0.032, the interstitial N concentrations are reduced, while there is no significant change in the total N concentration.

Room *T* Raman spectra for $GaAs_{0.981}N_{0.019}$:Si before and after annealing are shown in Fig. 4.13. Both spectra reveal features arising from GaAs-like longitudinal-optical (LO) and transverse-optical (TO) phonons from 500 to 580 cm^{-1}, and GaN like LO phonons at 470 cm^{-1}. In addition, we observed Raman features at 410 and 420 cm^{-1}, the intensities of which are significantly suppressed after RTA. These features have been attributed to N interstitial dimers on Ga site $(NN)_{Ga}$ and As site $(NN)_{As}$.[51] In Ref. 17, this assignment was based upon a similarity in the ratio of these frequencies to those of the local vibrational modes (LVMS) of Si_{Ga} and Si_{As}.[52] Since N_2 molecules have the same atomic weight as ^{28}Si, it was assumed that the N_2 molecule would be vibrating as one unit with an increased force constant in comparison with that of Si on Ga or As sites. In this work, we provide the first direct evidence (via NRA) of the annealing-induced reduction in f_{int}, thus proving that these Raman signatures are due to N interstitials.

The annealing-induced increase in n and μ, the reduction in the concentration of electron trapping centers, and the suppression of the PPC effect are all accompanied by a

reduction in f_{int}. Therefore, N interstitials are likely the intrinsic N-related point defect that leads to the "early" onset of MIT, the shrinkage in electron Bohr radius, as well as the free electron trapping and PPC effect in GaAsN alloys.

4.6 Conclusions

In this chapter, we discussed the influence of intrinsic N-related point defects on the electronic properties of GaAsN alloy films. For the as-grown $GaAs_{1-x}N_x$ films, Hall and resistivity measurements reveal an onset of MIT at a much higher n than that in GaAs. The MIT in $GaAs_{1-x}N_x$ is accompanied by a shrinkage of a_B with increasing x, suggesting an x-dependent increase in m_e^*. In addition, T-dependence of n for T>150 K suggests the presence of a N-induced electron trapping level below the GaAsN CB edge. For T<160 K, a N-induced PPC effect is observed. Following RTA, significant increases in n and μ are observed, with a transition in the low T transport mechanism from hopping to extended band conduction. Furthermore, following RTA, the T dependence of n is suppressed and the PPC effect vanishes, suggesting a reduction in the concentration of the N-induced electron traps. Correspondingly, NRA reveals an RTA-induced decrease in f_{int}, and the corresponding signatures for the reduction in f_{int} are also identified in Raman spectra. Thus, it is likely that the N interstitial defects are responsible for the MIT, the shrinkage in Bohr radius, the N-induced trapping level and the PPC effect discussed above. Therefore, the dominant form of intrinsic N defects in GaAsN alloys is likely N interstitials.

4.7 Figures

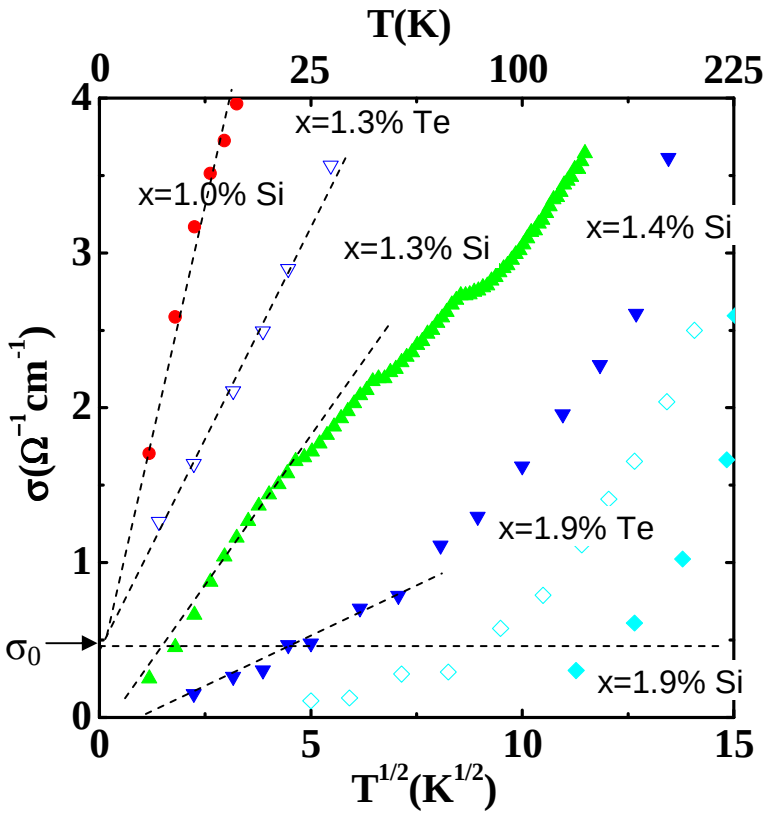

Figure 4.1 Conductivity, σ, as a function of temperature $T^{1/2}$ for GaAsN:Si and GaAsN:Te films, with n= $2x10^{17}cm^{-3}$. The dashed lines are linear-least-square fit of σ measured below 15K according to $\sigma = \sigma_0 + bT^{1/2}$, the y-intercept with x=0 is σ_0. For $GaAs_{0.987}N_{0.013}$:Si, the extrapolation of σ to T=0 passes through origin, thus suggesting a metal-insulator-transition at x=0.013.

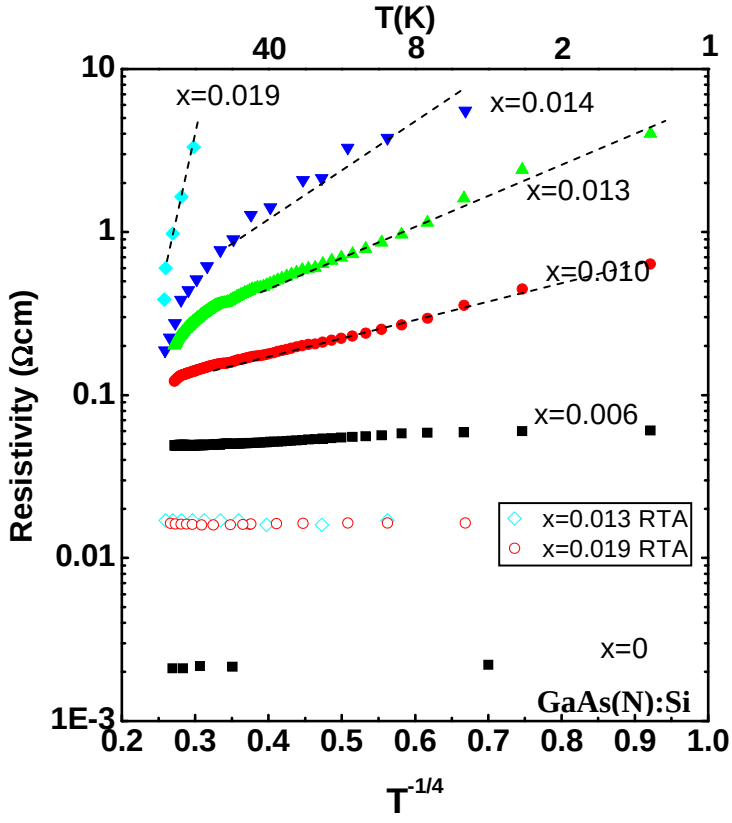

Figure 4.2 Resistivity, ρ, as a function of temperature $T^{-1/4}$ for GaAsN:Si films before and after RTA. For the films with x > 0.013, ρ increases substantially with decreasing T, suggesting the onset of variable range hopping conduction. Following RTA, ρ for GaAsN films become T-independent, suggesting a cross-over from hopping conduction to extended-band conduction.

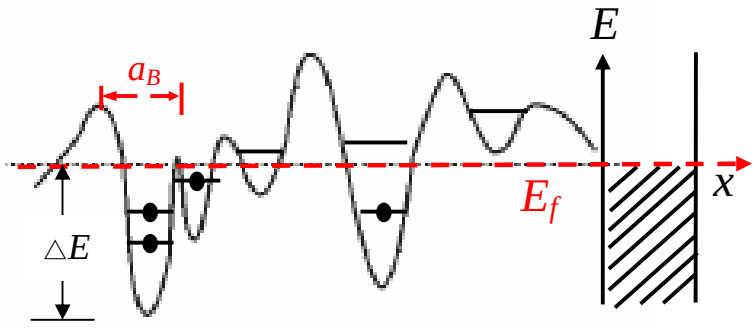

Figure 4.3 Schematic of the N point defect-induced potential fluctuations of the conduction band edge of GaAsN. Carriers are confined in the potential valley with average localization radius, i.e. electron Bohr radius, a_B, and depth, $\triangle E$, labeled on the plot. Carrier conduction is realized by hopping to other localized states.

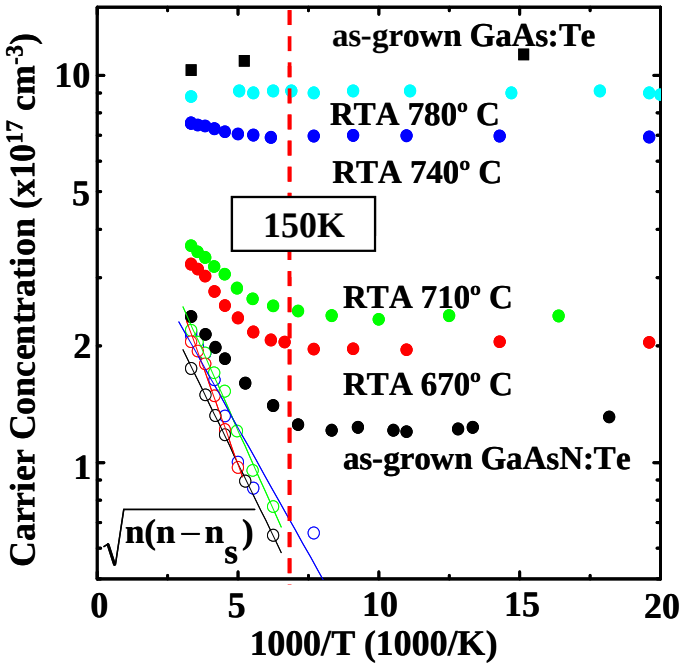

Figure 4.4 Free carrier concentration, n, as a function of inverse temperature for $GaAs_{0.987}N_{0.013}$:Te films annealed at various temperatures. Two distinct T-dependent regimes of [n] are apparent: T>150K, n increases exponentially with increasing T; T< 150K, n is independent of T. To use a 2-level system formalism to extract the activation energy of N-induced deep donor states, $\sqrt{n(n-n_S)}$ is also plotted in open circles for $n>n_s$. Reprinted with permission from Y. Jin *et al.*, Appl. Phys. Lett. **95**, 062109 (2009). Copyright 2009, American Institute of Physics.

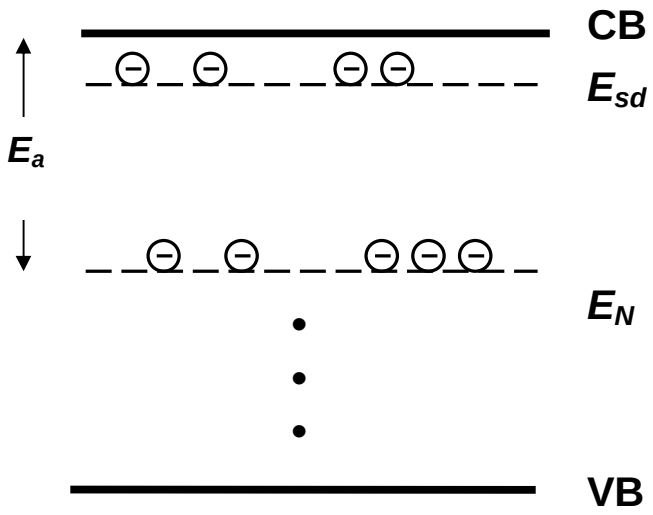

Figure 4.5 Schematic of Si/Te induced shallow donor level, E_{sd}, and N point defect-induced deep donor level, E_N, below the conduction band edge of GaAsN. The shallow donor level is activated at any temperature, while the deep donor level is only activated when T > 150 °C, leading to two temperature-dependent regimes of free carrier concentration in GaAsN.

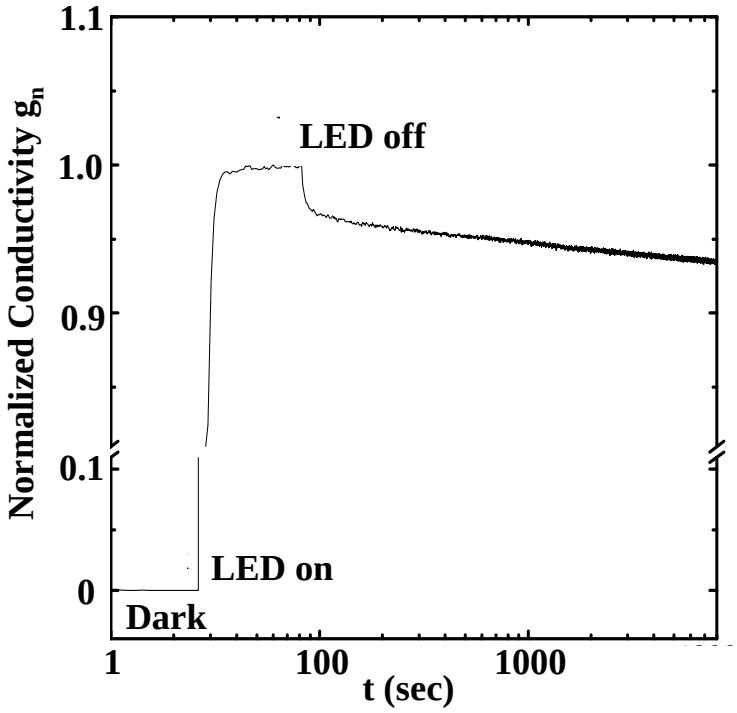

Figure 4.6 An example of normalized conductivity, g_n for a GaAsN film before, during and after illumination with a light-emitting diode (LED), measured at 40K. The moment when the LED is turned on and off are labeled. After illumination is terminated, the decay in g_n is less than 5% in 24 hrs, suggesting the existence of strong persistent photoconductivity. In this case, illumination induced > 200% increase in conductivity (i.e. $\frac{g_t - g_d}{g_d}$), which is not reflected in the figure, since g_d has been normalized to 0 in this figure.

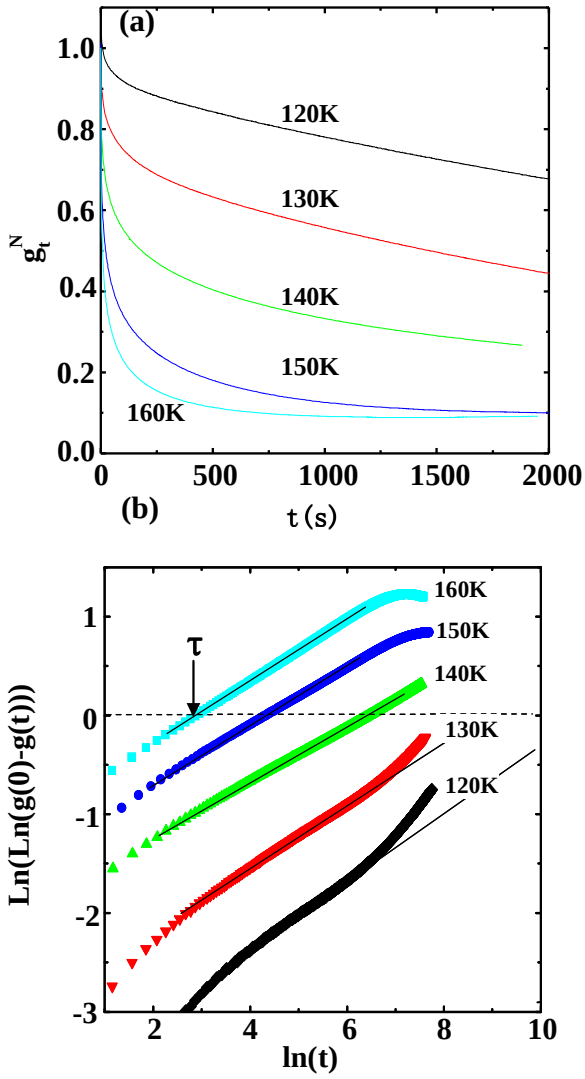

Figure 4.7 An example of persistent photoconductivity data and corresponding analysis for a $GaAs_{0.987}N_{0.013}$:Si film. (a) The normalized conductivity, g_t^N, as a function of time, was measured at various measurement temperatures. (b) Re-plot of g_t^N in the form of a stretched-exponential, $g_t^N = \exp(-(\frac{t}{\tau})^{\beta})$, where the x-intercept at y=0 is identified as the characteristic decay time, τ.

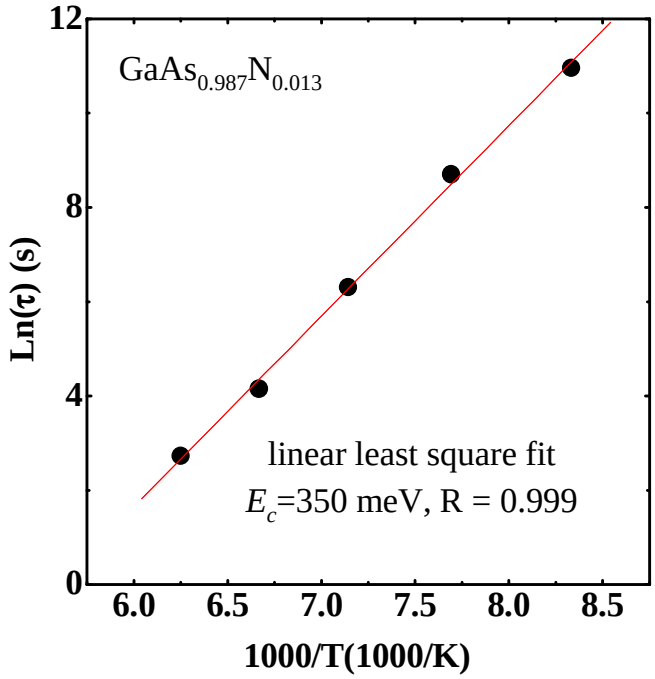

Figure 4.8 A typical example of a plot of characteristic decay time, τ, as a function of inverse measurement temperature. Ln (τ) is linearly dependent on the inverse measurement temperature, suggesting the relaxation of the persistent photoconductivity (PPC) is thermally activated, and the PPC recombination barrier, E_c, is extracted to be 350 meV.

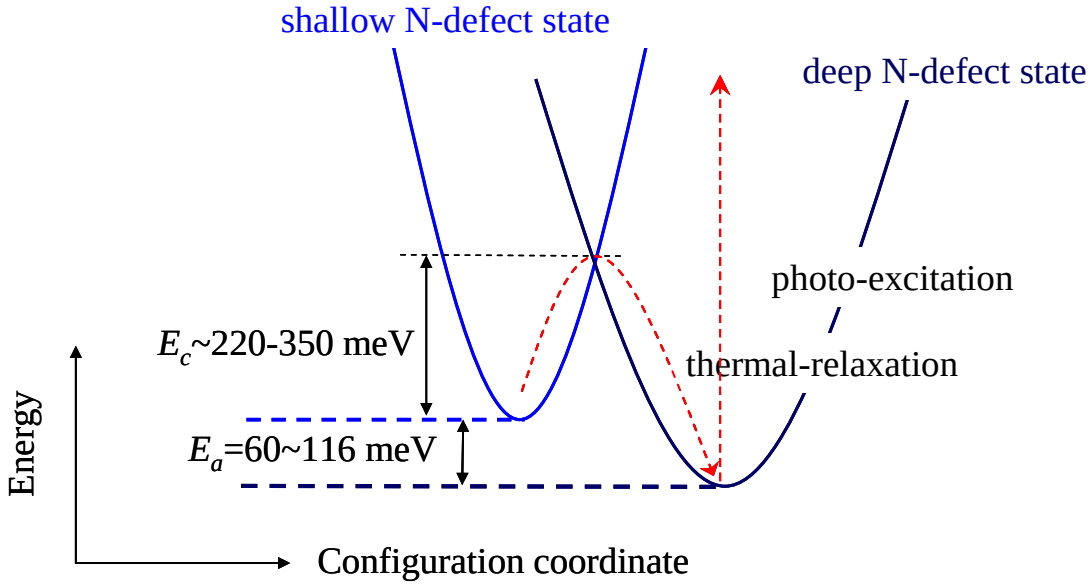

Figure 4.9 Configuration diagram of N interstitial-induced deep and shallow levels in GaAsN. The thermal energy barrier, E_a, was determined from the Hall and resistivity measurements discussed in Section 4.3. The capture barrier, E_c, was determined from the PPC relaxation measurements.

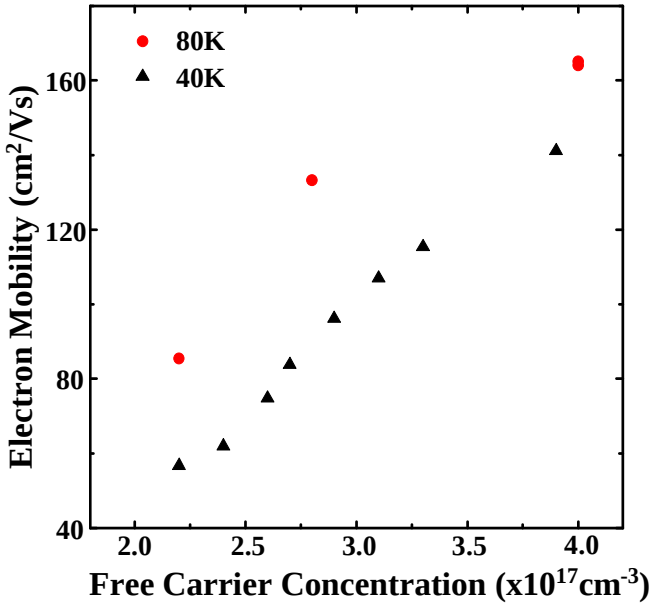

Figure 4.10 Electron mobility, μ, measured as the free carrier concentration, *n*, is gradually increased by illumination. μ increases with *n*, suggesting the existence of N-induced tail of states (or "mobility edge") near the GaAsN conduction band edge, as shown schematically in Fig. 4.11

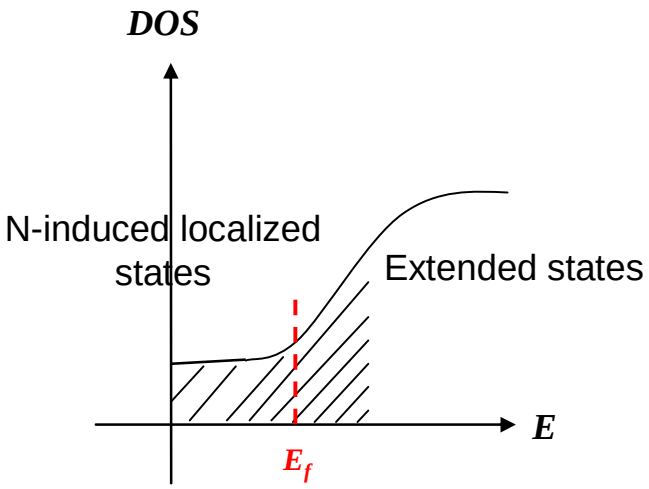

Figure 4.11 Schematic of the density of states (DOS) near the conduction band (CB) edge of GaAsN alloys. Due to the perturbation of the CB induced by the N-induced localized states, the CB edge contains a tail of N-induced localized states, as shown by the shaded area. When the Fermi level is within the shaded area, carrier conduction occurs via variable range hopping. When the Fermi level is in the extended states, band conduction dominates.[44]

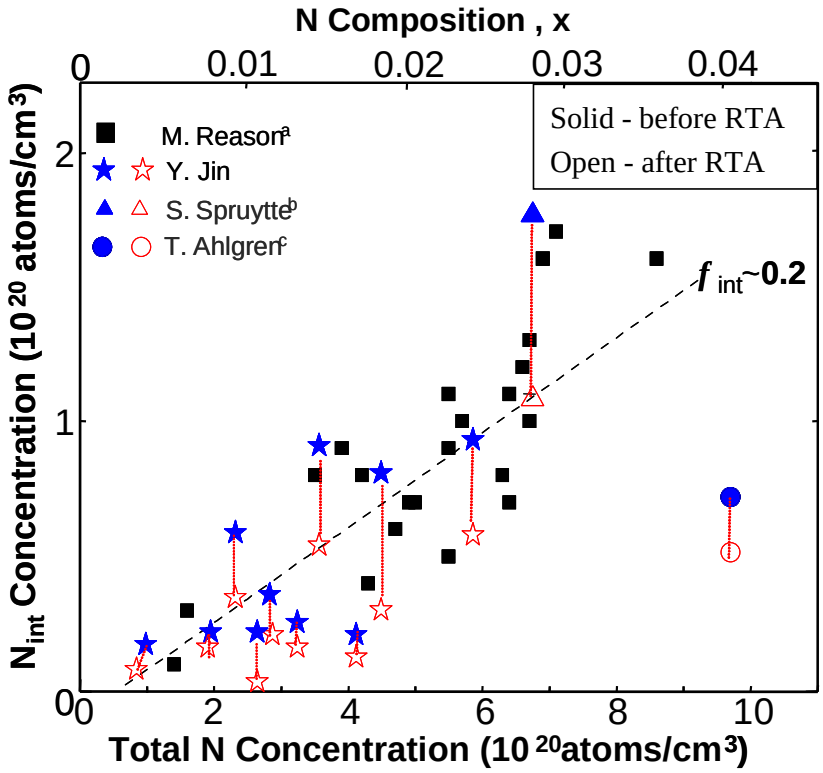

Figure 4.12 Interstitial N concentrations vs. total N concentration for $GaAs_{1-x}N_x$ films grown at 400 °C with varying x. The concentration of interstitial N increases with total N concentration. Linear extrapolation of the data before RTA suggests ~20% of N incorporated interstitially, as indicated in the plot. In addition, interstitial N concentration decreases after annealing, while the total N concentration remains constant. [a] See Ref.[50] [b]See Ref.[11] [c]See Ref.[12].

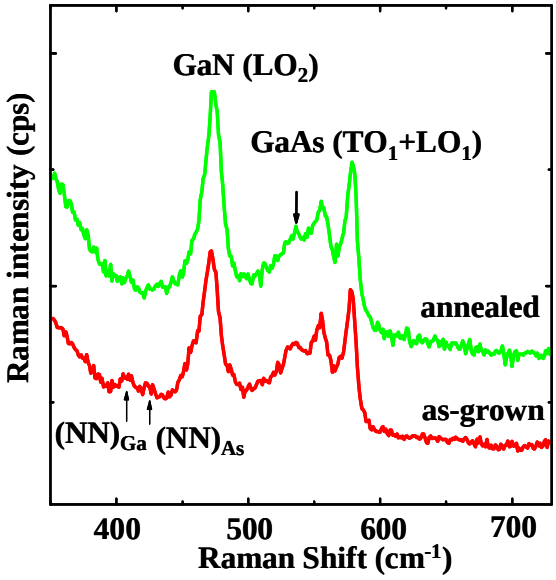

Figure 4.13 Unpolarized Raman spectra of as-grown and annealed $GaAs_{0.981}N_{0.019}$:Si. Both spectra show features arising from second order GaAs-like longitudinal (LO_1) and transverse ($TO_{1)}$ optical phonons from 500 to 580cm^{-1}, and first order GaN like (LO_2) phonons at 470cm^{-1}. In addition, we observed Raman features $(NN)_{Ga}$, and $(NN)_{As}$ at frequencies 410 and 420 cm^{-1}, respectively, the intensities of which are significantly suppressed after annealing. The corresponding reduction in f_{int} observed by NRA suggests these Raman signatures are related to N interstitials. Reprinted with permission from Y. Jin *et al.*, Appl. Phys. Lett. **95**, 062109 (2009). Copyright 2009, American Institute of Physics.

4.8 References

[1]L. H. Li, Z. Pan, W. Zhang, Y. W. Lin, Z. Q. Zhou and R. H. Wu, J. Appl. Phys. **87**, 245 (2000).

[2]M. Ramsteiner, D. S. Jiang, J. S. Harris and K. H. Ploog, Appl. Phys. Lett. **84**, 1859 (2004).

[3]P. Krispin, S. G. Spruytte, J. S. Harris and K. H. Ploog, Physica B **308**, 870 (2001).

[4]J. S. Harris, Semicond Sci Tech **17**, 880 (2002).

[5]K. Volz, V. Gambin, W. Ha, M. A. Wistey, H. Yuen, S. Bank and J. S. Harris, J. Crys. Growth **251**, 360 (2003).

[6]P. Klangtakai, S. Sanorpim, K. Yoodee, W. Ono, F. Nakajima, R. Katayama and K. Onabe, J. Crys. Growth **298**, 140 (2007).

[7]I. A. Buyanova, G. Pozina, P. N. Hai, N. Q. Thinh, J. P. Bergman, W. M. Chen, H. P. Xin and C. W. Tu, Appl. Phys. Lett. **77**, 2325 (2000).

[8]I. A. Buyanova, W. M. Chen and C. W. Tu, Solid State Electron. **47**, 467 (2003).

[9]L. Grenouillet, C. Bru-Chevallier, G. Guillot, P. Gilet, P. Ballet, P. Duvaut, G. Rolland and A. Million, J. Appl. Phys. **91**, 5902 (2002).

[10]J. F. Chen, C. T. Ke, P. C. Hsieh, C. H. Chiang, W. I. Lee and S. C. Lee, J. Appl. Phys. **101**, 123515 (2007).

[11]T. Ahlgren, E. Vainonen-Ahlgren, J. Likonen, W. Li and M. Pessa, Appl. Phys. Lett. **80**, 2314 (2002).

[12]S. G. Spruytte, C. W. Coldren, J. S. Harris, W. Wampler, P. Krispin, K. Ploog and M. C. Larson, J. Appl. Phys. **89**, 4401 (2001).

[13]H. F. Liu, N. Xiang and S. J. Chua, J. Crys. Growth **290**, 24 (2006).

[14]G. Mussler, J. M. Chauveau, A. Trampert, M. Ramsteiner, L. Daweritz and K. H. Ploog, J. Crys. Growth **267**, 60 (2004).

[15]P. Krispin, V. Gambin, J. S. Harris and K. H. Ploog, J. Appl. Phys. **93**, 6095 (2003).

[16]P. Krispin, S. G. Spruytte, J. S. Harris and K. H. Ploog, J. Appl. Phys. **89**, 6294 (2001).

[17]W. K. Loke, S. F. Yoon, S. Z. Wang, T. K. Ng and W. J. Fan, J. Appl. Phys. **91**, 4900 (2002).

[18]B. S. Ma, W. J. Fan, Y. X. Dang, W. K. Cheah and S. F. Yoon, Appl. Phys. Lett. **91**, 041905 (2007).

[19]D. Long and R. J. Hager, J. Appl. Phys. **36**, 3436 (1965).

[20]A. S. skal, Shklovskii, B.I., Sov. Phys. - Solid State **16**, 1190 (1971).

[21]M. C. Maliepaard, M. Pepper, R. Newbury and G. Hill, Phys. Rev. Lett. **61**, 369 (1988).

[22]B. L. Altshuler and A. G. Aronov, Jetp Lett. **37**, 410 (1983).

[23]M. G. Craford, G. E. Stillman, J. A. Rossi and N. Holonyak, Phys. Rev. B **168**, 867 (1968).

[24]D. V. Lang and R. A. Logan, Phys. Rev. Lett. **39**, 635 (1977).

[25]D. V. Lang, R. A. Logan and M. Jaros, Phys. Rev. B **19**, 1015 (1979).

[26]R. F. Khairoutdinov, L. V. Doubova, R. C. Haddon and L. Saraf, J. Phys. Chem. B **108**, 19976 (2004).

[27]X. Y. Lin, K. X. Lin, Z. S. Zhu, R. Huang, Y. P. Yu and Y. L. Luo, Conference Record of the 2006 IEEE 4th World Conference on Photovoltaic Energy Conversion, Vols 1 and 2 1692 (2006).

[28]A. Y. Polyakov, N. B. Smirnov, A. V. Govorkov, N. V. Pashkova, A. A. Shlensky, S. J. Pearton, M. E. Overberg, C. R. Abernathy, J. M. Zavada and R. G. Wilson, J. Appl. Phys. **93**, 5388 (2003).

[29]J. Lyou, K. S. Yoon, E. K. Kim and S. K. Min, Thin Solid Films **358**, 259 (2000).

[30]M. G. Craford, G. E. Stillman, N. Holonyak and J. A. Rossi, J. Electron. Mater. **20**, 3 (1991).

[31]M. I. Nathan, Solid State Electron. **29**, 167 (1986).

[32]H. P. Wei, D. C. Tsui and M. Razeghi, Appl. Phys. Lett. **45**, 666 (1984).

[33]M. I. Nathan, M. Heiblum, J. Klem and H. Morkoc, J. Vac. Sci. Technol. B **2**, 167 (1984).

[34]M. K. Sheinkman and A. Y. Shik, Sov. Phys. Semicon. **10**, 128 (1976).

[35]A. S. Dissanayake, J. Y. Lin and H. X. Jiang, Phys. Rev. B **48**, 8145 (1993).

[36]J. Y. Lin and H. X. Jiang, Phys. Rev. B **41**, 5178 (1990).

[37]K. Ploog and G. H. Dohler, Adv. Phys. **32**, 285 (1983).

[38]M. Hundhausen, L. Ley and R. Carius, Phys. Rev. Lett. **53**, 1598 (1984).

[39]D. J. Chadi and K. J. Chang, Phys. Rev. B **39**, 10063 (1989).

[40]D. J. Chadi and K. J. Chang, Phys. Rev. Lett. **61**, 873 (1988).

[41]J. Z. Li, J. Y. Lin, H. X. Jiang, J. F. Geisz and S. R. Kurtz, Appl. Phys. Lett. **75**, 1899 (1999).

[42]S. H. Hsu, Y. K. Su, R. W. Chuang, S. J. Chang, W. C. Chen and W. R. Chen, Jpn. J. Appl. Phys. 1 **44**, 2454 (2005).

[43]S. H. Hsu, W. R. Chen, Y. K. Su, R. W. Chuang, S. J. Chang and W. C. Chen, J. Crys. Growth **290**, 87 (2006).

[44]B. I. Shklovskii and A. L. Efros, *Electronic properties of doped semiconductors* (Springer-Verlag Berlin Heidelberg New York Tokyo, 1984)

[45]F. Masia, G. Pettinari, A. Polimeni, M. Felici, A. Miriametro, M. Capizzi, A. Lindsay, S. B. Healy, E. P. O'Reilly, A. Cristofoli, G. Bais, M. Piccin, S. Rubini, F. Martelli, A. Franciosi, P. J. Klar, K. Volz and W. Stolz, Phys. Rev. B **73**, 073201 (2006).

[46]E. P. O'Reilly, A. Lindsay and S. Fahy, J. Phys-Condense Mat. **16**, S3257 (2004).

[47]E. F. Schubert, *Doping in III-V semiconductors* (Cambridge Universtiy Press, UK, 1993) pp. 354-365.

[48]E. F. Schubert, *Doping in III-V semiconductors* (Cambridge Universtiy Press, UK, 1993) pp. 193-207.

[49]C. H. Lee, G. Yu and A. J. Heeger, Phys. Rev. B **47**, 15543 (1993).

[50]M. Reason, H. A. McKay, W. Ye, S. Hanson, R. S. Goldman and V. Rotberg, Appl. Phys. Lett. **85**, 1692 (2004).

[51]M. Ramsteiner, D. S. Jiang, J. S. Harris and K. H. Ploog, Applied Physics Letters **84**, 1859-1861 (2004).

[52]W. M. Theis and W. G. Spitzer, J. Appl. Phys. **56**, 890 (1984).

CHAPTER 5

SUMMARY AND SUGGESTIONS FOR FUTURE WORK

5.1 Overview

In this dissertation work, we have studied the influence of N-induced point defects on the electronic and optical properties of InGaAsN alloys.

The presence of extrinsic N-related point defect, namely Si-N complexes, is suggested by a decrease in carrier concentration, *n*, with increasing N-composition, x, observed in GaAsN:Si films but not in modulation-doped heterostructures. In addition, for GaAsN:Te (GaAsN:Si), *n* increases substantially (minimally) with annealing-*T*, suggesting a competition between annealing-induced Si-N complex formation and a reduced concentration of N-related traps. Since Si-N complex formation is enhanced for GaAsN:Si growth with the (2 x 4) reconstruction, which has limited group V sites for As-N exchange, the $(Si\text{-}N)_{As}$ interstitial pair is identified as the dominant Si-N complex. Finally, modulation-doped GaAs(N)/AlGaAs heterostructures were utilized to study N-related carrier scattering mechanisms without the influence of Si-N defect complexes, and the dominant source of carrier scattering was identified to be neutral scatters, such as N interstitial related point defects.

For intrinsic N-related defects, we compared the electronic properties of GaAsN films before and after rapid thermal annealing (RTA). We observed four effects in as-

grown GaAsN films that are either removed or reduced after RTA, likely due to the RTA-induced reduction of the interstitial N fraction, f_{int}. First, for as-grown GaAsN films, Hall and resistivity measurements reveal the onset of a metal-insulator transition (MIT), at a much higher n than that in GaAs. The MIT in GaAsN is accompanied by a shrinkage of the electron Bohr radius with increasing x, suggesting an increase in electron effective mass for GaAsN in comparison with that of GaAs. In addition, the temperature-dependence of n for T>150K suggests the presence of a N-induced electron trapping level below the GaAsN CB edge, which is accompanied by a persistent photoconductivity (PPC) effect. After RTA, significant increases in n and μ are observed, and a transition occurs in the low T transport mechanism from hopping to extended band conduction. Furthermore, after RTA, the temperature-dependence of n is suppressed and the PPC effect vanishes, suggesting a reduction in the concentration of the N-induced electron traps. Interestingly, NRA reveals an RTA-induced decrease in f_{int}, and the corresponding signatures for the reduction in f_{int} are also identified in Raman spectra. Thus, it is likely that N interstitials are responsible for the MIT, the shrinkage in electron Bohr radius, the N-induced trapping level, and the PPC effect discussed above. Indeed, N interstitial defects are likely the dominant form of intrinsic N defects in GaAsN alloys.

Several suggestions are made for future work, as follows.

5.2 Atomic structure of Si-N defect complexes

In chapter 3, by comparing the structure and properties of GaAsN films grown with different surface reconstructions, we indirectly identified interstitial $(Si\text{-}N)_{As}$ pairs as the more energy favorable Si-N defect complex. To directly determine the atomic structure of Si-N defect complexes in bulk-like GaAsN, cross-section scanning tunneling microscopy (XSTM) investigations of GaAsN:Si and GaAs:Si bulk-like films with various Si doping concentrations and annealing conditions are suggested. In XSTM, a cross-section of an (001)-oriented layered structure is prepared by cleaving the structure in ultra-high vacuum (UHV), to expose an atomically flat [1] surface, and constant-current scanning tunneling microscopy (STM) is then performed on this cleaved surface. Information about the chemistry and electronic properties of the bulk-like layers can thus be obtained.[2, 3]

The atomic structure of Si-related defects in GaAs has been investigated using STM, XSTM, and scanning tunneling spectroscopy (STS).[4-13] In addition, STM has also been used to identify N-related defects in GaAsN.[3, 14-17] To help identify the features observed in XSTM and attribute them to particular atomic configurations, calculations of the electronic features of point defects, such as potential profiles and electronic density of states are needed.[4, 18-21] To distinguish features associated with substitutional $Si_{Ga}\text{-}N_{As}$ and interstitial $(Si\text{-}N)_{As}$ pairs, ab initio simulations should be performed in parallel with XSTM experiment.[2]

5.3 Identification of N-induced defect states

In chapter 3, the carrier scattering/trapping in GaAsN without the influence of Si-

N defect complexes was investigated using modulation-doped GaAs(N)/AlGaAs 2DEG heterostructures. From those measurements, N-induced neutral scattering was identified as the dominant source of scattering in GaAsN alloys. However, due to the built-in (or external) electric field in this heterostructure, there exists a potential gradient in the 2DEG layer, and the Fermi energy is essentially interacting with a range of N-related energy levels. Thus, it is not possible to distinguish the influences from individual N-induced energy levels.

Here, we propose a "narrow 2DEG" heterostructure, that can potentially be used to identify the location of individual N-induced defect level(s) near the GaAs CB edge. In this heterostructure, the dilute nitride layer would be thick enough that bulk properties would still apply, but thin enough that the N states are not affected by the potential gradient. As shown in Fig. 5.1, the narrow-2DEG heterostructure is similar to the conventional AlGaAs/GaAs 2DEG heterostructure, with a very thin (~2 nm) δ-like GaAsN layer located near the 2DEG interface. Fig. 5.2 shows the CB diagram for the narrow-2DEG modulation-doped heterostructure, simulated by 1D Poisson/Schrödinger simulation software.[22, 23] In principle, it is possible to manipulate the Fermi level position relative to the CB edge of the GaAsN layer by applying a front gate voltage. Thus, as the Fermi level moves to coincide with the energies of the N-induced defect states, which presumably scatter free carriers, valleys in the conductivity are expected.[24] For the structure shown in Fig. 5.1, the application of a front gate voltage from -80 to 400 mV is expected to lead to ± 3 meV variations the Fermi level relative to the GaAsN CB edge.

5.4 Distinguishing $(NN)_{As}$ and $(NAs)_{As}$ split interstitials

In chapter 4, a combination of nuclear reaction analysis (NRA) and Rutherford backscattering spectrometry (RBS) in channeling and non-channeling conditions was used to determine the total and interstitial N concentration in (In)GaAsN films. Significant composition-dependent f_{int} were revealed, and RTA was found to substantially reduce f_{int}.

To distinguish between $(NN)_{As}$ and $(NAs)_{As}$ split interstitials, and determine the dominant defect for higher N compositions, NRA studies utilizing [111] channeling are suggested. As shown schematically in Fig. 5.3, for the $(NN)_{As}$ split interstitial complex, electronic structure calculations predict that the N atoms within the $(NN)_{As}$ complex reside in the [111] channel, with center of mass of the complex on the group V site. On the other hand, for the $(NAs)_{As}$ interstitial complex, calculations have predicted that the N atoms within the $(NAs)_{As}$ complex do not reside in the [111] channel; instead, the As atom is located in the center of the group V site, with the N atom offset by 0.6 Å.[25] Therefore, [111] channeling would be useful for distinguishing these two types of N split interstitials.

5.5 Dilute bismide GaAsNBi alloys

As a follow up to these studies of dilute nitride alloys, several investigations in the dilute bismide GaAsNBi alloy system are suggested.[26, 27] Specific suggestions include: (a) identification of the optimal GaAsNBi growth temperature window and V/III ratio, (b) mapping out the GaAs(N)Bi band gap as a function of quaternary composition, (c) characterization of hole transport properties in GaAsNBi, and (d) identification of Bi-related defect states near the valence band (VB) edge.

As summarized in Table 1.1 in Chapter 1, N (Bi) atoms have smaller (larger) covalent radius and a larger (smaller) electronegativity than As atoms. As a result, GaBi (GaN) has a larger (smaller) lattice parameter than GaAs. In addition, N and Bi affect the band structure of GaAs in opposite but analogous manners. As discussed in Section 1.3, N incorporation reduces the band gap of GaAs by as much as 150 meV per 1% N, presumably due to the influence of N-induced localized states on the GaAs CB edge. On the other hand, for GaAs:Bi, it has been proposed that Bi incorporation into GaAs also reduces the band gap by as much as 88 meV per 1% Bi,[28, 29] presumably due to the Bi impurity-induced bound state near the VB of GaAs, as shown in Fig. 5.4.[27, 29]

In addition to the Bi-induced band gap reduction, dilute bismide GaAsBi alloys have several additional useful properties. First, the reported temperature-insensitivity of the energy band gap and refractive index make GaAsBi alloys particularly attractive for improving the high-temperature performance of light-emitting device applications.[30, 31] In addition, the Bi composition-dependent VB spin-orbit splitting is expected to enable the manipulation of spins.[32] Furthermore, since the CBM of GaAsBi and the VBM of GaAsN are approximately aligned with those of GaAs, with corresponding significant VB and CB offsets, GaAsN/GaAsBi is expected to exhibit a Type II band-offset, as shown in Fig. 5.5. The resulting optical absorption at wavelengths smaller than the fundamental band gap and the spatial separation of charge are both promising for intermediate band solar cells.[33, 34] Finally, Bi has the lowest toxicity among the neighboring elements, such as As, Sb, Hg, Th and Pb.[29]

The co-incorporation of N and Bi in GaAsNBi alloys offers several advantages. First, due to the large atomic radius of Bi, simultaneous incorporation of Bi and N can

eliminate the strain inherent to the dilute nitrides nearly lattice-matched to GaAs.[35] In addition, calculations have suggested that Bi-N nearest neighbors would form a dipole, thereby reducing free electron and free hole scattering; to date, this has not been confirmed experimentally.[35] In addition, there is some experimental evidence that the GaAs band gap reduction due to the combination of Bi and N is larger than the sum of the two independently, while it is the opposite for In and N in GaAs.[36] For example, as schematically shown in Fig. 1.1, to achieve alloys lattice matched to GaAs with E_g = 0.93eV (which corresponds to λ =1.33 μm), the N and In/Bi compositions needed for InGaAsN and GaAsNBi are: 3.8% N, 10% In, and 1.5% N, 2.4% Bi, respectively.[27, 29] Thus, an equivalent band gap reduction can be achieved in GaAsNBi with significantly less N incorporation compared to that of InGaAsN. Thus, it should be possible to obtain GaAsNBi–based 1.0 eV bandgap material with much longer carrier diffusion lengths (as discussed in Section 1.5) than have been reported for In GaAsN.[37]

5.6 Figures

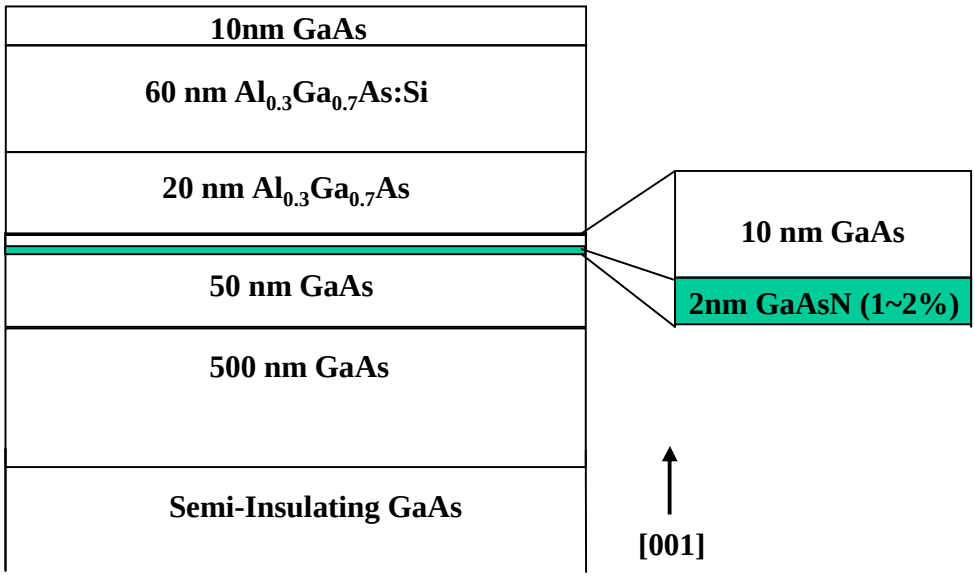

Figure 5.1 Cross-section of a narrow-2DEG modulation-doped heterostructure consisting of a 50 nm thick GaAs channel layer, 20 nm undoped $Al_{0.3}Ga_{0.7}As$, 60 nm Si-doped $Al_{0.3}Ga_{0.7}As$, and 10 nm GaAs grown by solid source molecular beam epitaxy. A 2 nm thick GaAsN layer is inserted in the GaAs channel layer ~10 nm away from the GaAs/AlGaAs interface. The whole structure is grown on top of 500 nm undoped GaAs buffer layer grown at 580 ˚C.

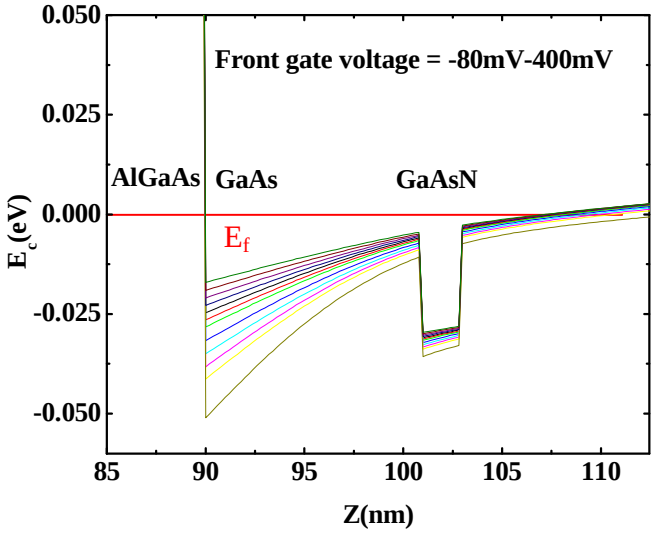

Figure 5.2 CB diagram for the narrow-2DEG modulation doped heterostructures calculated with 1D Poisson/Schrödinger software. [22, 23, 38] As the front gate voltage is swept from -80 to 400 mV, the relative position of Fermi level to the GaAsN CB edge is varied by ± 3 meV

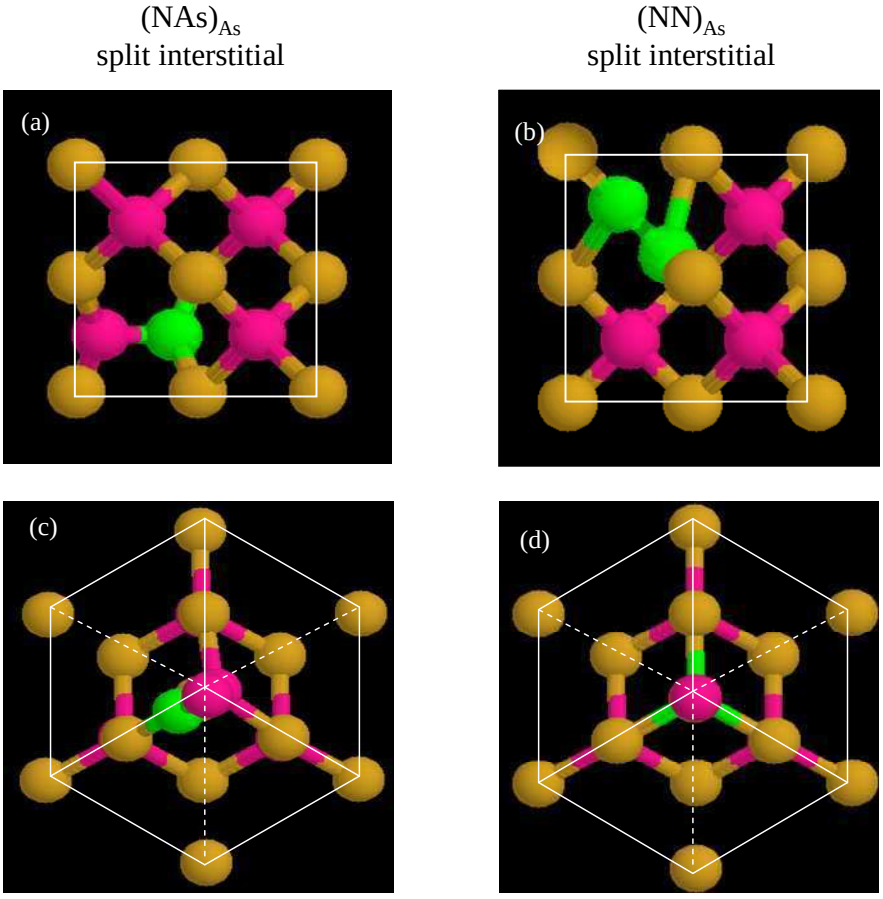

Figure 5.3 Schematic ball-stick models of $(NN)_{As}$ and $(NAs)_{As}$ split interstitials in GaAs lattice for (a) (b) [001] channeling and (c) (d) [111] channeling. For [001] channeling, both interstitials will be detected. For [111] channeling only $(NAs)_{As}$ will be detected. Thus, [111] channeling is expected to be useful for distinguishing $(NN)_{As}$ and $(NAs)_{As}$ split interstitials.

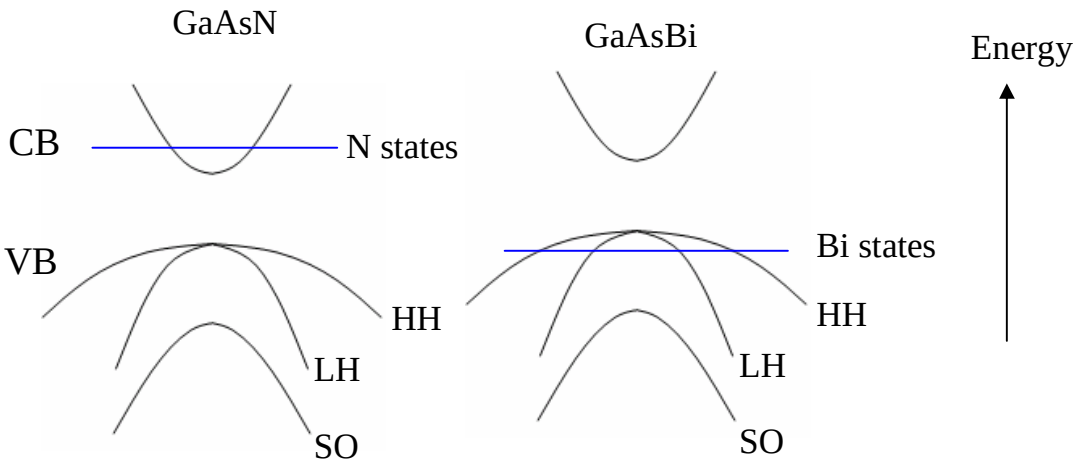

Figure 5.4 Schematic illustration of band structure of : (a) GaAsN and (b) GaAsBi, showing CB, heavy hole VB (HH), light hole VB (LH) and split-off band (SO). N(Bi) incorporation primarily affects the conduction (valence) band of GaAs.[27, 29]

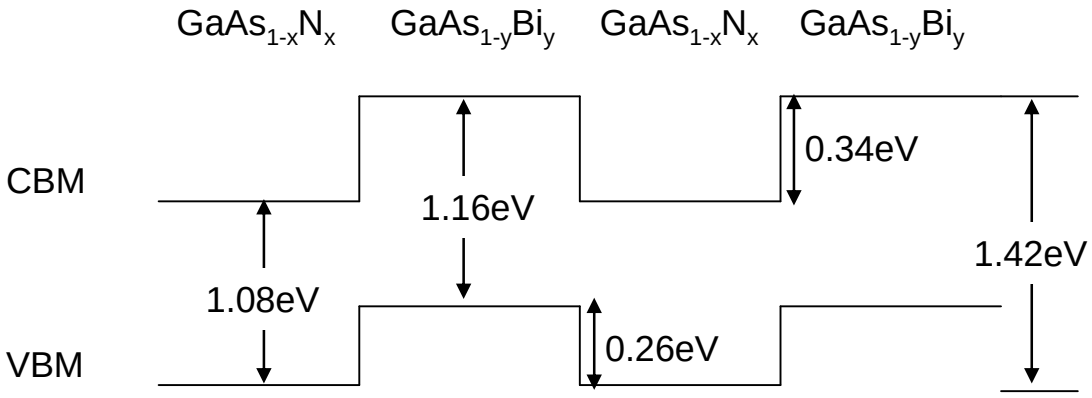

Figure 5.5 Schematic band alignment for a $GaAs_{1-x}N_x/GaAs_{1-y}Bi_y$ superlattice structure with x=y = 0.03.[29] The modification of Bi (N) to the valence (conduction) bandedge of GaAs enables the growth of heterostructures with type II band alignment.[33]

5.7 References

[1]C. L. Aardahl, H. K. Yun, T. P. Pearsall, J. W. Rogers, M. Qian, H. Fong and M. Sarikaya, Thin Solid Films **344**, 646 (1999).

[2]L. Bogdan, Ph.D. thesis, Ch. 2. University of Michigan, 2001

[3]R. S. Goldman, J. Phys. D-Appl. Phys. **37**, R163 (2004).

[4]X. M. Duan, M. Peressi and S. Baroni, Phys. Rev. B **72**, 085341 (2005).

[5]M. D. Pashley and K. W. Haberern, Phys. Rev. Lett. **67**, 2697 (1991).

[6]B. Grandidier, D. Stievenard, J. P. Nys and X. Wallart, Appl. Phys. Lett. **72**, 2454 (1998).

[7]C. Domke, P. Ebert and K. Urban, Surf. Sci. **415**, 285 (1998).

[8]J. Gebauer, R. Krause-Rehberg, C. Domke, P. Ebert and K. Urban, Mater. Sci. Forum **258-2**, 885 (1997).

[9]C. Domke, P. Ebert and K. Urban, Phys. Rev. B **57**, 4482 (1998).

[10]J. Gebauer, R. Krause-Rehberg, C. Domke, P. Ebert and K. Urban, Positron Annihilation - Icpa-11 - Proceedings of the 11th International Conference on Positron Annihilation, Kansas City, Missouri, USA, May 1997 **255-2**, 494 (1997).

[11]Y. Ishikawa, T. Fukui and H. Hasegawa, J. Vac. Sci. Technol. B **15**, 1163 (1997).

[12]H. Yamaguchi and Y. Horikoshi, Phys. Rev. B **53**, 4565 (1996).

[13]M. D. Pashley, K. W. Haberern and R. M. Feenstra, J. Vac. Sci. Technol. B **10**, 1874 (1992).

[14]J. M. Ulloa, P. M. Koenraad and M. Hopkinson, Appl. Phys. Lett. **93**, 083103 (2008).

[15]W. M. McGee, P. A. Bone, R. S. Williams and T. S. Jones, Appl. Phys. Lett. **87**, 181905 (2005).

[16]H. A. McKay, R. M. Feenstra, T. Schmidtling, U. W. Pohl and J. F. Geisz, J. Vac. Sci. Technol. B **19**, 1644 (2001).

[17]R. S. Goldman, R. M. Feenstra, B. G. Briner, M. L. Osteen and R. J. Hauenstein, J. Electron. Mater. **26**, 1342 (1997).

[18]R. M. Feenstra, Phys. Rev. B **50**, 4561 (1994).

[19]P. Ebert, Surf. Sci. Rep. **33**, 121 (1999).

[20]N. D. Jager, M. Marso, M. Salmeron, E. R. Weber, K. Urban and P. Ebert, Phys. Rev. B **67**, 165307 (2003).

[21]S. Modesti, R. Duca, P. Finetti, G. Ceballos, M. Piccin, S. Rubini and A. Franciosi, Phys. Rev. Lett. **92**, 086104 (2004).

[22]I. H. Tan, G. L. Snider, L. D. Chang and E. L. Hu, J. Appl. Phys. **68**, 4071 (1990).

[23]1D Poisson/Schrodinger, Greg Snider, U-Notre Dame; www.nd.edu/~gsnider; downloaded 10:47pm (January 24, 2010)

[24]private communication with Fahy *et al*

[25]E. Arola, J. Ojanen, H.-P. Komsa and T. T. Rantala, Phys. Rev. B **72**, 045222 (2005).

[26]B. Fluegel, A. Mascarenhas, A. J. Ptak, S. Tixier, E. C. Young and T. Tiedje, Physical Review B **76**, (2007).

[27]S. Tixier, S. E. Webster, E. C. Young, T. Tiedje, S. Francoeur, A. Mascarenhas, P. Wei and F. Schiettekatte, Appl. Phys. Lett. **86**, 112113 (2005).

[28]S. Francoeur, M. J. Seong, A. Mascarenhas, S. Tixier, M. Adamcyk and T. Tiedje, Appl. Phys. Lett. **82**, 3874 (2003).

[29]T. Tiedje, E. C. Young and A. Mascarenhas, Int. J. Nanotechnol. **5**, 963 (2008).

[30]M. Yoshimoto, W. Huang, G. Feng and K. Oe, Phys. Status Solidi B **243**, 1421 (2006).

[31]J. Yoshida, T. Kita, O. Wada and K. Oe, Jpn. J. Appl. Phys. 1 **42**, 371 (2003).

[32]B. Fluegel, S. Francoeur, A. Mascarenhas, S. Tixier, E. C. Young and T. Tiedje, Phys. Rev. Lett. **97**, 067205 (2006).

[33]M. Y. Levy, C. Honsberg, A. Marti and A. Luque, IEEE Phot. Spec. Conf. 90 (2005).

[34]Y. Zhang, A. Mascarenhas and L. W. Wang, Phys. Rev. B **71**, 155201 (2005).

[35]A. Mascarenhas, Y. Zhang, J. Verley and M. J. Seong, Superlattices Microstruct. **29**, 395 (2001).

[36]S. Adachi, *Physical Properties of III-V semiconductor Compounds* (Wiley, West Sussex, England, 1992)

[37]T. Tiedje, E. C. Young and A. Mascarenhas, International Journal of Nanotechnology **5**, 963-983 (2008).

[38]G. L. Snider, I. H. Tan and E. L. Hu, J. Appl. Phys. **68**, 2849 (1990).

APPENDIX A

Growth and characterization of GaAs:Te

Since GaTe was introduced for the first time as an n-type doping source in our GenII MBE system, a series of calibration growths were performed. GaAs:Te films were grown with various growth temperatures, growth rates, and GaTe cell temperatures. The well-calibrated Si-doped GaAs films were used as a reference to compare with the doping behavior of GaTe. All films grown for GaTe source calibration purposes are summarized in Table A.3; select data is also plotted in Fig.A.3

First, the effect of Te surface segregation on the surface morphology of GaAs:Te films was examined. During the growth of the GaAs buffer layer at 580 °C, a streaky (2x4) surface reconstruction was observed (Fig.A.1(a), (b)). As soon as the GaTe shutter was opened, the RHEED intensity decreased, and the RHEED pattern became slightly spotty (Fig.A.1 (c), (d)). With increasing film thickness, the RHEED intensity decreased further, and the RHEED pattern became spotty, suggesting an increase in surface roughness. After growth, AFM images were collected from the GaAs:Te surface, as shown in Fig.A.2. Mound-like features elongated in the $[1\bar{1}0]$ were observed, with 1.3 nm rms surface roughness instead of the 0.3~0.4 nm rms roughness typically observed for GaAs(:Si) films grown with similar V/III ratios and substrate temperatures.

The effect of Te surface segregation on the electronic properties of GaAs:Te was then examined. In Fig. A.3, Log (*n*) of GaAs:Te films are plotted as a function of inverse GaTe cell temperature, with GaTe doping calibration values reported by Bennett *et al.*[1] included as well. The dashed line is linear-least-square fit to the combination of Bennett's data and our 2007 doping calibration data. Log(*n*) depends linearly on the inverse GaTe cell temperature, suggesting *n* is thermally activated, with an activation energy =1.82 eV, consistent with literature reports.[1] For GaAs:Si films grown with the same Si effusion cell settings, similar *n* values are measured, independent of growth temperature (400 vs. 580 °C). However, for GaAs:Te, for the same effusion cell setting, films grown at 580 °C exhibited significantly lower *n* than those films grown at 400 °C (Fig.A.3), presumably due to Te surface segregation at the higher substrate temperature. Furthermore, for both GaAs:Si and GaAs:Te films grown at 400 °C, *n* increases with decreasing growth rates (Table.A.1), as predicted based upon beam flux ratio analysis.[2] On the other hand, for GaAs:Te films grown at 580 °C, *n* is higher for films grown at higher growth rates. This is presumably because lower growth rates allow more time for Te surface segregation, thus further lowering the doping efficiency.[1] However, GaAsN films are typically grown at 400 °C, where Te surface segregation is presumably negligible.[1] Therefore, GaTe is suitable as an alternative n-type dopant for GaAs.

Finally, two issues are important for the long-term use of GaTe as an alternative n-doping source in MBE growth, namely, the memory effect and the source stability. To test the GaTe memory effect, after a few growth runs with GaTe doping, we grew an unintentionally doped GaAs sample. Following growth, a background doping concentration less than $1x10^{14}$ cm^{-3} was observed, suggesting that GaTe does not induce a

significant memory effect in our MBE chamber. To test the long-term stability of the cell, Te doping calibration results in a span of two years were compared, as listed in Table A.1 and plotted in Fig.A.3. Compared with the doping calibration performed in 2007, the doping calibration performed recently (2009) yields a much higher free carrier concentration (~5 x higher) for the same GaTe cell temperature. This might be due to the decompostion of GaTe, followed by preferential evaporation of Ga. Therefore, the Te doping cell needs to be frequently calibrated to achieve consistent doping concentrations.

Table A.1: Summary of GaAs:Te and GaAs:Si layers for calibration of the GaTe dopant cell. The free carrier concentration resulting from GaTe doping of GaAs were investigated as a function of GaTe cell temperature, substrate temperature, T_{sub}, and growth rate, in comparison with that of Si doping of GaAs.

	RMBE	G.R.	T_{sub}	Doping cell T(ºC)	n (cm^{-3})	μ (cm^2/Vs)
Influence of T_{sub} on GaAs:Si (Sep. 2007)	579	0.51	400	Si-1265	1.3e18	2318
	580	0.51	580	Si-1265	1.2e18	2271
Influence of T_{sub} on GaAs:Te (Aug.–Sep. 2007)	573	0.50	400	Te-500	2.3e18	1933
	574	0.50	520	Te-500	2.1e18	2193
	575	0.50	550	Te-500	2.0e18	1748
	558	0.52	580	Te-500	2.0e17	3286
Influence of G.R. on GaAs:Te (Aug.2007)	556	0.27	580	Te-480	6.1e16	3980
	555	0.49	580	Te-480	3.4e17	3319
	557	0.94	580	Te-480	9.1e16	4042
Background (Oct.2007)	590	1.07	580	-	-	-
Te Doping calibration (Sep.– Nov.2007)	577	0.51	400	Te-480	7.8e17	2158
	607	0.47	400	Te-490	1.5e18	1987
	573	0.50	400	Te-500	2.3e18	1933
Te Doping calibration (Oct.– Nov. 2009)	725	1.0	400	Te-400	9.0e16	3090
	724	1.0	400	Te-420	2.0e17	2120
	726	1.0	400	Te-450	1.8e18	1780
	711	1.0	400	Te-480	7.0e18	1045
	715	1.0	400	Te-490	7.6e18	1466
	712	1.0	400	Te-500	9.0e18	1287

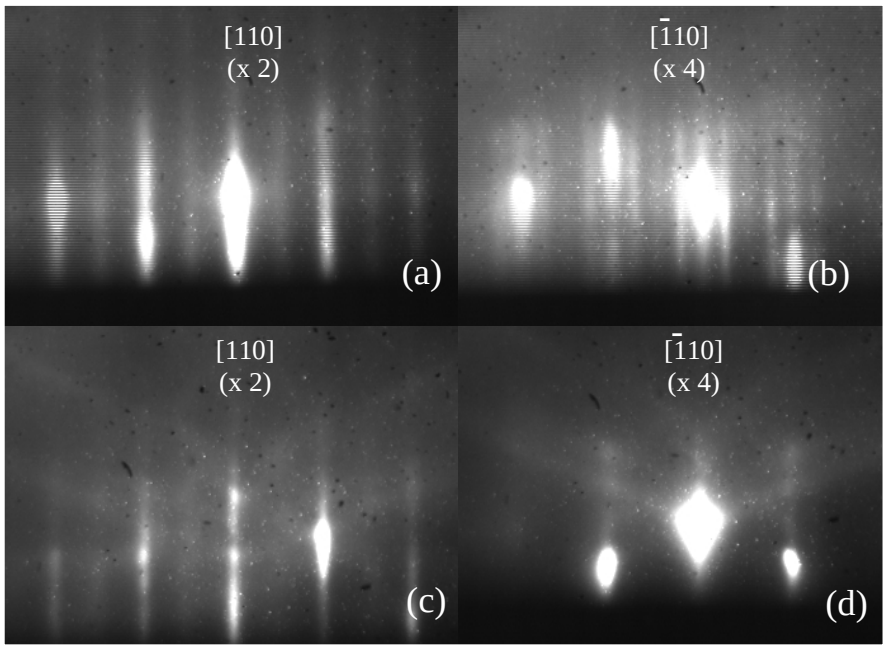

Figure A.1 Reflection high-energy electron diffraction patterns collected along the [110] and [$\bar{1}$10] axes during the growth of (a), (b) GaAs buffer layer, and (c), (d) GaAs:Te layer at 580°C. The streaky (2x4) patterns observed during GaAs buffer growth suggest a layer-by-layer growth mode. The spotty (2x4) patterns observed during GaAs:Te layer growth suggests a transition to 3D growth, presumably due to significant Te surface segregation.

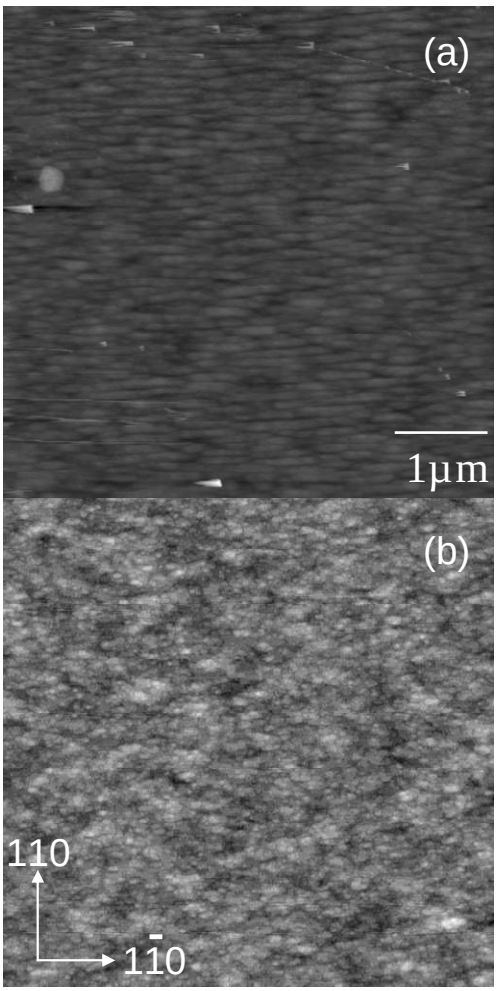

Figure A.2 Representative atomic force microscopy images of GaAs bulk-like films grown at 580ºC (a) with and (b) without Te doping. △Z=10nm in both images. For the Te-doped films in (a), "Mound-like" features elongated along the [1$\bar{1}$0] direction are presumably due to the Te surface segregation at high growth temperature.

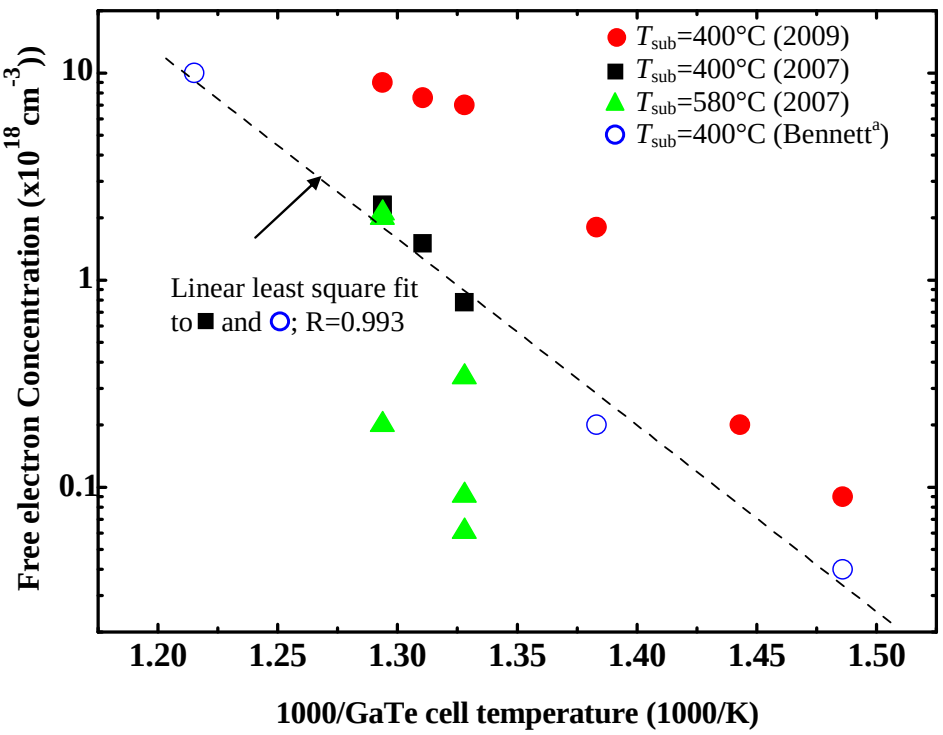

Figure A.3: Free electron concentration, *n*, for GaAs:Te grown at various substrate temperatures, as a function of the inverse GaTe cell temperature. Results from Bennett's GaTe cell doping calibration in GaAs are also included.[1] Log *n* depends linearly on the inverse of the GaTe cell temperature, suggesting that n is thermally activated, with an activation energy of 1.82 eV, similar to literature reports.[1] In addition, significantly lower *n* is observed for films grown at 580°C than those grown at 400°C, presumably due to Te surface segregation. Using equivalent GaTe cell temperatures, the 2009 doping calibration yields substantially higher *n* than those of 2007, presumably due to the decompostion of GaTe, followed by preferential evaporation of Ga.

[1]B. R. Bennett, R. Magno and N. Papanicolaou, J. Crys. Growth **251**, 532 (2003).

[2]E. F. Schubert, *Doping in III-V semiconductors* (Cambridge Universtiy Press, UK, 1993) pp. 354.

APPENDIX B

Ion beam analysis techniques and alignment procedures

B.1 Overview

This Appendix describes the ion beam analysis techniques and alignment procedures used for this dissertation work. In B.2, three NRA measurement setups are described and compared. In B.3, the procedure for aligning the [001] channeling axis in Rutherford backscattering spectrometry (RBS) and nuclear reaction analysis (NRA) is described.

B.2 Comparison of NRA setups at MIBL and LANL

The ion beam analysis measurements were preformed by three people at two laboratories, Michigan ion beam laboratory (MIBL) and Los Alamos National Laboratory (LANL), with slight variations in experimental setups. Thus, it is necessary to compare the difference in the three setups and examine their influences on the ion beam analysis. The differences in the experimental setups are listed in Table B.1.

Table B.1 Differences in configurations of the NRA setup at MIBL and LANL:

	MIBL (original)	MIBL (modified)	LANL
Slits	one (2mm)	one or two (2mm and 4mm)	one slit (3mm x 3mm)
Suppressor	Yes (100V)	no	Yes (150V)
Beam energy	1.4MeV	1.2MeV	1.2MeV
Typical doses	1000 μC	200 μC	12 – 48 μC
Detector	small (5 msr)	small: RBS (5 msr) large: NRA (50 msr)	100msr ($300mm^2$, 5.5cm)
Detector angle	150 º	150 º	135-150 º
Minimal χ_{RBS} obtained	5.7 % (with ^4_2He) on GaAs	~10 % (with ^1_1H) on GaAsN	~4.8 % (with ^1_1H) on GaAsN

Near the beginning of these dissertation studies, a number of changes were made to the MIBL NRA setup. To potentially minimize lattice damage, a larger detector was considered. In addition, in an attempt to improve beam collimation, the slit configuration was modified. Finally, we considered the influences of the incident ion beam energy and the standard sample for RBS measurements on the χ_{RBS}(GaAs) values.

It was suggested that the longer ion beam exposure time needed when using a small detector may induce additional lattice defects and corresponding "extra" de-channeling of the ion beam. Therefore, a large detector was added into the so-called "modified" MIBL setup, as shown in Table B.1. We compared the influence of the detector size on χ_{RBS}. Indeed, lower χ_{RBS} yields were obtained with the larger detector,

especially for $GaAs_{1-x}N_x$ films with low x (<0.005). Therefore, a large-area detector was used for the measurements in this dissertation work.

To accommodate the large-are detector, additional modifications were required. The Faraday cup, which is used to force the sputtered electrons back to the sample, thereby preventing them from being measured as incident positive charge, could not accommodate the new large detector. Therefore, we investigated the necessity of using the Faraday cup. The apparent ion dose was increased by more than 30% when measured without the Faraday cup. Therefore, we installed a new Faraday cup, which could accommodate the large-area detector, and enabled us to accurately measure the incident ion dose.

To potentially improve the ion beam collimation, the slit configuration was modified. Slit(s) are typically put in the beam line in front of the sample to narrow and collimate the ion beam. To examine the influence of slit width, we compared 2 mm and 4 mm width slits and found negligible differences in χ_{RBS}. Then, we compared the use of one slit (4mm in width) vs. two slits (4mm and 2mm in width). We also found that the use of one or two slits lead to negligible differences in the measured χ_{RBS}. In addition, the use of two slits complicated the beam alignment, leading to minimal usable beam current, and a ~ 5-fold increase in the measurement time. Therefore, one slit is suggested for this type of measurement.

Finally, we discuss two other aspects of the “modified” MIBL setup. First, we examined the influence of the incident ion beam energy (1.2MeV vs. 1.4MeV) on χ_{RBS}, and observed negligible difference in the measured χ_{RBS} value. Then, we compared the effect of using GaAs and GaAsN as the control RBS sample. We found that GaAsN films

yield higher χ_{RBS} than GaAs films, which is expected considering the de-channeling due to interstitial N incorporation. Therefore, in this dissertation, GaAs films were used to determine χ_{RBS}(GaAs).

B.3 Aligning to [001] channeling direction

To accurately determine the interstitial N fraction in GaAsN alloy films, it is critical to accurately align the ion beam to the film channeling direction. The details of ion beam analysis experiments were discussed in Section 2.7 and in Section B.6 of M.Reason's PhD thesis.[1] Here we describe the procedure for aligning to the [001] channeling direction in the ion beam analysis setup at LANL.

When energetic ions are incident on a crystal, if they are at or near the direction of the close-packed planes of atoms, they are steered by a series of collisions so that they are "channeled" into the regions between these planes. In this case, the backscattering yield will be significantly lower than when the incident ion beam is in a "random" direction. For example, for the diamond lattice, 4 major and 4 minor plane channeling directions are expected around the [001] direction, as shown in Fig. B.1.[2]

Since our films were grown on [001] substrates, the incident ion beam was initially roughly aligned perpendicular to the sample surface. First, a piece of glass mounted in the vicinity of the sample holder was used to locate the beam spot, a CCD camera was used to record this location, and the sample of interest was then moved to this location. A computer program was used to rotate the goniometer azimuthally about the x and y axes, φ_x and φ_y, (as labeled in Fig. 2.5) in steps of 0.2°. At each 0.2° step, using an incident ion dose of ~0.1 μC, RBS spectra were collected from the top 20-30 channels near the spectra surface edge (as explained in Section 2.7 of this thesis). χ_{RBS} was then calculated and plotted as a function of φ_x and φ_y. As the incident ion beam is aligned to the 4 major and 4 minor plane channeling directions in Fig B.1, 4 "deep" and 4 "shallow" minima in χ_{RBS} are expected. An example of χ_{RBS} vs. step number is shown in

Fig.B.1. A grid was then used to find the [001] channeling direction, as shown in Fig. B.3. The grid was labeled with both the step number and the corresponding φ_x and φ_y rotation angles. Each pair of minima was connected and ideally should intersect at one point, and the corresponding (x,y) coordinate was then identified as the [001] direction. The goniometer was then set to these coordinates and the channeling condition was considered to be established.

B.4 Figures

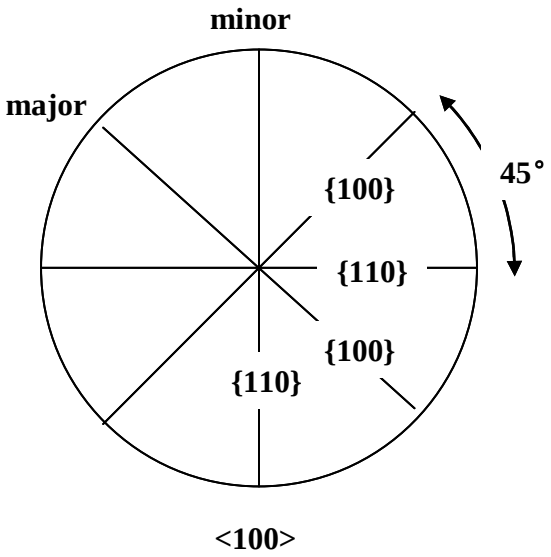

Figure B.1 Low index planes around the <001> axes in a diamond lattice structure. For incident ion beams at or near these "channeling" directions, the backscattering yield exhibits local minima in comparison with the backscattering yield for random directions.[2]

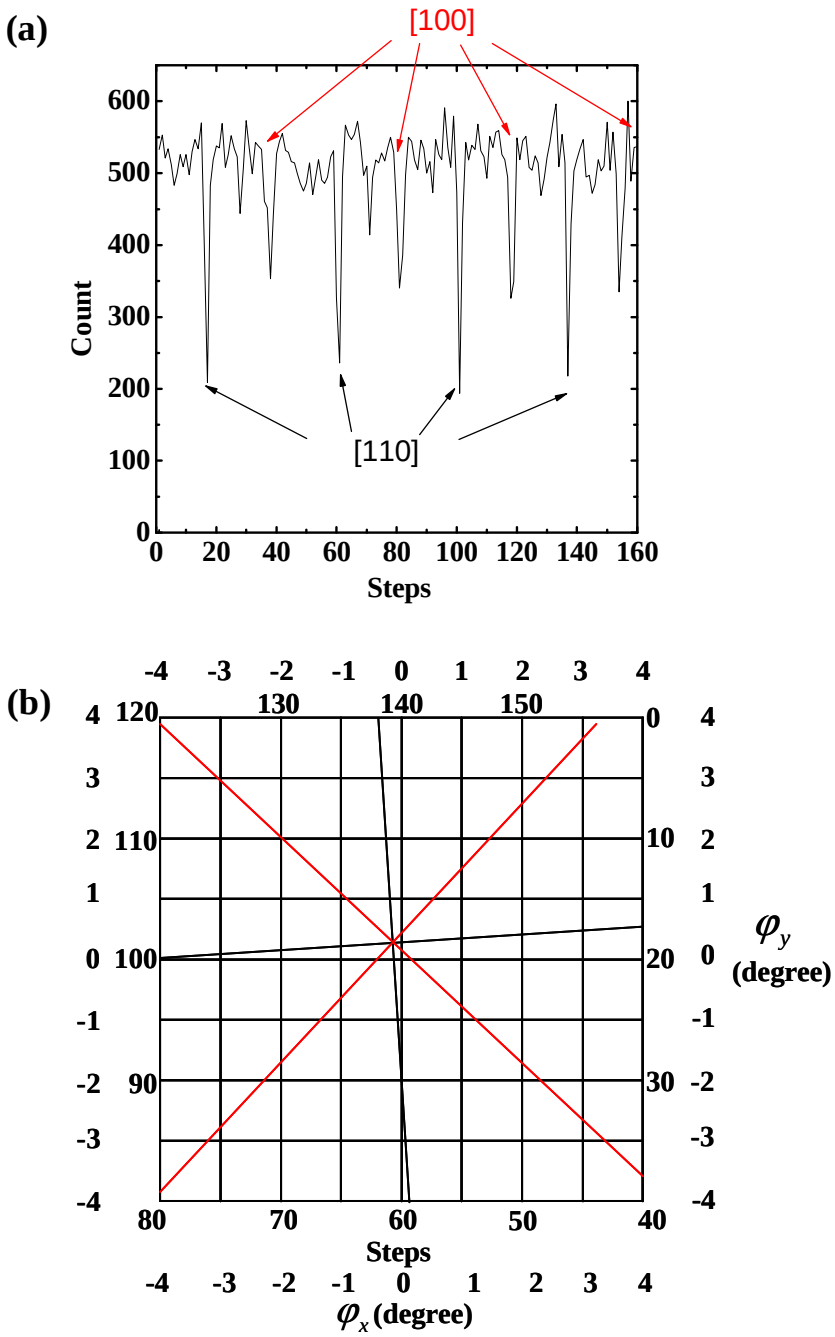

Figure B.2 (a) Example of χ_{RBS} as a function of φ_x and φ_y rotation steps used in the channeling alignment process. (b) The corresponding grid, where pairs of minima in (a) are connected and the point of intersection is considered to be the [001] channeling direction. In both plots, the step numbers are labeled to correspond to φ_x and φ_y rotation angle in degrees.

B.5 References

[1]M. Reason,Ph.D. thesis, University of Michigan, Ch. 2.

[2]J. R. Tesmer and M. A. Nastasi, *Handbook of Modern Ion Beam Materials Analysis* (Materials Research Society, Pittsburgh, 1995) pp. 655.

APPENDIX C

Tabulated data

C.1 Overview

In this Appendix, data from various measurements of GaAs(N) are tabulated. In C.2, data from room *T* Hall and resistivity measurements for n-type GaAsN films are tabulated. In C.3, nuclear reaction analysis data are tabulated.

C.2 Hall and resistivity data

Table C.1: Room *T* free carrier concentration, *n*, free carrier fraction, f_f, (defined as the ratio of n_{GaAsN} to n_{GaAs} with the same target doping concentration) and electron mobility, μ, of GaAsN films with various N composition and Si/Te as the n-type dopant.

GaAsN:Si					GaAsN:Te				
RMBE	x	*n* (x10^{17} cm^{-3})	f_f	μ (cm^2/Vs)	RMBE	x	*n* (x10^{17} cm^{-3})	f_f	μ (cm^2/Vs)
454	0.0002	5.4	1.01	1924	584	0.0075	4.8	0.45	182
446	0.0013	6.5	0.69	595	583	0.010	4	0.38	173
422	0.0025	5.5	0.64	376	578	0.012	2.4	0.31	193
380	0.0035	9.8	0.76	322	596	0.013	5.1	0.36	183
445	0.0048	4.8	0.51	309	559	0.015	7.6	0.34	132
421	0.0068	4.0	0.46	280	576	0.016	1.31	0.17	153
444	0.0082	3.1	0.33	202	598	0.020	2.38	0.17	154
420	0.010	3.1	0.43	250					
427	0.011	7.5	0.58	184					
426	0.012	7.5	0.58	184					
419	0.013	3.4	0.24	209					
378	0.018	3.9	0.31	177					
581	0.019	2.53	0.11	176					
328	0.020	0.6	0.05	157					

C.3 Nuclear reaction analysis data

Table C.2: Nuclear reaction analysis (NRA) data for various $GaAs_{1-x}N_x$ films, including the total N composition determined using x-ray rocking curves and NRA, the ratio of aligned and unaligned yields, $\chi(N)$, and the interstitial N fraction, f_{int}, determined using the expressions described in Section A.1 and A.3 of M. Reason's PhD thesis.[1] Most of the NRA data was obtained at LANL, a described in Section 2.7 and Appendix B.2. Data with * are from previous measurements by M. Reason performed with the "original" MIBL setup described in Appendix B.2.

RMBE	Growth T (°C)		x (XRC)	x (NRA)	$\chi(N)$%	f_{int}%
149	400	as-grown	0.005	0.005/0.007*	21/22*	16.8/28*
		annealed	NA	0.004	15.4	10.9
158	400	as-grown	0.014	0.012/0.019*	19.3/23*	15.1/29*
		annealed	NA	0.013	14.7	10.2
599	400	as-grown	0.019	0.014	13	8.4
		annealed	0.019	0.014	12.5	7.9
683	400	as-grown	0.021	0.020	20	15.8
		annealed	0.021	0.022	10.6	5.9
684	580	as-grown	0.006	0.009	17	12.6
		annealed	0.006	0.009	13.1	8.5
685	400	as-grown	0.018	0.018	8.8	4.0
		annealed	0.017	0.017	8.1	3.3
686	580	as-grown	0.010	0.010	31	28.5
		annealed	0.009	0.010	16	17.1
363	400	as-grown	0.012	0.013	13.3	8.7
		annealed	NA	0.011	7.2	2.3
337	400	as-grown	0.023	0.024	9	4.2
		annealed	NA	0.024	7.6	2.7
327	400	as-grown	0.018	0.020	10.6	5.9
		annealed	NA	0.022	11.3	6.6
365	400	as-grown	0.031	0.030	12.2	7.6
		annealed	NA	0.030	14.4	9.0

C.4 References

[1]M. Reason,Ph.D. thesis, Ch. 2. University of Michigan, 2006

APPENDIX D

Hall bar photolithography process

This Appendix describes the photolithography processes utilized for fabrication of gated Hall bars, including mesa definition, contact definition, and gate definition. The tools used for the processes include the wet chemical bench, the GaAs bay spinner station, the MJB3 Mask aligner, the SJ20 Evaporator, the JetFirst-150 RTP, and Dektak 6M Surface Profilometer

(a) Mesa definition

1. Clean samples with Acetone (Ace), Isopropanol (IPA), DI water; blow dry with N_2
2. Prebake for 10 min at 105 ºC
3. Spin coat Hexamethyldisilazane (HMDS) for 30 s @, 4000 rpm
4. Spin coat photoresist 1813 for 30 s @ 4000 rpm
5. Prebake at 105 ºC for 1 min on hotplate
6. Expose for 6 s in mask aligner
7. Develop with MF351:DI water (1:5) for 1 min
8. Rinse in DI water for 3 min
9. Inspect using UV-filtered light

10. Descum for 1-2 min at 80 W, 250 mTorr, 17% O_2
11. Hard bake: 120ºC for 15 min
12. Mesa etch for 2.5min (GaAs: 1600 Å/min) with H_3PO_4:H_2O_2:H_2O (1:1:25)
13. Strip resist: Ace/IPA/N_2 Dry
14. Measure mesa thickness profile with Dektak

(b) Contact definition

Repeat (a) 1-3

4. Spin coat photoresist 5218 for 30 s @ 4000 rpm
5. Prebake on hotplate at 105 ºC for 1 min
6. Expose for 6 s in mask aligner
7. Bake on hotplate at 120 ºC for 2-4 min
8. Flood expose for 1 min in mask aligner
9. Develop in MIF319 for 1 min
10. Rinse in DI water for 3 min
11. Inspect using UV-filtered light
12. Descum for 1-2 min at 80 W, 250 mTorr, 17% O_2
13. Remove oxide with Ammonium Hydroxide (NH_4OH:H_2O, 1:15) for 15 s
14. N_2 dry only (no DI rinse), place into evaporator immediately
15. Evaporate contacts (Ni/Ge/Au/Ti/Au=200/325/650/200/2000 Å)
16. Liftoff with warm Ace/IPA for 1 min, DI rinse for 1 min
17. Anneal contacts for 2 min at 410 ºC in atmosphere pressure N_2 at Jet first-150 RTP station.

(c) Gate definition

Repeat (b)1-14

15. Evaporate gate (Ti/Au=500/1500 Å)
16. Liftoff with warm Ace, IPA for 1 min, DI rinse for 1 min

APPENDIX E

InGaAsN photodetector Fabrication

E. 1 Overview:

Here, we describe the initial steps towards the fabrication of (In)GaAsN/GaAs p-i-n photodetectors operating in the 1.3 μm to 1.55 μm wavelength range. For this purpose, we developed and optimized a novel surface leakage suppression treatment based upon Zn diffusion via a Zn-containing spin-on-glass (SOG).[1, 2]

In general, the sensitivity of solid-state photodetectors is often limited by reverse-bias surface leakage current, apparently along the etched or cleaved sidewalls.[3, 4] At the semiconductor cleaved or etched surfaces, dangling bonds may pin the Fermi level. Under reverse bias, carriers in the bulk are blocked by the p-n junction. However, on the cleaved or etched surfaces, since the Fermi level is pinned, the carriers are not blocked, and thus, there are often surface leakage currents along the sidewall, as labeled by the arrow in Fig.E.1 (a).[5]

A common approach to reduce the surface leakage current is sidewall passivation using coatings such as silicon oxide (SiO_2) or silicon nitride (Si_3N_4).[6 7] However, after the sample has been fabricated and cleaved into individual devices, sidewall passivation is typically impractical. An alternative would be to avoid putting the cleaved or etched surface under bias. For example, Lin *et al.* developed a structure with an additional gate

electrode deposited on the sidewall along the junction perimeter, so that an external gate voltage could be applied to suppress the sidewall surface leakage current.[5] In addition, a significant reduction in leakage current was recently reported using epitaxial growth and post-growth patterning of an n-i-n structure, followed by spatially selective surface dopant type conversion during metal-organic chemical vapor deposition (MOCVD) re-growth using dimethylzinc and diethylzinc.[3, 4, 8, 9] However, this strategy requires an MOCVD facility, which was not conveniently available to the author.

In this work, we explored a novel ex-situ Zn diffusion approach to surface dopant type conversion of n-i-n diodes, using a commercially-available Zn-containing SOG, Zincsilicafilm 306 solution. The photodetector structure consisted of 200nm n^+GaAs grown on an n^+GaAs substrate, followed by a 1.5μm unintentionally doped InGaAsN photo-absorption layer, and a 200nm n^+GaAs capping layer. The targeted doping concentration in the top and bottom n^+GaAs was $5x10^{18}cm^{-3}$. The targeted doping concentration and In and N compositions were determined using the procedures discussed in sections 2.5 and 2.7. The targeted energy bandgap of the InGaAsN layer was 1.2eV.

To test the suitability of the surface leakage suppression treatment, comparison of the performance of a control device (i.e., without surface leakage suppression treatment) and a treated sample (with surface leakage suppression treatment) is needed. For the control sample, the n-type layer of the photoconductor was converted to p-type by Zn-diffusion, without any surface photolithographic patterning. Thus, the control sample mimics the direct growth of a p-i-n structure, as shown in Fig. E.1 (a). For the treated sample, the sample surface will be patterned by photolithography, so that only the central

area of the photodetector will be converted to p+ by Zn diffusion, while the periphery of the photodetector remains n-type, as shown in Fig. E.1 (b). Thus, when the sidewall of this structure is etched to form individual devices, the etched surface will not be under bias.

E. 2 Zn Diffusion and active Zn profile characterization

For the purpose of the photodetector fabrication, the top n-layer needs to be converted to p-type without penetration of the p-type dopants into the i-layer. Thus, a high ($>5x10^{18}cm^{-3}$) and spatially localized free hole concentration profile is needed. Although the Zn diffusion profile in GaAs has been characterized in the literature,[10] the active Zn profile, i.e. the free hole concentration profile, has not been reported. To identify the optimal annealing conditions for the desired free hole profile discussed above, the GaAs:Zn-SOG samples were annealed at 850ºC for various durations: 15, 20, 23, 30, and 40 minutes (Note that the manufacturer recommended a minimum annealing temperature of 850ºC for activation of the Zn in the Zn-SOG[11]). Each ~1 x 1cm^2 GaAs:Zn-SOG sample was cleaved into fourths, and one corner of each piece was then coated with photoresist as an etch stop. Following baking for 10 minutes at 130ºC, wet etching in H_3PO_4:H_2O_2:H_2O (1:1:25) was carried out for 0, 38, 75, 113 s, resulting in depths of 0, 135 ± 1, 182 ±14, 325 ± 18 nm, as determined by Dektak profilometry. The etched pieces were then cut into ~ 4 x 4 mm^2 pieces, and Hall and resistivity measurements were carried out at room temperature.

To quantify the free hole concentration profile, we assumed a so-called “finite source” Gaussian active Zn (free hole) concentration profile:

$$p(x) = p_0 \exp(-\frac{x^2}{2\sigma^2}) \tag{E.1}$$

where x is the depth from the unetched surface, which is defined as $x = 0$, p_0 is the free carrier concentration at unetched surface, $p(x)$ is the free carrier concentration at depth x, and σ is the characteristic diffusion length. Since the measured free carrier concentration is the remaining sheet carrier density in the film following each etching, the experimentally obtained data cannot be directly fit to Eq.E.1. Therefore, Eq.E.1 was integrated to fit the measured residual sheet carrier density, $p_s(x_e)$,as a function of etching depth:

$$p_s(x_e) = \int_{x_e}^{\infty} p_0 \exp(-\frac{x'^2}{2\sigma^2})dx' = p_0\sqrt{\frac{\pi}{2}}\sigma(1 - erf(\frac{x_e}{\sqrt{2}\sigma})) \tag{C.2}$$

where x_e is the depth etched and $p_s(x_e)$ is total residual carrier density following etching to the depth of x_e.

For each annealing time, p_0 and σ were obtained by fitting the measured data to the integrated Gaussian expression (Eq. E.2), as summarized in Table E.1. As shown in Table. E.1, annealing at 850ºC for 15 min yields free a hole concentration at 200 nm of ~ $9x10^{19}$ cm^{-3}, which is much higher than the n-type dopant concentration in the top of the GaAs photodetector structure ($5x10^{18}$ cm^{-3}), and is therefore sufficient to convert the top layer to p^+. Figure E.3 shows a plot of Gaussian fits to the free hole density vs depth for various annealing times. The Gaussian fits reveal that as the annealing time is increased, σ increases and p_0 decreases. As discussed earlier, for the purpose of photodetector

fabrication via surface dopant type conversion of n-i-n diodes, a high, spatially localized free hole concentration profile is needed. Thus, 850ºC for 15 min is identified as the optimal annealing condition.

Table:E.1 Surface carrier concentration, p_0, and characteristic diffusion depth, σ, for various annealing conditions determined from fits of the measured sheet carrier density to Eq. C.2.

Diffusion Time (min)	p_0 (10^{20}cm^{-3})	Diffusion length σ (nm)
15	1.3	250
20	1.2	290
23	1.17	320
30	1.09	370
40	1	450

For completeness, we compared our data with the GaAs:Zn diffusivity reported in the literature. Although there have been a wide range of values reported in the literature,[12-16] a similar trend was reported by Enquist *et al.*[10] Enquist measured the GaAs:Zn diffusivity at 850 ºC as D=1.5x10^{-13}cm^2/s, leading to a 15 min- 40 min diffusion length ranging from 120-200nm, similar to our values shown in Table E.1.

E. 3 Photodetector fabrication

The fabrication of both the control and modified photodetectors involves two major steps: annealing with Zn-containing SOG to convert the top layer to p-type, and photolithography to define mesa and contacts. In the following paragraph, we first describe the annealing process for the type conversion. We then describe the complete fabrication steps for both the control p-i-n and modified n-i-n photodetector structures.

The conversion of the top n-type layer from n- to p-type was realized by Zn

diffusion using Zn-containing Zincsilicafilm 306 solution. The GaAs wafer surface was first conditioned by heating at 350ºC to 400ºC for 5 minutes in air. Zincsilicafilm 306 was then coated on the wafer surface by spin coating at 3000 rpm for 1 minute. After spinning, the wafer was cured by heating in air for 10-15 minutes at 100°C to 120ºC.[11] Annealing was then carried out in a quartz furnace with N_2 overflow, with a GaAs proximity cap to prevent As out-diffusion. Following annealing, the Zincsilicafilm was removed by etching in 10% HF, and the surface was examined in an optical microscope.

For the control sample, the following fabrication steps including dopant type conversion, top p-type contact definition, mesa definition, and bottom n-type contact definition were utilized:

1. Dopant Type Conversion: Unmasked annealing @ 850°C for 15 min in N_2 ambient

2. Top p-type Contact Definition: Deposition of Pd/Zn/Pd/Au=100/200/200/2000 Å using SJ20 e-beam evaporator

3. Contact Annealing: RTA @ 410 °C for 2 min using JetFirst-150 RTP

4. Mesa Definition: H_3PO_4:H_2O_2:H_2O (1:1:2) wet etching for 13 min

5. Bottom n-type Contact Definition: (Ni/Ge/Au/Ti/Au=325/250/600/200/2000Å) using SJ20 e-beam evaporator

6. Contact Annealing: RTA @ 410 °C for 2 min using JetFirst-150 RTP

For the modified n-i-n photodetector sample, steps 1 (a) - 1(c) replace step 1

1 (a). SiO_2 Diffusion Mask Definition: deposit 1µm SiO_2 in GSI PECVD at 400 °C

(b). Selected Area Zn Diffusion: annealing @ 850°C for 15 min in N_2 ambient

(c). SiO_2 Mask Removal: buffered HF solution

E.4 Figures

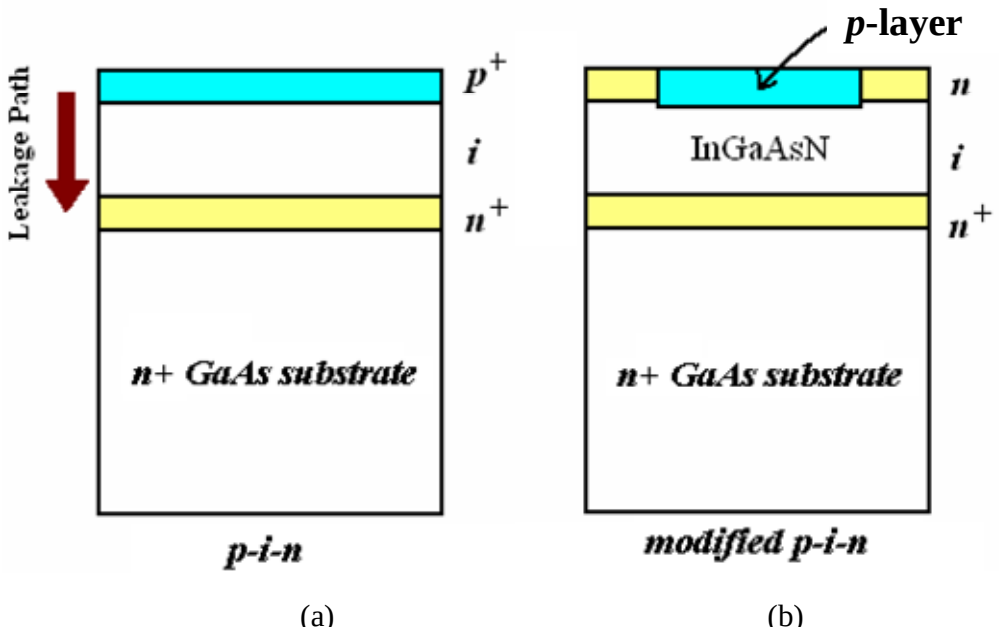

Figure E.1 Schematic of (a) control p-i-n photodetector and (b) modified n-i-n photodetector with central area converted to p-type by masked Zn diffusion.

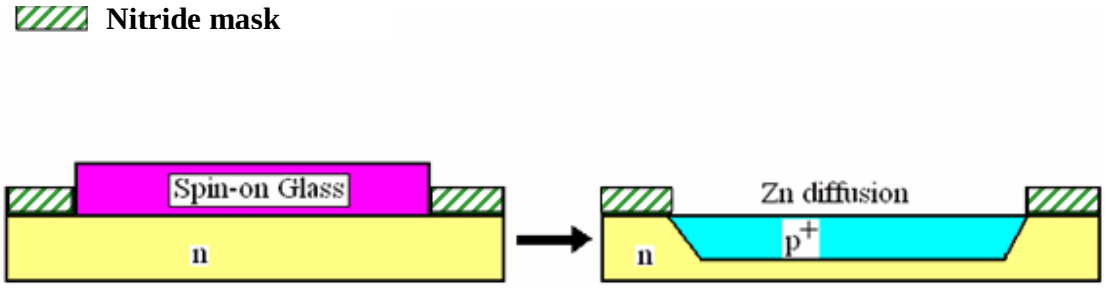

Figure E.2 Schematic of selective Zn diffusion process proposed for the modified n-i-n photodetector structure. A nitride mask is defined so that only the central area of the mesa is converted to p-type via the Zn-contained spin-on-glass.

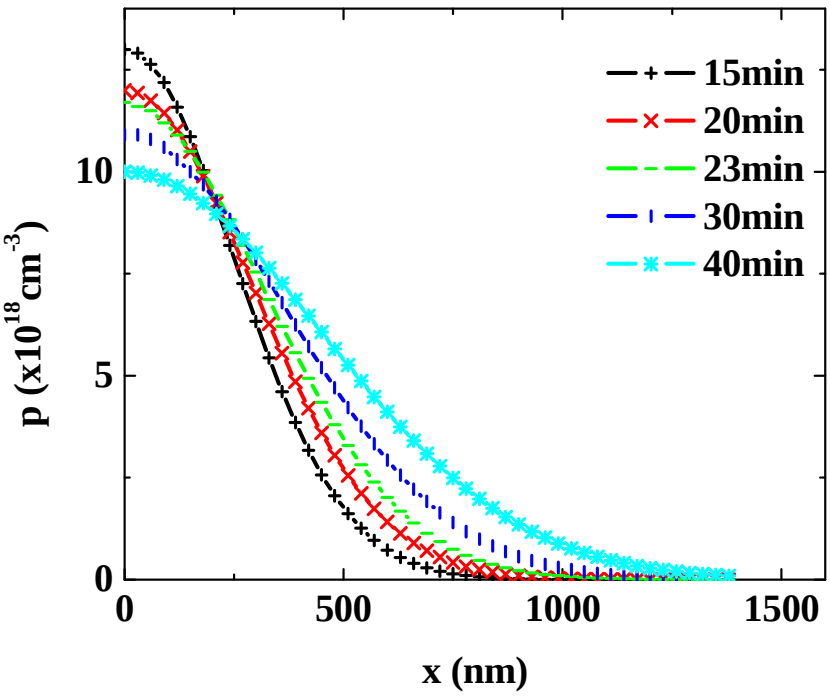

Figure E.3 Free hole concentration, *n*, vs. depth, *x*, for various annealing times, assuming a "finite source" Gaussian active Zn (free hole) concentration profile. As the annealing time is increased, the diffusion length increases and the surface hole concentration decreases.

E.5 References

[1]http://www.emulsitone.com/znsif_306.html; downloaded 10:00pm (Octobor 12, 2009)

[2]S. Rai,M.S. thesis, Notre Dame, 2004

[3]V. Bhagwat, Y. G. Xiao, I. Bhat, P. Dutta, T. F. Refaat, M. N. Abedin and V. Kumar, J. Electron. Mater. **35**, 1613 (2006).

[4]M. Gallant, N. Puetz, A. Zemel and F. R. Shepherd, Appl. Phys. Lett. **52**, 733 (1988).

[5]R. M. Lin, S. F. Tang, S. C. Lee, C. H. Kuan, G. S. Chen, T. P. Sun and J. C. Wu, IEEE Trans. Electron Devices **44**, 209 (1997).

[6]R. G. DeCorby, R. I. MacDonald, M. Beaudoin, T. Pinnington, T. Tiedje and F. Gouin, J. Electron. Mater. **26**, L25 (1997).

[7]S. Kollakowski, U. Schade, E. H. Bottcher, D. Kuhl, D. Bimberg, P. Ambree and K. Wandel, J. Vac. Sci. Technol. B **14**, 1712 (1996).

[8]N. Otsuka, M. Kito, M. Ishino, Y. Matsui and F. Toujou, J. Appl. Phys. **84**, 4239 (1998).

[9]K. Vanhollebeke, I. Moerman, P. Van Daele and P. Demeester, IEEE Int. Symp. Compound Semi. 205 (2000).

[10]P. Enquist, J. A. Hutchby and T. J. Delyon, J. Appl. Phys. **63**, 4485 (1988).

[11]http://www.emulsitone.com/znsif_306.html; downloaded 12Oct 2009

[12]H. Frank and S. A. Azim, Solid State Electron. **10**, 727 (1967).

[13]H. Rupprecht and C. Z. Lemay, J. Appl. Phys. **35**, 1970 (1964).

[14]J. Blanc, J. Appl. Phys. **45**, 1948 (1974).

[15]A. Luque, J. Martin and G. L. Araujo, J. Electrochem. Soc. **123**, 249 (1976).

[16]S. R. Styer and L. F. Donaghey, Materials Research Bulletin **10**, 1297 (1975).